Department of Precision and Microsystems Engineering

Tunable Magnet Actuators: Hysteresis Modelling for Efficient and Accurate Magnetization State Tuning

J.D. Wiersema

Report no	: 2022.034
Coach	: Dr. S.H. HosseinNia
Professor	: Dr. S.H. HosseinNia
Specialisation	: Mechatronic System Design
Type of report	: MSc Thesis
Date	: July 25 2022

Tunable Magnet Actuators

Hysteresis Modelling for Efficient and Accurate Magnetization State Tuning

by

Jasper Wiersema

to obtain the degree of Master of Science
at the Delft University of Technology,
to be defended on Monday July 25, 2022 at 10:30 AM.

Student number: 46025877
Project duration: September 1, 2021 – July 25, 2022
Thesis committee:

Dr. ir. S. H. HosseinNia,	TU Delft, supervisor
Dr. ir. A. Hunt,	TU Delft
Dr. ir. J. Dong,	TU Delft

An electronic version of this thesis is available at http://repository.tudelft.nl/.

TU Delft

Preface

In the last year, while working on this thesis, I have been fortunate enough to receive support from many individuals, to whom I would like to extend my sincerest gratitude.

First of all, I would like to thank my supervisor Hassan for guidance and support throughout the entire year. Giving me the autonomy and trust to take the project in my desired direction has taught me a lot in research and project management. Your enthusiasm and criticism have kept me motivated and engaged during the entire process, resulting in the work presented in this report.

A special thanks to my fellow students, with whom I have had the pleasure to work on the Tunable Magnet Actuator project. Our countless discussions and hours spent in the lab have been a great source of motivation and have contributed to the quality of this work.

Thanks to the complete Precision and Microsystems Engineering staff and students for providing help where needed and for sharing your thoughts during the weekly update meetings.

Finally, a special thanks to all of my friends and family for supporting me during my time at the Delft University of Technology.

Jasper Wiersema
Delft, July 2022

Summary

In the precision industry, Reluctance Actuators are widely used to obtain precise and fast actuation. These actuators use coils in a magnetic circuit to generate a controllable flux, which results in a force on the mover. However, coil-based actuators need a constant supply of current to generate a flux which causes heat generation through Joule heating. As a result, deformations in the machine will lead to reduced precision and repeatability. This is especially prevalent in systems operating in quasi static operation with large bias forces in a vacuum or cryogenic environment. To solve this problem, a new type of magnetic actuator has been developed, the Tunable Magnet Actuator. Here, a low-coercivity Permanent Magnet (PM) is used to generate the flux in the magnetic circuit. By changing the Magnetization State (MS) of the PM, the flux can be controlled and 'tuned' to a desired value within the magnet's $B(H)$-curve. A magnetizing coil is used to generate the external field which changes the MS. Once tuned, the MS remains constant, generating a constant force without any heat generation.

In the previous work performed by S.G. Viëtor [39] and R. Meijer [25], MS tuning methods have been developed to change the magnetization state of the PM. However, the methods introduced have used simplifications that have led to inherent downsides. The Saturation Magnetization State Tuning (SMST) method introduced by Viëtor achieved accurate tuning. However, by saturating the PM in between tuning steps, relatively large currents are required which reduces the efficiency. The Minor-loop Magnetization State Tuning (MMST) method introduced by Meijer removed the saturation step from the tuning process, greatly improving the efficiency. However, linearization of the hysteresis curves has led to a significant loss in accuracy. This thesis aims to improve on the state of the art by introducing a novel tuning method combined with a non-linear and history dependent modelling approach to allow for continuous, accurate and efficient MS tuning.

The tuning process is characterized by the non-linear and history dependent characteristics of magnetic hysteresis. The behaviour can be described using Madelung's rules. The tuning algorithm used should follow these rules by tracking the previous MSs and using this to determine the order of reversal curve of the new MS. For this purpose, the Envelope Magnetization State Tuning (EMST) method is introduced. The EMST allows for sequential MS tuning, while minimizing the heat generation during the tuning process.

To accurately use the EMST, a hysteresis model is needed which uses the previous MSs, the desired MS, and the corresponding order reversal curve to calculate the Corner Point (CP). A specifically designed hysteresis modelling approach is introduced to handle this. Measured reversal curves up to a certain order are used to identify multi-variable polynomials by mapping the magnetization history to the CP coordinates. For every measured order, two polynomials are identified (one for H_{CP} and one for B_{CP}) and the right order is selected based on the output of the EMST algorithm.

Since measuring higher order reversal curves requires exponentially more data for every order, an estimation model is introduced which estimates these higher orders based on lower order data. Using the congruency property of magnetic hysteresis and the fact that reversal curves are close to linear between the CP and the remanence, higher order curves can be estimated using First Order Reversal Curve (FORC) data. The CP to reach a desired MS is then estimated to be the intersection between the FORC crossing this MS and the measured reversal curve crossing the previous MS. By extending the measured model with the estimation model, continuous MS tuning is possible independent of the order.

An experimental setup is build to validate the performance of the introduced modelling approach and the EMST algorithm. Validation shows that the hysteresis model improves the static accuracy with approximately 50% compared to the model used in previous work. Furthermore, by combining the EMST with a flux controller to reach the desired CP, a theoretical heat generation reduction of 86% is observed compared to the SMST while no significant difference in MS tuning accuracy is measured.

Contents

List of Figures

List of Tables

Glossary

AlNiCo Aluminium-Nickel-Cobalt.

BTI Break-even Tuning Interval.

CP Corner Point.

DA Dynamic Air-gap compensation.
DRS Dynamic Recoil-line Slope compensation.

EMST Envelope Magnetization State Tuning.

FEA Finite Element Analysis.
FF Fringe Flux-loss compensation.
FO First Order.
FORC First Order Reversal Curve.
FPGA Field-Programmable Gate Array.

HDM Hysteretic Deformable Mirror.
HTMA Hybrid Tunable Magnet Actuator.

MEC Magnetic Equivalent Circuit.
MGC Magnetic Gravity Compensator.
MMF Magneto Motive Force.
MMST Minor-loop Magnetization State Tuning.
MS Magnetization State.

NdFeB Neodymium-Ferite-Boron.

PPI Parallel PI flux-feedback control.

RA Reluctance Actuator.
RMSE Root Mean Square Error.

SMA Switchable Magnet Actuator.
SMST Saturation Magnetization State Tuning.
SO Second Order.
SORC Second Order Reversal Curve.

TMA Tunable Magnet Actuator.

VFMM Variable Flux Memory Motor.

1

Introduction

1.1. Motivation

In the precision industry, magnetic actuators are widely used to obtain high accuracy and efficient actuation. Currently, these actuators often use coils to create magnetic forces. Two widely used methods of implementing this, are the Lorentz actuators and Reluctance Actuators (RA). Lorentz actuators are characterized by good predictability and easy control due to the linear force-current relationship, but the actuator has a relatively low force density. RAs overcome this downside, as they can have force densities up to 10 times larger than that of the Lorentz actuator [40]. Due to the high force density, less volume is needed for the actuator which leads to an increase in system efficiency, making it a very attractive actuator to use in precision actuation systems.

When looking at the a basic RA, it shows that the force current relation is non-linear, more specifically, it is proportional to the current squared [34]. Using recent control theory, this is not a problem in implementation [13], however, it does lead to the problem of Joule heating. The force-current relation shows that for a constant force, a constant supply of current is needed, which heats up the system through copper losses in the coil windings. This can become a problem in precision systems that operate in quasi static operation with a large bias force in a vacuum environment. Here quasi static refers to operation where a constant bias force is needed for an extended period of time before changing the bias force magnitude. A large bias force scales the heat generation exponentially due to the non-linear force current relation. The vacuum environment limits the heat dissipation of the machines due to the lack of convective cooling. The produced heat in the actuator leads to deformation of the system, reducing the accuracy and repeatability of the machine.

One of the possible application areas where these conditions apply is the EUV lithography machine manufactured by ASML [4] (figure 1.1a). This system houses machines known as Magnetic Gravity Compensators (MGC), which ensure that external vibrations do not cause disturbances on the end-effector while providing a constant bias force to counter the gravity acting on the mover [12]. In the EUV lithography machine, the MGC isolates a lens placed in vacuum from the outside environment, which is used to guide an extreme ultraviolet light beam on a silicon wafer. During operation, sub-nanometer precision is required for the lens position to accurately guide the light beam. Another application area could be devices in space where systems inherently operate in a vacuum. The deformable space mirror developed by TNO [20] (figure 1.1b) for example, uses electromagnetic actuators to change the mirror shape between measurements. These measurements can last from seconds up to months while the actuator position must remain accurate. Similarly to the EUV lithography machine, this system operates in the limiting conditions of reluctance actuator where Joule heating can pose serious challenges.

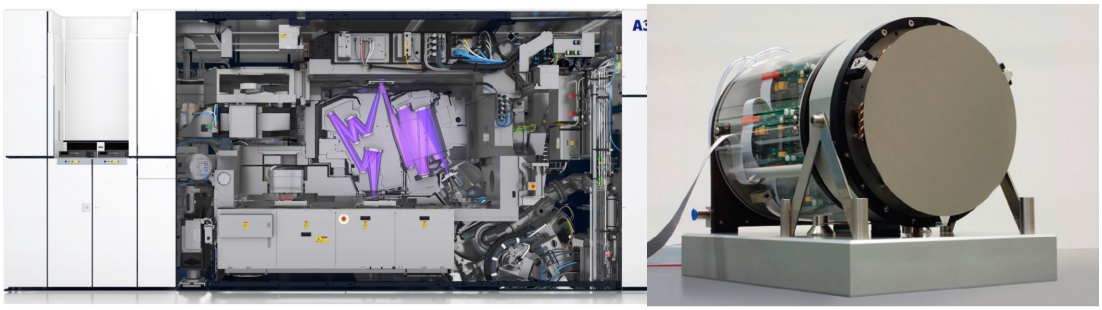

(a) (b)

Figure 1.1: (a): The EUV Lithography Machine manufactured by ASML [4] (b): The deformable space mirror developed by TNO [20].

1.2. Prior Art

To solve the problem of Joule heating in reluctance actuators, Permanent Magnets (PMs) can be used as source for the magnetic flux in the reluctance actuator instead of a coil. Where a coil needs the supply of current to generate a flux, a PM does not. To be able to use this in a dynamic application however, the magnetization level op the PM needs to change, leading to the problem of in-situ Magnetization State (MS) tuning.

Switchable Magnet Actuator This idea of using a low-coercivity PM to change the force in an actuator by changing its MS, has been implemented by A. Knaian in the development of a Switchable Magnet Actuator (SMA) [19]. The SMA uses two permanent magnets, a high coercivity NdFeB PM and a low-coercivity AlNiCo PM with comparable remanent fluxes (figure 1.2a). These magnets are wound by a coil which is used to change the magnetization of the soft magnet but not change the magnetization of the hard magnet. This results in an actuator with an on- and off-state. In the off state, the soft magnet operates in the negative saturated remanent magnetization state and the fluxes cancel each other resulting in a net zero flux density. In the on-state, both magnets operate in the positive saturated remanent magnetization state and the fluxes add up to a net positive flux density resulting in a force on the mover.

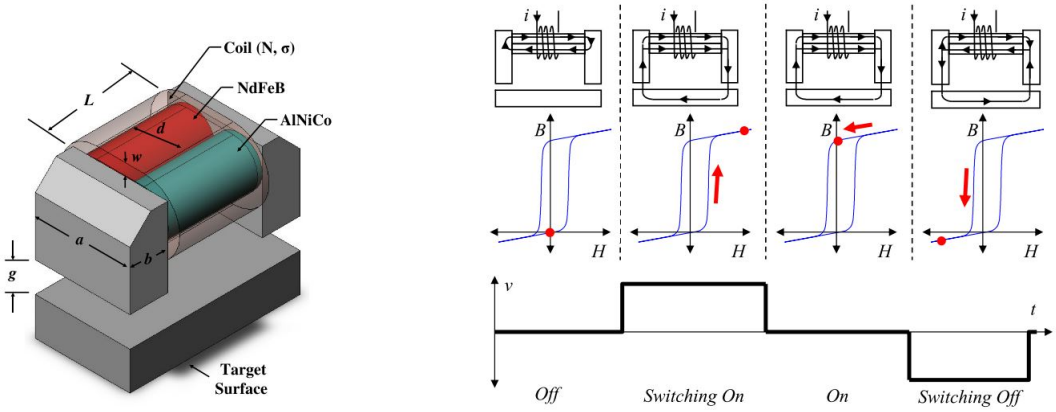

(a) (b)

Figure 1.2: (a): SMA with an AlNiCO and NdFeB magnet (b): Process of switching the SMA between the on- and off-state, adapted from [19].

Tunable Magnet Actuators First proposed in the work of S. Viëtor [39], the Tunable Magnet Actuator (TMA) is an actuator with a continuous variable force profile based on MS tuning of low-coercivity PMs. The design proposed is based on a conventional C-shaped RA with a PM placed inside the coil (see figure 1.3). The force on the mover for such a circuit is related to the air gap flux density as shown in equation (1.1). Here subscript g relates to the gap with B the magnetic flux density and A the area. By

using the PM as flux-source, a constant bias force can be held without the constant dissipation of energy. The coil wound around the magnet is used to magnetize and demagnetize the PM by generating an external magnetic field (H) in the PM resulting in a change in magnetic flux density in the PM according the its $B(H)$ characteristics. By changing the flux density in the magnet, the constant bias force on the mover is changed, this follows from the relation between magnetic flux density and air gap flux density depicted in equation (1.2). Here the subscript m relates to magnet parameters.

$$F_x = \frac{B_g^2 A_g}{\mu_0} \tag{1.1}$$

$$B_g = \frac{B_m A_m}{k_1 A_g} \tag{1.2}$$

Viëtor realized the C-Shaped TMA set-up and introduced the novel Saturation Magnetization State Tuning (SMST) method which allowed for discrete pre-defined tuning steps. The TMA principles have been experimentally validated on a fixed mover setup with accurate tuning results using the SMST. A theoretical comparison metric called the Break-even Tuning Interval (BTI) is introduced to compare the efficiency of the TMA with an equivalent reluctance actuator.

As an continuation on this work, R. Meijer implemented dynamic MS tuning in the TMA setup [25]. By connecting the mover to a flexure mechanism and by implementing multiple real-time compensation methods, accurate and continuous magnetization state tuning on a dynamic set-up was achieved and validated using the SMST. Finally, the novel Minor-loop Magnetization State Tuning (MMST) method was introduced as a more efficient alternative to the SMST by minimizing the heat generation during the tuning process. While the increased efficiency has been experimentally validated, a loss of accuracy in MS tuning was observed.

W. Hoekwater introduced the novel Hybrid Tunable Magnet Actuator (HTMA) with the aim to linearize the force-flux relation of the actuator [11]. The HTMA achieves this linearity by using high-coercivity PMs to provide bias fluxes in the air gaps of the actuator. The force-flux relation has been experimentally validated to be linear over an 800μm mover range allowing for linear control implementations.

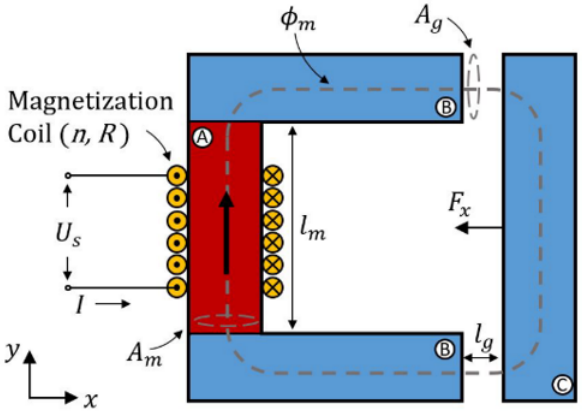

Figure 1.3: Schematic of the TMA circuit, adapted from [39]

Variable Flux Memory Motors Outside of applications where MS tuning is used for force generation in electro magnetic actuators, it has also been used in synchronous motors. First introduced by Ostovic [27], Variable Flux Memory Motors (VFMMs) get their name from the magnetic property where the magnets are able to memorize their flux density magnitude. In the VFMM, the MS of a low-coercivity permanent magnet is changed by a short current pulse through the stator coils. This allows for flux weakening in the motor without the constant supply of current as is done in conventional synchronous motors [16]. Yu et al., improved this initial concept by decoupling the demagnetization and load currents by using separate windings to demagnetize the magnet [43]. Whereas the SMA only switches

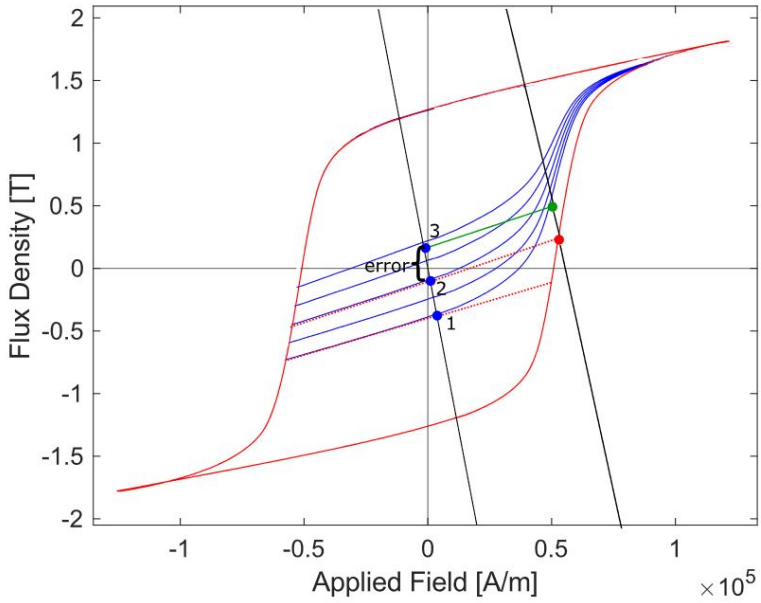

Figure 1.4: Visualization of MMST limitation. Here, the tuning step performed should be from point 1 to point 2. However, due to the non-linearity of reversal curves, point 3 is reached when a linear model is used.

between two magnetization states, the VFMMs use the entire range of obtainable magnetization states in operation, making it an interesting body of research for TMA applications as well.

1.3. Problem Definition

Previous work has mainly focused on proving the concept of the TMA for industrial applications. This has resulted in a robust base which shows the potential of the TMA. However, on the performance side, a lot more can be gained. The SMST has proven to allow for accurate MS tuning with B_m accuracies in the 18mT range. However, the saturation step needed to reach a MS, makes the method inherently inefficient. The MMST improves the efficiency by removing the saturation step from the tuning process by 20-90%. However, the B_m accuracy of the MS tuning is much lower than that of the SMST.

It is suspected that this loss of accuracy is caused by the simplifications made in the development of the MMST. The approach assumes a linear and history independent B-H curve while magnetic hysteresis is non-linear and history dependent. Figure 1.4 illustrates how these assumptions can reduce the accuracy of the achieved MS tuning. The implemented controller provides a current such that the load line intersects the calculated Corner Point (CP) (red point). By simplifying the B-H curve, errors in H_{CP} and B_{CP} are expected, which may result in a large error between expected and realized CP (green point) due to the steep slopes of the load line and the reversal curves around the CP.

Furthermore, both methods have not yet been implemented with a continuous use-case where multiple magnetization states should be reached in succession. During validation, the magnet was always magnetized to a reference MS prior to the tuning process, reducing the history dependent effects. In industrial applications it is desired that the MS is continuously changed without the need to first magnetize to a reference value. A continuous tuning algorithm and hysteresis model are needed to further increase the applicability of the TMA.

1.4. Research Goal and Objectives

To improve on the limitations described in section 1.3, the research goal of this thesis can be described as follows:

Develop a continuous tuning algorithm combined with a non-linear and history dependent hysteresis

model to allow for efficient and accurate magnetization state tuning.

The following objectives are defined to reach this goal:

1. **To describe a tuning approach which respects the non-linear and history dependent characteristics of magnetic hysteresis.** By the implementation of a tuning algorithm which adheres to the phenomenological behaviour of magnetic hysteresis, it will be possible to ensure that the tuning step performed is as efficient as possible.

2. **To develop a generalized hysteresis modelling approach based on measurement data.** By identifying a hysteresis model on measurement data of the tunable magnet, accurate MS tuning will be achieved. Due to the history dependent nature of magnetic hysteresis, an estimation method will be developed to limit the amount of measurement data needed while still allowing for continuous MS tuning.

3. **To validate the performance of the tuning algorithm and hysteresis modelling approach.** Using a simplified TMA design, experimental validation of the developed methodologies will be performed. The hysteresis models will be tested for accuracy and the algorithm for efficiency with respect to the state of the art.

1.5. Thesis Outline

In chapter 2 necessary background information is provided on magnetism, the TMA state of the art and hysteresis modelling. The contributions of this paper are presented in paper-format in chapter 3 under the title: *Hysteresis Modelling for Efficient and Accurate Magnetization State Tuning of Soft Magnets.* Chapter 4 concludes the work and suggests recommendations for future work.

Additional information is provided in several appendices. A literature review on Hysteresis Modelling is given in Appendix A, where the need for a new approach is discussed. Appendix B discusses eddy current damping in non-laminated and laminated magnetic circuits and how this influences hysteresis behaviour. The experimental set-up used during this work is shown in Appendix C. For readers who are interested in reproducing this work, the identification of the hysteresis models and implementation of the algorithms is discussed in Appendix D. Finally, some useful data sheets are included in Appendix E.

2

Preliminaries: Magnetism and Tunable Magnet Actuators

This chapter provides background information necessary for understanding the principles used while performing the research of this thesis. The first section covers basic magnetism and magnetic hysteresis, laying the foundation to understanding the working principles of the TMA and its current limitations. In section 2.2 an elaborate review of the state of the art of the TMA is provided, highlighting tuning and hysteresis modelling.

2.1. Magnetism

In this section, background information on magnets, hysteresis and magnetic circuits is provided. If the reader has sufficient knowledge on these topics, this section can be skipped. For readers that have little knowledge on the subjects, it is advised to read this chapter to understand the remainder of this research. The following books are the main source for the following chapter [5], [7], [14], if other sources are used this will be specified later.

2.1.1. Permanent Magnets

Magnetic field and magnetization The magnetic state of a permanent magnet can be described using the magnetization vector **M**. This vector describes the volume density of the magnetic moments inside a material. In ferromagnetic materials, this magnetization vector is the sum of the magnetic moments of the magnetic domains. Another parameter to describe the magnetic state of a magnet is the flux density **B**. The flux density consists of two contributions, the flux density applied to the magnet $\mu_0\mathbf{H}$ and the flux density from the magnetization of the material $\mu_0\mathbf{M}$. The flux density is then given by:

$$\mathbf{B} = \mu_0(\mathbf{H} + \mathbf{M}) \tag{2.1}$$

Where **H** is the applied magnetic field intensity. The Magnetization State (MS) of a magnet refers to the current state of **B** and **H**.

Magnetization process In ferromagnetic materials, the initial state is a demagnetized state where all magnetic moments of the magnetic domains are oriented randomly resulting in a net zero magnetization. Inside the magnetic domains, atomic moments are aligned parallel due to the phenomenon of spontaneous magnetization. If an external field **H** is applied to the material, these domains will rotate in the direction of the applied field. By applying a high enough external field, all magnetic domains become parallel resulting in a maximum magnetization called saturation. Part of the changes that occurred inside the magnetic domains are irreversible and part of it is reversible, this becomes evident when the external field is removed. The magnetic domains do not remain in the parallel alignment but small rotations occur reducing the total magnetization of the magnet. This value is referred to as the remanent magnetization. This process is visualized in figure 2.1.

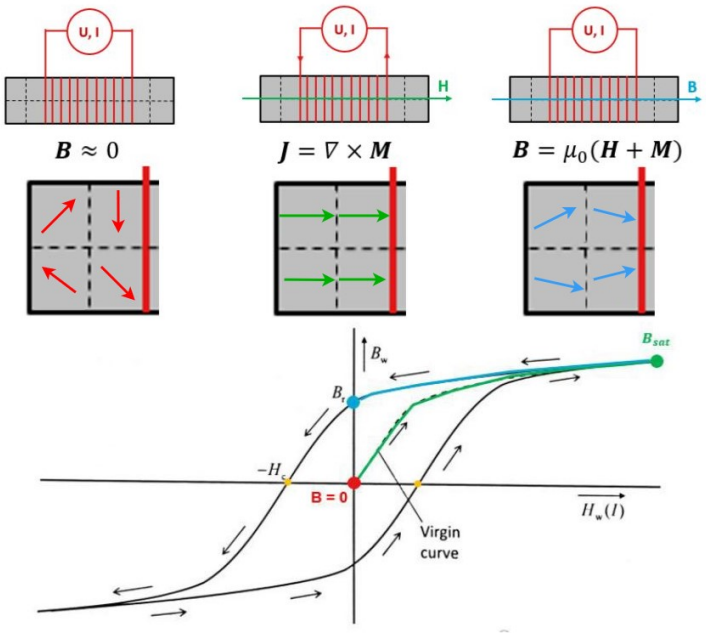

Figure 2.1: Schematic of the magnetization process of a ferromagnetic material, adapted from [39]

Hysteresis Curve The process described above can be plotted in either an $M(H)$ curve or a $B(H)$ curve since they are directly related. Because we are mostly interested in the magnetic flux density of the magnet since this is directly related to forces created in reluctance actuators, we will use the $B(H)$ curve in this research. The process described in the previous paragraph can be extended by applying a negative magnetic field, this will de-rotate the domains and reduce the magnetic flux density. The magnetic field needed to reduce the flux density to zero is called the coercive field (H_c). This value indicates if the magnetic material is a hard or soft material, in other words, is it easy to demagnetize (soft) or not (hard). By decreasing the applied field further, we reach negative saturation. This point is symmetric from positive saturation and the phenomena observed here are symmetric to those observed at positive saturation. By closing the loop between negative and positive saturation, we find the major loop of the magnetic hysteresis curve.

2.1.2. Magnetic Hysteresis

In this subsection, detailed information and properties of the magnetic hysteresis curve are discussed. These properties are history dependence, the existence of reversal curves, energy losses and time dependence.

History dependence From the major loop of the hysteresis curve (figure 2.2), it can be seen that the magnetic state is history dependent. Depending on the previous MSs of the material, the response to an external field will be different. When a magnet is in its demagnetized state where all domains are oriented randomly, there is no history inside the material. During it's first magnetization to saturation it will follow the virgin curve. It is impossible to follow this curve again without resetting the history of the magnet. Methods to reset the history have been discussed by Bertotti and Ivanyi [5][14], and it is suggested that by applying a cycling field with decreasing amplitude, this state can be reached again.

Reversal Curves The major loop of the hysteresis curve envelopes the reachable B-H domain of the material. Every point inside the envelope can be reached by an infinite amount of possible routes. When traversing the major $B(H)$ curve from remanence by decreasing the external field, a reversal curve can be entered by reversing the external field from decreasing to increasing. A curve that is entered by reversing the external field while traversing the major loop is known as a First Order Reversal Curve (FORC), for example curve 2-5-3-1 in figure 2.2. When reversing the magnetic field while traversing a FORC, the entered curve is called a Second Order Reversal Curve (SORC) (curve 5-2) and so on.

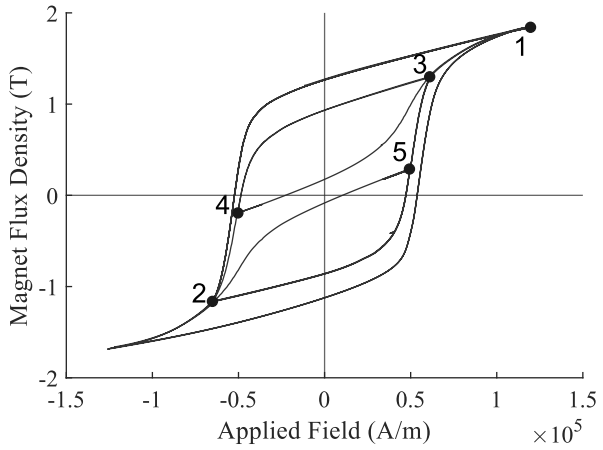

Figure 2.2: Major and minor loops of the magnetic hysteresis curve for an AlNiCo-5 PM, note that loops are always traversed in counter-clockwise direction.

A closed loop inside the $B(H)$ curve that consist of a FORC and SORC or any higher order reversal curves is called a minor loop (e.g. loop 2-5-2).

Madelung's rules The history dependent phenomena that describe magnetic hysteresis have been studied extensively. In the year 1905, Madelung introduced a set of rules which describe these phenomena called Madelung's rules [24]. In [47] Zirka et al., described them in modern terminology and they are summarized below, the paths described are shown in figure 2.2.

1. The path of any reversal curve is uniquely determined by the coordinates of the reversal point and its magnetization history (History dependency of magnetic hysteresis).
2. If any point 3 of curve 2-3-1 becomes a new reversal point, then curve 3-4-2 originating at point 3 returns to the initial point 2 (Return point memory or loop closure).
3. If point 4 of the curve 3-4-2 becomes the newest reversal point and the transition curve 4-3 extends beyond the point 3, it will pass along section 3-1 of curve 2-3-1 as if the previous closed loop 3-4-3 did not exist at all (wiping out property).
4. All transition curve that start from the reversal points having the same flux density and sign, can be brought into coincidence by their parallel motion along the H axis (B congruency of the reversal curves).
5. If some point on the initial magnetization curve becomes a reversal point, then the reversal curve will cross a point symmetric around the origin(odd symmetry of the hysteresis curve).

Energy losses and time dependence From the hysteresis curve, the energy dissipated during magnetization and demagnetization can be calculated and is proportional to the volume of the magnetic material and the area of the hysteresis curve enclosed.

$$E_{hyst} = A_m l_m \int H_m dB_m \tag{2.2}$$

Until this point, we have described rate-independent hysteresis, referring to hysteresis independent of the field rate of change. However, in reality, there are two important phenomena that are time dependent. First is the production of eddy currents between domain walls that limit the diffusion speed of the induction [5]. These eddy currents cause loop-widening in the hysteresis curve which streches the $B(H)$ curve along the H-axis, resulting in the need for higher amplitude external field when using high rates of change. Appendix B contains a detailed investigation into the effects of loop widening in TMA and its effect on the $B(H)$ curves. Second is thermal relaxation which says that the system will move to lower energy states when the temperature is not absolute zero. The rate at which this happens is represented by the magnetic viscosity of a material.

2.1.3. Magnetic Circuits

Untill now, we've only looked at a magnet with a coil surrounding it without any magnetic circuitry attached. When a magnetic circuit is added to the system, a $B(H)$ relation is added. This relation can be modelled using Magnetic Equivalent Circuit (MEC) Modelling [34].

Magnetic Equivalent Circuits The MEC model is a lumped parameter approach to model magnetic circuits in a way that is comparable to electrical circuits [34]. The basic equation used in this model is the calculation of magnetic flux Φ as a function of the magnetomotive force MMF and the reluctance R:

$$\Phi = \frac{MMF}{R} \tag{2.3}$$

Here the flux can be seen as current, the magnetomotive force as voltage and the reluctance as the resistance when comparing it to an electrical circuit.

The MMF comes from sources that create magnetic fields, such as magnets (equation 2.4) and coils (equation 2.5).

$$MMF_{PM} = H_M l_M \tag{2.4}$$

$$MMF_C = NI \tag{2.5}$$

The reluctance of an element inside the flux path can be described using equation 2.6:

$$R = \frac{l_\Phi}{\mu A} \tag{2.6}$$

Where l_Φ is the length of the element in the flux path, μ is the magnetic permeability and A is the area of the cross-section of the flux path. Finally, the flux can be related to the flux density at a certain part of the circuit using equation 2.7:

$$B = \frac{\Phi}{A} \tag{2.7}$$

Combining equations 2.3-2.7, the flux density can be related to the magnetic field and the circuit parameters, this relation is known as the load line of the circuit.

$$B_m = f(H_m) \tag{2.8}$$

Combining circuits and magnets Two relations have been found that relate the magnetic field and the magnetic flux density in a magnetic circuit with a coil and a permanent magnet. Combining these two relations, the operation point of the magnet can be found and is equal to the intersection between the load line and the hysteresis curve. Figure 2.4 illustrates this operating point.

2.2. Tunable Magnet Actuators

This section discusses the state of the art of Tunable Magnet Actuators.

2.2.1. TMA: review S.G. Viëtor

The first work on the TMA has been performed by S.G. Vïetor [39]. Similarly to the ideas used in the VFMM, the TMA uses in-situ magnetization of AlNiCo permanent magnets to increase the efficiency of the machine for certain applications. In this subsection, a review on the work done is given.

Concept of TMA The design proposed in Viëtor's work is based on a conventional C-shaped RA [34]. A magnet is placed inside the coil of the RA to get the design shown in figure 2.3. The force on the mover for such a circuit is related to the air gap flux density (equation 2.9). The coil is used to apply a magnetic field to the magnet to reach different MSs in the magnet. By changing the flux density in the magnet, the constant bias force on the mover is changed, this follows from the relation between magnetic flux density and air gap flux density depicted in equation 2.10.

$$F_x = \frac{B_g^2 A_g}{\mu_0} \tag{2.9}$$

$$B_g = \frac{B_m A_m}{k_1 A_g} \tag{2.10}$$

Using the MEC modelling approach, the load line of the circuit is determined and is given as:

$$B_m = -\mu_0 \frac{k_1}{k_2} \frac{A_g l_m}{2 A_m l_g} (H_m - \frac{NI}{l_m}) \tag{2.11}$$

where N is the number of coil windings, subscripts g and m denote magnet and gap respectively with l length and A area, and I is the coil current. From this equation, it can be seen that the load line has a slope and a shift along the H_m-axis. The slope is dependent on the air gap length between stator and mover, to simplify the problem, the gap was kept constant during the tuning cycle. Furthermore, the slope is a function of system parameters and two loss factors, k_1 and k_2. k_1 represents the flux leakage coefficient and describes the amount of flux going through the magnet that arrives in the gap as useful flux. k_2 is the MMF loss factor, describing the unwanted magnetization of circuit components. Values for these parameters where identified using a magnetic FEA in COMSOL.

The shift of the load line is a function of the coil dimensions and the current flowing through the coil windings. This shift shows that by applying a current, the MS of the magnet will traverse the hysteresis curve as the intersection between load line and hysteresis curve is changed.

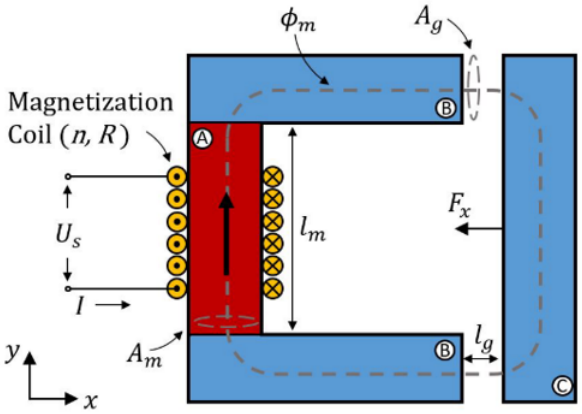

Figure 2.3: Schematic of the TMA circuit, adapted from [39]

Tuning method and modelling approach Viëtor introduced a method to tune the magnet to different magnetization states called the Saturation Magnetization State Tuning (SMST) method. This method relies on the use of the first part of FORCs originating from the descending branch of the major loop. The starting point of this method is any arbitrary MS of the magnet. When a new MS is desired, it is checked whether the state is higher or lower than the current state. When the state is lower, the magnet is immediately demagnetized until the desired Corner Point (CP), from where the applied magnetic field is removed. When a higher state is desired, the magnet is first saturated before it is demagnetized along the major loop again. Figure 2.4 shows the algorithm used for the SMST and the path traversed in the hysteresis curve of the AlNiCo magnet.

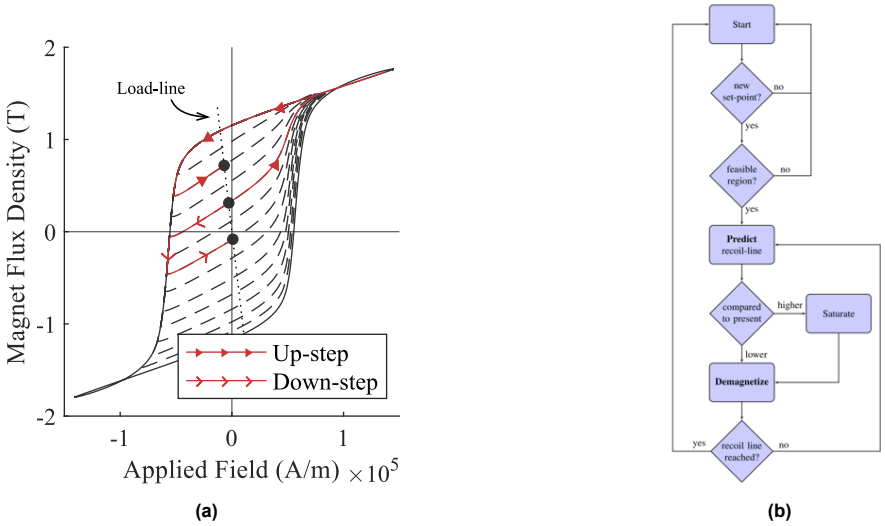

Figure 2.4: (a): The SMST tuning cycle with up-stepping and down-stepping. (b): the SMST tuning algorithm, adapted from [39]

To calculate the CP from the desired operating point and the current operating point, a linear hysteresis model is developed. In this model, the FORCs are linearized between the CPs and the load line. The identification for the linear reversal curves was performed for 8 different FORCs. Using the linear model and the relation for the load line, 8 different CP were predetermined and used as set points for the controller.

Break-even Tuning Interval To validate the claim that a TMA can decrease the heat generation in certain actuation systems, a metric for comparison has been developed. This comparison is based on the fact that a TMA can provide a constant bias force without a constant supply of current. Only an initial investment of energy is needed during the tuning process of the magnet to reach this constant bias force. A normal reluctance actuator however, requires a continuous current input to maintain a constant force. This means that the longer the static force needs to be maintained, the more efficient the TMA becomes compared to a normal reluctance actuator. The moment the TMA becomes more efficient than the reluctance actuator is named the Break-even Tuning Interval (BTI) or T_{be} and is defined as the interval between tuning cycles, such that a TMA dissipates the same amount of energy as a comparable normal reluctance actuator. In equation form this is written as follows:

$$T_{be} = \frac{E_{hyst} + E_{TM,copper}}{P_{EM}} \tag{2.12}$$

Where E_{hyst} are the hysteresis losses of the tuning cycle, $E_{TM,copper}$ are the losses in the coil due to Joule heating during the tuning cycle, and P_{EM} is the power consumption of a reluctance actuator. The hysteresis losses are calculated through the area enclosed in the hysteresis loop:

$$E_{hyst} = A_m l_m \int H_m dB_m \tag{2.13}$$

The copper losses in the coil are subdivided into 3 steps of the magnetization cycle, namely: saturation, demagnetization and decay. These are calculated as follows:

$$E_{TM,copper} = E_{TM,sat} + E_{TM,demag} + E_{TM,decay} \tag{2.14}$$

$$E_{TM,sat} = \int_0^{T_{sat}} I_{sat}^2(t) R dt$$

$$E_{TM,demag} = \int_0^{T_{demag}} I_{demag}^2(t) R dt$$
$$E_{TM,decay} = \int_0^{T_{decay}} I_{decay}^2(t) R dt$$

Viëtor performed an analysis on the influence of system parameters on the theoretical BTI. Namely, the gap flux density, air gap length and supply voltage are investigated. The BTI decreases monotonically for all these 3 parameters. In a nominal scenario, the T_{be} approximates to 1 second. Furthermore, the analysis led to conclusions on the applicability of the TMA, which are:

- Low actuation bandwidth
- Quasi static operation
- Large constant bias force
- Small scale actuation

Bandwidth Outside of static operation, the actuator can also be used for dynamic operation. Here the BTI determines the bandwidth of the actuator for which it is more efficient than a comparable reluctance actuator. Using basic sampling rules, a sinusoidal force trajectory can be approximated using 10 constant force samples. This leads to the following expression for the bandwidth:

$$f_{bw} \leq \frac{1}{10 T_{be}} \tag{2.15}$$

2.2.2. TMA: review R. Meijer

As a continuation on the work of Viëtor, Meijer's work can be subdivided into 4 focus points [25], namely:

1. Implementing a dynamic test setup
2. Increase tuning performance
3. Introducing the MMST approach
4. Validation of the BTI

In this section, these points will be discussed.

Implementing a dynamic test setup Viëtor's work has been based on a setup with a constant air gap during the tuning cycle. In reality however, this air gap will vary because the mover is not fixed. Meijer implemented this through the design of a parallel flexure mechanism which can be seen in figure 2.5. In addition, the calculation of the CP has been implemented in a real time application such that any MS within the reachable domain can be obtained rather than the 8 predefined set points. Important to note is that the model used to describe the FORCs is the linear model identified by Viëtor.

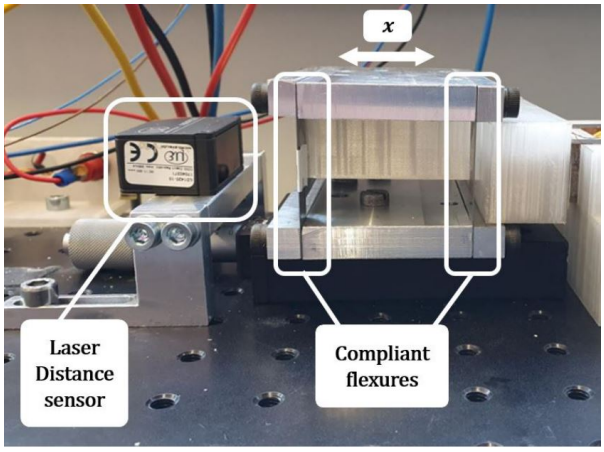

Figure 2.5: TMA with flexure mechanism for dynamic operation, adapted from [25].

Increase tuning performance It was found that the performance of the tuning method as proposed by Viëtor was highly dependent on the magnetization set-point and air-gap length when implemented on the dynamic setup. Meijer identified several causes for this and implemented compensation methods to increase the performance over a broader operating range.

Dynamic Recoil-line Slope Compensation (DRS)

The recoil-line slope μ_{rec} has been identified to be dependent on the CP. This has been identified as a 10th order polynomial by Viëtor. Meijer linearized this relation to obtain a relation for μ_{rec} which is implemented in the real time CP prediction:

$$\mu_{rec} = 0.955B'_r + 4.69 \tag{2.16}$$

Dynamic Air-gap compensation (DA)

Meijer identified that the load line is dependent on the length of the air gap. When assuming a constant air gap, this discrepancy leads to an error in CP prediction and it decreases the accuracy of the feed-forward control supplying the demagnetization voltage, limiting the tuning speed. To compensate this, the air-gap length is measured and fed back in real time into the CP predictions and supply voltage calculations.

Fringe Flux-loss compensation (FF)

Up to this point, k_1 and k_2 have been assumed constant. However, Meijer identified that both k_1 and k_2 depend on the air-gap length. The sensitivity of k_2 to the air-gap length was identified to be small enough to be neglected, the sensitivity of k_1 however, can not be neglected. Using a magnetic FEA in COMSOL, an approximate relation between the air-gap length the loss factor k_1 is found. This relation is used in the CP prediction and uses the measured air-gap length:

$$k_1 = 2.44(-6.79 \cdot 10^4 l_g^2 + 4.76 \cdot 10^2 l_g + 0.59) \tag{2.17}$$

Parallel PI flux-feedback control (PPI)

Meijer added a PI controller to correct for any steady state errors.

Performance gains on these methods have been summarized in Table 2.1, all values here are in B_g.

Compensation method	*MAE* $[mT]$	*MAE* gain [%]	3σ $[mT]$	3σ gain [%]
None (reference)	19.81	-	2.38	-
DRS	8.72	55	1.92	19
DRS, DA & FF	7.55	61	0.78	67
DRS, DA, FF & PPI	6.75	65	0.75	68

Table 2.1: Performance comparison compensation methods, adapted from [25].

Minor-loop Magnetization State Tuning Meijer recognized that the tuning method developed by Viëtor was efficient for down-stepping, but required a saturation step for up-stepping, greatly reducing the efficiency of the method. It was proposed to overcome this problem by implementing the so called Minor-loop Magnetization State Tuning (MMST) method. This method linearizes the reversal curves from the descending to the ascending and from ascending to descending branch of the major loop. This allow for entering reversal curves on either side of with down-stepping performed on the descending branch and up-stepping performed on the ascending branch, as shown in figure 2.6.

The SMST and MMST methods are then compared on 4 areas, namely:

1. Mover dynamics

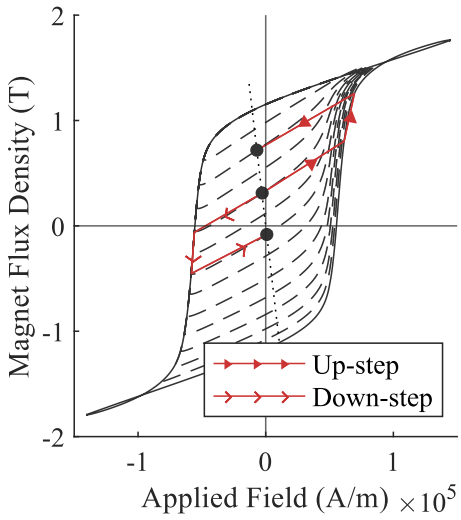

Figure 2.6: The MMST method with up-stepping and down-stepping assuming linear reversal curves.

2. Tuning time
3. Energy loss
4. Accuracy and Repeatability

Meijer showed great improvements on the first 3 areas. The mover dynamics were significantly reduced during the tuning cycle as well as the tuning time and the energy loss. However, the accuracy increased where the repeatability remained roughly the same. Table 2.2 summarizes the comparison between the tuning methods.

Area of Improvement	SMST baseline	MMST difference
Max. Deflection	791 μm	-84.1%
Tuning Times	575 ms	-9.7%
Energy Used	18.37 J	-51.3%
Accuracy (MAE)	7.1 mT	+50.4%
Repeatability (3σ)	0.7 mT	-17.3%

Table 2.2: Comparison SMST and MMST, adapted from [25].

Validation of the BTI Meijer validated the BTI of both the SMST and the MMST method at different tuning speeds and varying magnetization levels by measuring the current supplied to the magnetizing coil and calculating the copper losses. For both methods, the largest possible tuning step was used to estimate hysteresis losses. With the current setup, BTI values ranging from 120 to 5 seconds were achieved for the MMST and efficiency gains between the SMST and the MMST range from 20% to 90% between worst and best case. Finally, Meijer investigated the theoretical performance that could be achieved with the current setup when it is not limited by control hard- and software. Meijer found that BTI values between 1 and 0.29 seconds for a tuning range from 100 to 175mT can be achieved for the SMST, and 1 to 0.08 seconds in the range of 50 to 175mT for the MMST. Following equation 2.15, this leads to the theoretical efficiency bandwidth of 0.1 to 1.2Hz for the MMST.

3

Hysteresis Modelling for Efficient and Accurate Magnetization State Tuning of Soft Magnets

Hysteresis Modelling for Efficient and Accurate Magnetization State Tuning of Soft Magnets

Jasper Wiersema

***Abstract*—In this paper, the accuracy and efficiency of Magnetization State (MS) tuning in Tunable Magnet Actuators (TMAs) is investigated. TMAs are developed to improve thermal stability in quasi-static precision actuation applications. First, the operating principles of TMAs and limitations in previous work are discussed respectively. It is found that the linearization and simplification of magnetic hysteresis limit the accuracy and efficiency of the tuning process. Subsequently, a history dependent tuning algorithm and a generalized non-linear hysteresis modelling methodology are proposed. The tuning algorithm minimizes the energy loss by adhering to the hysteresis properties described by Madelung's rules. The hysteresis model uses measurement data to accurately calculate the applied field Corner Point (CP). Finally, the tuning algorithm and hysteresis model are experimentally validated for MS tuning of an AlNiCo-5 Permanent Magnet with an RMSE of 5.8 mT and theoretical tuning energies are reduced by as much as 86%.**

***Index Terms*—AlNiCo, magnetization state, hysteresis model, tunable magnets.**

I. Introduction

RELUCTANCE ACTUATORS (RA) are widely used magnetic actuators in the precision industry due to their high accuracy and high efficiency [1]. Advances in recent control theory allow for wider implementation of these actuators, despite their non-linear force-current relation [2], [3]. Applications range from magnetic gravity compensators [4], to lithography machines [5] and deformable space mirrors [6]. In these applications, large bias forces are needed and heat generation should be minimized due to the desired accuracy and the lack of convective cooling. However, the force-current relation of RAs shows that for a constant force, a constant supply of current is needed which heats up the system through copper losses in the windings of the flux generating coil. This can become a problem in precision systems that operate in quasi static operation with large bias forces in a vacuum or cryogenic environment as the produced heat deforms the system reducing the accuracy and repeatability of the machine.

The development of the Tuneable Magnet Actuator (TMA) aims to solve this problem using low coercivity Permanent Magnets (PM) such as AlNiCo [7], [8]. By using a PM as the source of the Magneto Motive Force (MMF), a constant bias force can be held without the constant use of energy. The PM can be magnetized and demagnetized by generating an external magnetic field using a coil wound around the PM. This allows Magnetization State (MS) tuning of the PM to any flux remanence inside the $B(H)$ curve of the PM.

Since the tuning process of the AlNiCo PM in TMAs is characterized by the non-linearity and history dependency of magnetic hysteresis, a hysteresis model is needed for accurate MS tuning. In the field of Variable Flux Memory Motors (VFMMs) [9], operator based models and analytical approximations of magnetic hysteresis have been used for this purpose [10]. Here, changing the magnetization of low coercivity PMs allows for flux weakening in the motor without the constant supply of current as is done in conventional synchronous motors [11]. Operator based models such as Preisach and Prandtl-Ishlinskii use the summation of an infinite number of mathematical operators to phenomenologically describe hysteresis [12]. Evaluating these models is computationally expensive due to the Everett function and backward calculations require an iterative numerical process [13], [14]. Analytical approximations have been developed to solve this problem, including a model based on Frölich equations [15], a piecewise linear model [16] and a non-linear model based on 5^{th} order polynomials [17]. The downside of these approaches is the reduced accuracy due to the simplifications made. The desire for an accurate model which is computationally inexpensive and allows for direct backward calculation from a desired MS to the Corner Point (CP), asks for a new modelling approach.

To further increase the applicability of the TMA, the tuning process should be as accurate and energy efficient as possible. Therefor, the contributions of this paper can be summarized as follows:

1) The description of the optimal MS tuning algorithm, minimizing the hysteresis and copper losses of the TMA.
2) The development of a novel, generalized hysteresis modelling approach suitable for accurate MS tuning of soft PMs.
3) The development of a novel estimation method allowing for MS tuning beyond the highest measured order $B(H)$ curves.

First preliminary knowledge on TMAs and hysteresis is provided in section II. Section III proposes the tuning algorithm and novel hysteresis modelling approach. The performance of the proposed contributions are experimentally validated and compared to previous work in section IV. Finally, section V concludes the paper.

II. Preliminaries

A. Magnetic Hysteresis

The major $B(H)$ curves of a magnetic material bound the reachable MS domain of the material. Magnetization states inside the major loop can be reached by reversing the external field from ascending to descending or vise versa when traversing the major loop. The point where the field is reversed is defined as the Corner Point (CP). The entered curve is referred to as a First Order Reversal Curve (FORC), for example curve 2-5-3-1 in Fig. 1. When reversing the magnetic field while traversing a FORC, the entered curve is called a Second Order Reversal Curve (SORC) (curve 5-2) and so on for higher order curves. A closed loop inside the $B(H)$ curve that consists of two reversal curves is called a minor loop (e.g. loop 2-5-2). The history dependent phenomena that describe how these reversal curves are traversed can be described by Madelung's rules [18]. The most important rules are summarized below using a modernized terminology [19]. The paths described can be seen in Fig. 1.

1) The path of any reversal curve is uniquely determined by the coordinates of the CP and its history (history dependency).
2) If any point 3 of curve 2-3-1 becomes a new CP, then curve 3-4-2 originating at point 3 returns to the initial point 2 (loop closure).
3) If point 4 of the curve 3-4-2 becomes the newest CP and the transition curve 4-3 extends beyond the point 3, it will pass along section 3-1 of curve 2-3-1 as if the previous closed loop 3-4-3 did not exist at all (wiping out property).

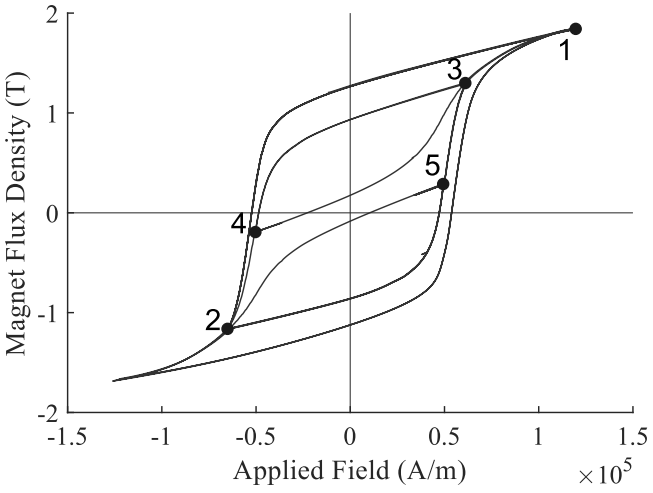

Fig. 1: Reversal curves for illustrating Madelung's rules for an AlNiCo-5 PM.

Besides these rate-independent hysteresis phenomena, there are also rate-dependent properties which depend on the rate of change of the external field. Most notably is the production of eddy currents between domain walls that limit the diffusion speed of induction [20]. These eddy currents cause loop-widening in the hysteresis curve which stretches the $B(H)$ curve along the H-axis.

B. Tunable Magnet Actuators

First introduced in [7], the TMA uses reversal curves to change the remanent MS of low coercivity PMs. The design is based on a conventional C-shaped RA with a magnet inside the coil as MMF source. The magnetic flux density of the magnet and the force acting on the mover are related as follows:

$$F_x = \frac{B_g^2 A_g}{\mu_0} \tag{1}$$

using

$$B_g = \frac{B_m A_m}{k_1 A_g} \tag{2}$$

with F_x being the force on the mover, subscripts g and m denote the gap and magnet respectively, B is the magnetic flux density, A the area and k_1 the fringe flux loss factor. Using Magnetic Equivalent Circuit (MEC) modelling, the load line of the circuit is derived and written as:

$$B_m = -\mu_0 \frac{k_1}{k_2} \frac{A_g l_m}{2 A_m l_g} (H_m - \frac{NI}{l_m}) \tag{3}$$

here l denotes length, N the number of coil windings, I the coil current and k_2 the MMF loss factor. The load line equation combines the permanent magnet with the magnetic circuit and is used to find the operating point of the magnet which is equal to the intersection of the load line and the hysteresis curve (Fig. 2). By changing the current in the coil, a shift in the load line is observed, allowing the traversal of hysteresis curves and thus MS tuning.

The first tuning approach implemented, called the Saturation Magnetization State Tuning method (SMST), relies on using the linear part of the FORCs originating on the descending branch of the major loop [7]. A lower MS is directly reached using a negative current pulse. However, a positive current pulse to saturate the magnet followed by a negative pulse is needed to reach a higher state, see Fig. 2a. The current set-point for the negative pulse is determined by calculating the shift needed for the load line (3) to intersect with the CP. The CP is determined by linearizing the $B(H)$-curves and finding the intersection between the major curve and the desired reversal curve.

A more efficient tuning approach called the Minor-loop Magnetization State Tuning (MMST) method aimed at removing the saturation step from the algorithm, as it is an inherently inefficient step using large currents [8]. The method uses linearized reversal curves originating from both the ascending as the descending major loop branch. This allows for entering reversal curves on either side with down-stepping performed on the descending branch and up-stepping on the ascending branch, see Fig. 2b.

The SMST was designed to only tune to positive fluxes due to the quadratic term in the force-flux relation (1). However, it can be more efficient to also tune to negative fluxes and use the ascending branch of the Major Loop as well. This approach is introduced as the extended version of the SMST (SMST-E) to make for a fairer comparison between tuning approaches in section IV. If a saturation step is needed, the SMST-E decides whether to use the ascending or descending branch of the Major Loop by minimizing the estimated hysteresis

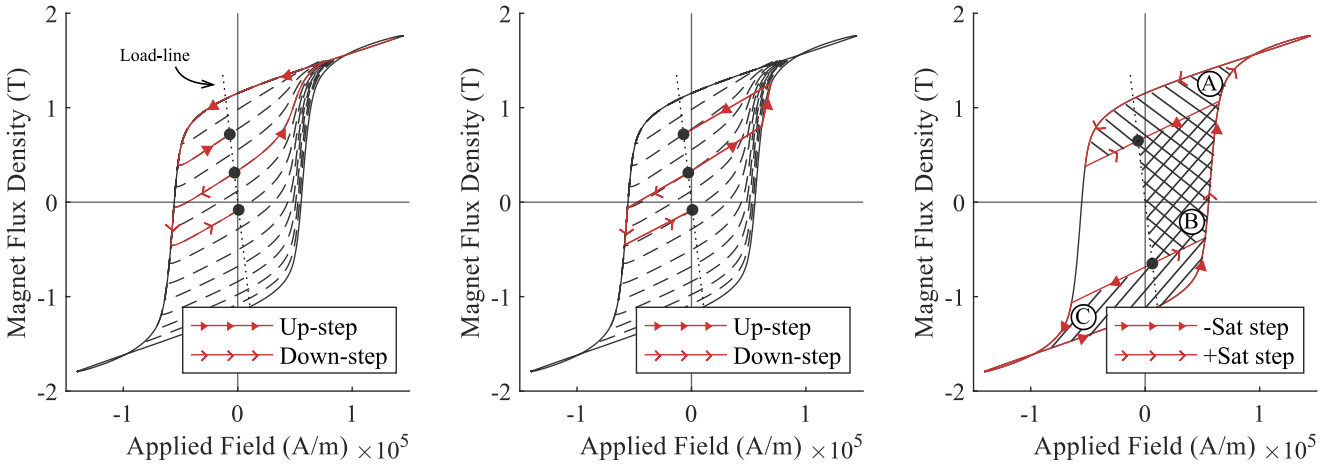

(a) SMST (b) MMST (c) SMST-E

Fig. 2: Tuning paths for different algorithms, here the black dots are the remanent MSs which lie on the intersection between load line and reversal curve. (a) Illustrates the tuning path of the SMST, where the up-step is realized by saturating the magnet. (b) Shows the same up-step for the MMST, showing a more efficient approach together with the linearization assumed for the reversal curves. (c) Illustrates the extension made to the SMST where during the saturation step the hysteresis losses are minimized.

losses of the tuning step. More concretely, this comes down to minimizing the area enclosed by the tune step in the $B(H)$ curve. By simplifying the $B(H)$ curve to a parallelogram, this simplifies to checking whether the absolute value of the desired MS is greater or smaller than the absolute value of the current MS as can be seen in Fig. 2c. Here the + saturation step encloses areas A and B and the - saturation step areas C and B. Area B has the same area independent of going through - or + saturation. Area A is larger than C in case of the new MS has a smaller absolute value than the previous MS due to symmetry of the $B(H)$ curve, making the - saturation step more efficient. Similarly, if the new MS has a larger absolute value, the + saturation step is more efficient.

III. Data Driven Hysteresis Modelling for Envelope Tuning

To change the MS of the AlNiCo PM in the TMA, a general tuning approach and hysteresis modelling methods are developed. An estimation method is developed to allow for MS tuning beyond the highest measured order reversal curves.

A. System Architecture

The TMA used in this work has a slight modification to the TMA used in previous work [7] [8]. Fig. 3 shows the schematic of the used TMA design. Laminated steel cores are used to minimize the rate-dependent effects of eddy currents. A fixed mover is used to remove any position dependencies in the load line and loss factors. Using MEC modelling, the load line equation of this circuit is determined as follows:

$$B_m = -\mu_0 \frac{1}{k} \frac{A_g l_m}{2 A_m l_g} (H_m - \frac{NI}{l_m}) \tag{4}$$

with k the total loss factor of the system.

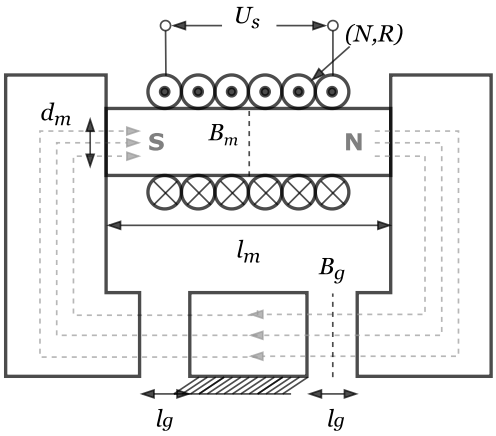

Fig. 3: Schematic overview of the used TMA.

B. Accuracy and Efficiency Optimization

To minimize the heat generation in the system during the tuning process, two properties of the tuning process should be minimized, the hysteresis losses and the copper losses due to Joule heating. The hysteresis losses are related to the area enclosed while traversing the $B(H)$ curve and the volume of the magnet as:

$$E_{hyst} = A_m l_m \int H_m dB_m \tag{5}$$

The coil losses are the time integral of the power in the coil:

$$E_{coil} = \int I(t)^2 R dt \tag{6}$$

The tuning approach can influence the path taken in the $B(H)$ curve to reach a certain magnetization state. The methodology should minimize the area enclosed and the

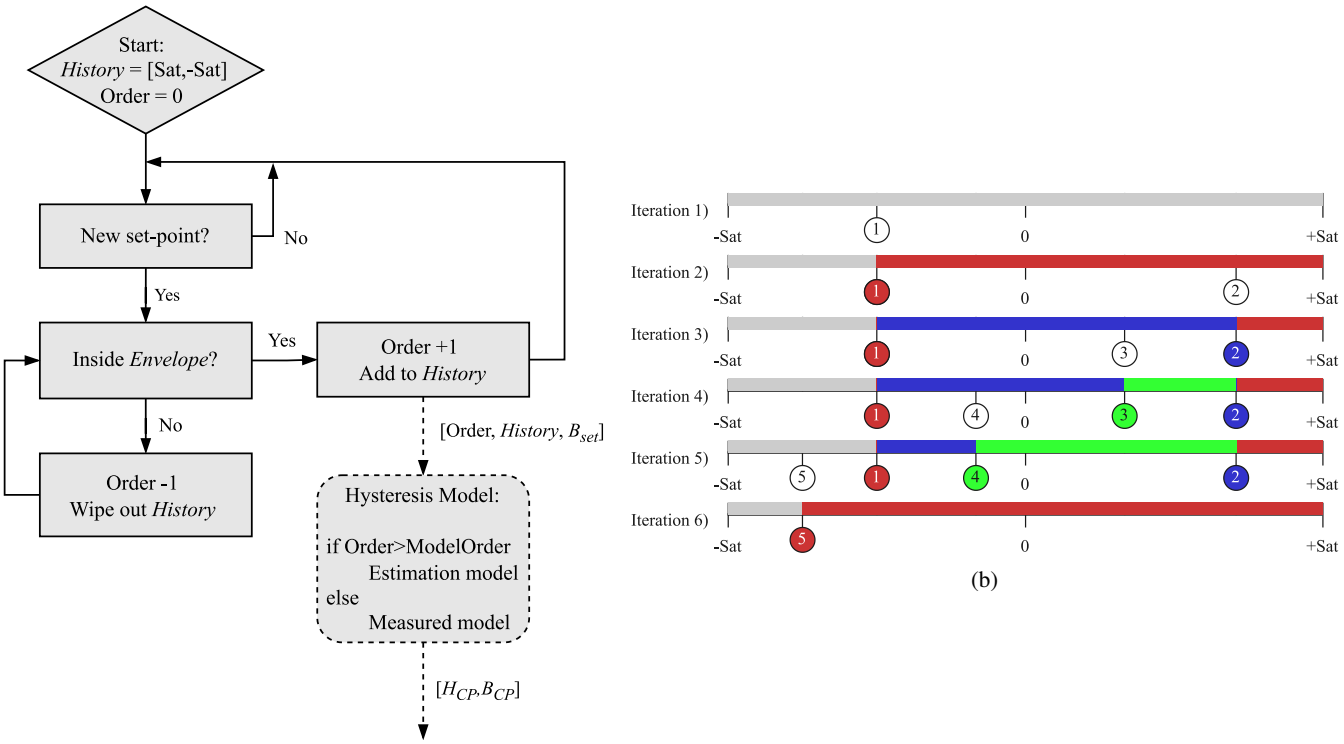

Fig. 4: (a): Envelope Magnetization State Tuning Algorithm. (b): Visual representation of how the algorithm progresses. The horizontal bar illustrates the reachable magnetization domain of the PM with new MSs in white and the *History* states coloured according to their order, with red, blue and green as first, second and third order respectively.

currents needed for this. The MMST minimizes both these variables by traversing the shortest path possible in the hysteresis curve. However, the MMST is history independent and uses linearized reversal curves, making the approach inherently inaccurate. Therefor, a non-linear history dependent approach which traverses the shortest path in the $B(H)$ curve should optimize for both efficiency and accuracy.

The requirements for how this approach should work can be derived from Madelung's rules as introduced in section II. Rule 1 states that every reversal curve is uniquely described by its CP and its MS history. Also, every reversal curve has a single remanent MS, thus the history of the reversal curve can be described by the sequence of previously reached remanent MSs. A history dependent hysteresis model could therefor calculate the CP based on the previously reached remanent MSs.

However, rules 2 and 3 introduce the loop closure and wiping out property of magnetic hysteresis. These properties influence the memory of the magnet by removing states from the history. Therefor, an algorithm needs to be developed which respects these properties and changes the history of remanent MSs accordingly.

C. Envelope Magnetization State Tuning

The Envelope Magnetization State Tuning (EMST) algorithm (Fig. 4) is proposed to keep track of the history of MSs and to find the order of the reversal curve of the desired remanent MS, B_{set}. The 1D array *History* refers to the history of MSs tracked. The path described in Fig. 5 shows an example of a few sequential tuning steps using the EMST method which is used to explain the algorithm. It is assumed that the start MS is at the positive saturated remanence point +*Sat* with reversal curve order 0 and *History* [+*Sat*,-*Sat*] (grey part in Fig 4b). When a new MS is desired (state 1), it is checked whether it lies within the last two values of *History*, which is referred to as the *Envelope*. If this is the case, the order of the reversal curve is increased and the new MS is added to *History*. This is illustrated in Fig. 4b, here state 1 lies in the grey part so the state is added to *History* and the order is increased to 1 (red). The same process is followed when moving to state 2 and 3 which lie on a SORC (blue) and Third Order Reversal Curve (TORC) (green) respectively. At state 3, *History* now consists of magnetization states [3,2,1+*Sat*,-*Sat*]. Continuing to state 4, it is observed that it does not lie within the *Envelope* which are state 3 and 2 (the green section). Following the wiping-out property of hysteresis, state 3 is removed from *History* and the order is decreased by 1. In the next iteration, state 4 does lie between the last two values resulting in a TORC and an *History* of [4,2,1,+*Sat*,-*Sat*]. In Fig. 4b this is easily visualized by observing that state 4 lies in the blue part of *History*. Finally, moving to state 5, three iterations are needed before the state lies in the *Envelope* spanned by +*Sat* and -*Sat*, reducing the order to FORC and *History* to [5,+*Sat*,-*Sat*]. This process can be continued indefinitely with any arbitrary

sequence of remanent MSs.

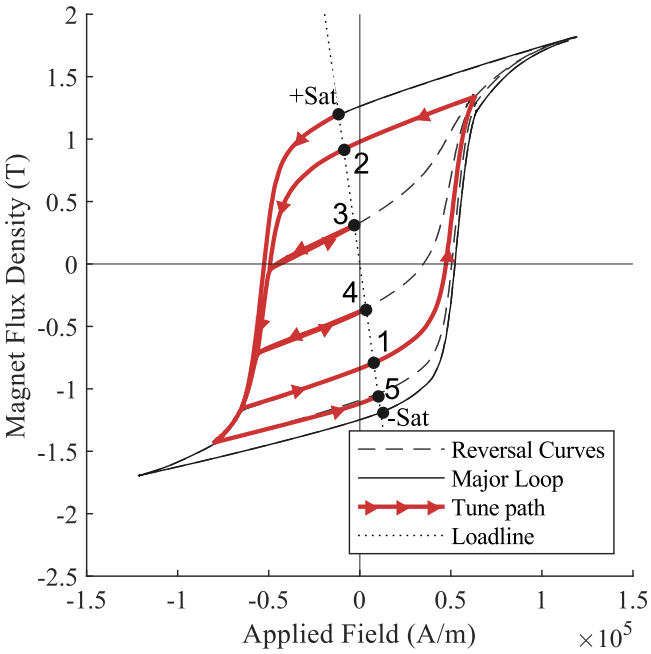

Fig. 5: EMST following the numbered remanent MSs in ascending order.

D. Data driven Hysteresis Modelling

Reaching a new MS accurately is directly dependent on accurately reaching the corresponding CP, as this will decide which reversal curve is entered and which remanence is reached. The hysteresis model should therefor output the coordinates of the CP for a given desired remanent MS and the history of remanent MSs.

The approach proposed here can be used to model up to any order reversal curve, however, for illustration purposes the process is shown for a second-order (SO) model. Reversal curves up to the modelled order need to be measured, in the case of a SO model this means a set of ascending FORCs and for every FORC a set of descending SORCs. The amount of reversal curves measured should be enough to capture the non-linear characteristics and can be limited to the domain of interest in the hysteresis curve. From the measurement data, the remanent MSs of the curves are found and matched to the CP of that remanence. For a set of reversal curves originating from the same lower order curve, this leads to two data sets that relate B_{rem} to H_{CP} and B_{CP} respectively, as shown in Fig. 6a. When modelling reversal curves higher than first order, multiple of these relations are found. For example, in case of a SO model, for every FORC a set of SORCs is measured and the mapping of B_{rem} to H_{CP} and B_{CP} is performed on each set, Fig. 6b shows multiple of these mappings from B_{rem} to H_{CP} with the respective FORC remanence. Using the FORC remanence, a continuous mapping of all SORC CPs can be constructed as shown if Fig. 6c.

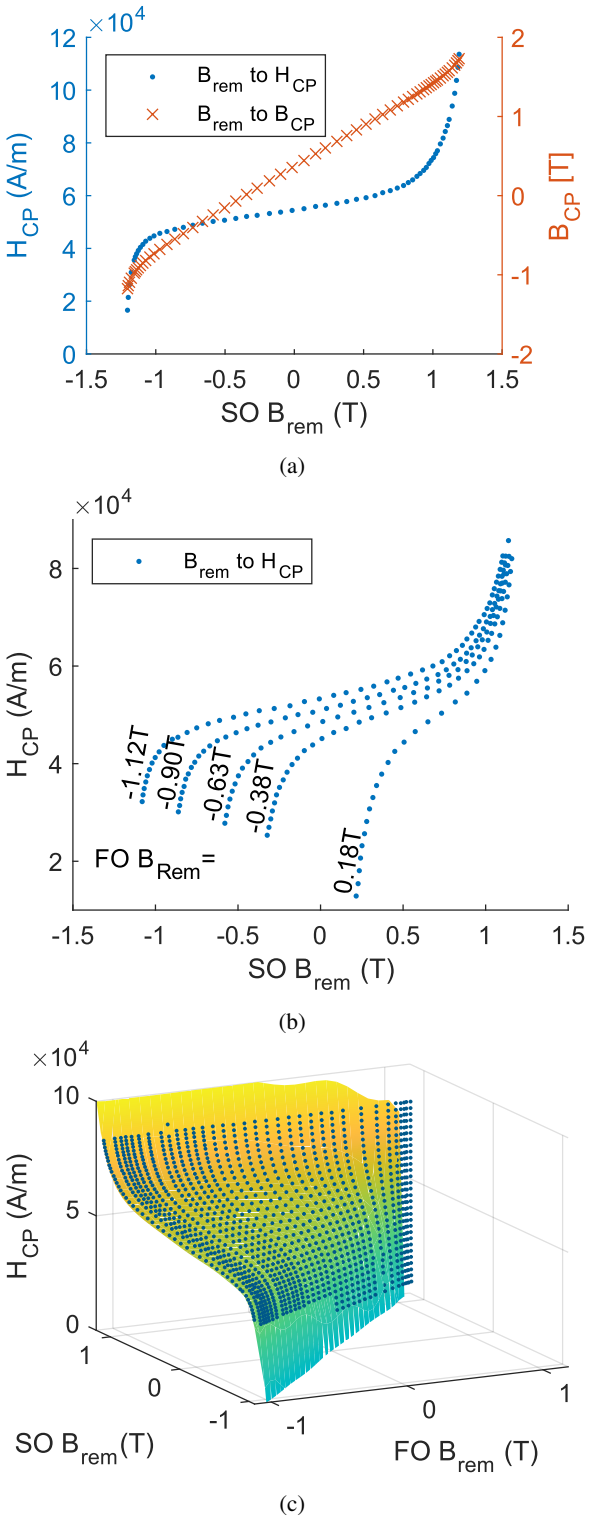

Fig. 6: (a): Mapping of B_{rem} to B_{CP} and H_{CP} for a set of SORCs originating from a single FORC. (b): Multiple mappings of B_{rem} to H_{CP} for different SORC sets with their respective FORC remanence. (c): All mappings in 3D with a polynomial fitted to the data, resulting in a SO model.

On the obtained continuous description, a multi-variable polynomial is fitted using the history of remanent MSs and the

desired remanence as variables and H_{CP} or B_{CP} as output. In case of the SO model, the history is completely determined by the FORC remanence. The polynomial order can be as high as desired as long as over-fitting is avoided.

E. Higher Order Estimation

The amount of data needed to model higher order reversal curves increases exponentially with every order, which leads to the desire to estimate higher order curves with lower order data to allow for continuous tuning without the need of a saturation step. Similarly to the modelling approach, the estimation approach can be applied to any order data.

The estimation is based on the observation that despite the order of the reversal curve, the curves show a linear behaviour between the CP and remanent state with similar slopes between orders, see Fig. 7. This allows for using the linear part of FORCs as transplants to estimate the linear section of higher order curves. This transplant is be found by finding the intersections of the highest measured order curve with the FORCs. Fig. 7 shows this for a SO model, with the intersections between SORCs and FORCs highlighted. The coordinates of these intersections are logged as the CP of the estimated curve. The remanence of the FORC is logged as the remanence of the estimated curve. Again, multi-variable polynomials are be used to relate the coordinates of the CPs to the desired remanence and the history of remanent MSs, which are the FORC and SORC remanence for estimation based on SO data.

To summarize, the final hysteresis model consists of multiple polynomials mapping the history of remament MSs and the desired MS to the coordinates of the CP. For every modelled order, two polynomials are needed, one for H_{CP} and one for B_{CP}. Two polynomials are added as an estimation model to increase efficiency by estimating reversal curve orders higher than the highest measured order. The EMST algorithm (Fig. 4a) tracks the order and the history of MSs, which are used by the model to select the correct polynomials and calculate the CP of the next tuning step.

IV. Performance Analysis and Validation

To validate and compare the performance of the tuning approaches and models proposed in this paper, different use cases are developed and applied to the experimental setup.

A. Experimental Setup

The TMA discussed in section III-A is realized for the experimental setup and is shown in Fig. 8. An AlNiCo-5 PM is used as the low-coercivity PM. The magnetizing coil is powered by two 30V sources connected to a linear power amplifier [7] to reach a $\pm$30V domain with a maximum current magnitude of 10A. The number of windings in the coil are chosen such that a high enough field can be generated to saturate the magnet. A hall sensor is placed in one of the actuator air gaps for gap flux density measurements. A current sensor is placed in the current path of the coil for coil current

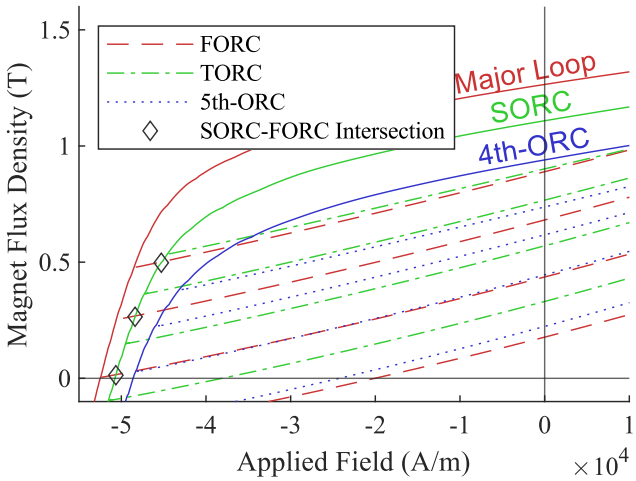

Fig. 7: Linear section of multiple order reversal curves of an AlNiCo-5 PM.

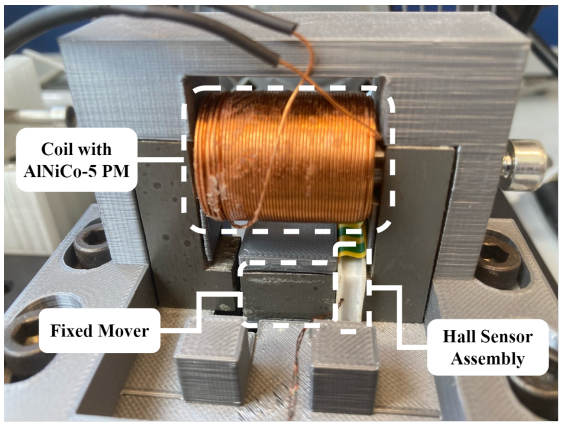

Fig. 8: Experimental TMA Setup

measurements. Using (2) the gap flux density is converted to magnet flux density. Magnet flux density and coil current are converted into external magnetic field using the load line (4) allowing the generation of $B(H)$ curves. The final system parameters are give in Tab. I.

TABLE I: Realized System Parameters

Symbol	Value	Comment
Actuator Parameters		
l_g	1.16 [mm]	Air gap length
A_g	100 [mm^2]	Air gap area
N_{coil}	655	Number of coil windings
R	3.75 [Ω]	Coil resistance
k	0.216	Loss factor
Magnet Parameters		
l_m	30.15 [mm]	Magnet length
d_m	9.9 [mm]	Magnet diameter
B_{rem}	1.25 [T]	Remanence
H_C	55 [kA/m]	Coercive field
μ_{max}	270 [Tm/A]	Maximum relative permeability
Other		
U	$\pm$ 30 [V]	Voltage range
r_{hall}	1 [mT]	Hall sensor resolution
$r_{current}$	1 [mA]	Current sensor resolution

Fig. 9 shows the implemented control scheme during the

TABLE II: Repeatability test, N=50

Order	$B_{m,set}$ [T]	1σ Sensor [mT]	1σ Tune [mT]	1σ [mT]
	1.15	0.48	0.26	0.55
1	0.8	0.42	0.85	0.95
	0	0.46	1.5	1.6
	0.15	0.47	1.2	1.3
2	0.5	0.44	1.8	1.9
	0.9	0.44	1.0	1.1
3	0.25	0.44	1.6	1.7

tuning process. A current controller and a flux controller were used during the validation. Only one controller is used at the same time and only to reach the CP, no feedback is used to reach the remanence. Appendix B contains a more detailed description of the controllers used.

B. Hysteresis Model Identification

For experimental validation of the modelling method and the proposed tuning algorithm, the FO and SO model for the AlNiCo-5 PM are identified together with the estimation models. The amount of reversal curves per measured set varies depending on the range of remanences in the set. The difference between two neighbouring reversal curves is chosen such that the non-linearities shown in Fig. 6a are properly captured. Polynomials ranging from order 3 to 50 are fitted to the data using the Vandermonde matrix and solving the system of equations [21]. The polynomials are tested on independent gathered data, calculating the Root Mean Square Errors (RMSE) of the CP calculation. The polynomial order of the final models are chosen by minimizing the RMSE and are found to be $N_{FO} = 25$ and $N_{SO} = 25$ with the following RMSEs:

- FO: $H_{\text{RMSE}} = 90$(A/m), $B_{\text{RMSE}} = 0.9$(mT)
- SO: $H_{\text{RMSE}} = 210$(A/m), $B_{\text{RMSE}} = 1.9$(mT)

where H_{RMSE} and B_{RMSE} are the RMSE values between calculated and measured CP coordinates.

C. Expected Model Performance

Using the current controller, a repeatability test is performed on the experimental setup using predefined set-points of different orders. Tab. II contains the results of this test, showing a tuning repeatability ranging from 0.55 to 1.9mT in B_m.

Transforming the RMSEs of the CP coordinates of the tested models in section IV-B to expected RMSE of the reached remanence, the expected systematic error can be calculated. By evaluating the load line (4) to find the error in load line shift and by linearizing the reversal curve with an assumed relative permeability of $\mu_{max}/2$, the error along the reversal curve can be found, see Fig. 10. For simplicity it is assumed that the value for B_{error} along the reversal curve translates 1:1 to the error at remanence. Performing this calculation and combining with the results of the repeatability tests give the following expected performance parameters of the models:

- FO: B_{rem} RMSE=6.3 mT, 1σ=1.6 mT
- SO: B_{rem} RMSE=13.5 mT, 1σ=1.9 mT

TABLE III: First Order Model Validation, N=20

FORC B_{set} [T]	RMSE [mT]	1σ [mT]
1.0000	1.9	1.8
0.7780	4.4	1.6
0.5560	8.3	1.9
0.3330	12.3	2.2
0.1110	10.5	2.5
-0.1110	11.6	1.6
-0.3330	12.3	1.9
-0.5560	7.6	1.8
-0.7780	4.2	1.3
-1.0000	2.3	1.5
Average	7.5	1.8

TABLE IV: Second Order Model Validation, N=20

FORC B_{set} [T]	SORC B_{set} [T]	RMSE [mT]	1σ [mT]
	-0.6	6.1	3.0
	-0.2	14.2	4.2
-1.0	0.2	4.5	4.1
	0.6	4.9	3.5
	1.0	6.6	2.2
	-0.2	7.1	2.1
	0.1	14.5	4.0
-0.5	0.4	10.3	3.3
	0.7	12.1	4.1
	1.0	7.5	2.0
	0.2	4.6	1.1
	0.4	12.3	2.2
0.0	0.6	5.7	3.1
	0.8	23.5	4.3
	1.0	9.1	1.9
Average	-	9.4	3.0

D. Validation

Tab. III and IV show the results of the FO and SO model validation which is summarized to:

- FO: B_{rem} RMSE=7.5 mT, 1σ=1.8 mT
- SO: B_{rem} RMSE=9.4 mT, 1σ=3.0 mT

Comparing this to the expected accuracy discussed in section IV-C, the models preform as expected or even better. This might be due to the simplification of $\mu_{rec} = \mu_{max}/2$ used. The linear model used in previous work realized the following static performance:

- Linear: B_{rem} RMSE=18mT, 1σ=1.9mT (converted from B_g to B_m [7].

A significant improvement in static MS tuning is observed. Therefor, for fair comparison between tuning algorithms, all algorithms are used with either the FO or SO model.

The different tuning algorithms are tested with the current controller and flux controller on the periodic and random use-case, Tab. V shows these results. The tests are repeated 20 times and the RMSE and 1σ of the MS tuning are calculated. Furthermore, the theoretical average energy loss per tuning cycle (E_{tune}) is shown. There is no difference in E_{tune} between the current controlled case and the flux controlled case, therefor it is removed from Table V to avoid repetition. Appendix A contains detailed descriptions on the use-cases and the calculation of E_{tune}.

Tab. VI shows the relative performance of the different approaches with respect to the SMST. It shows that using a current controller the SMST and SMST-E preform the best in terms of accuracy with the SMST-E the more efficient method. The MMST, EMST-FO and EMST-SO all greatly

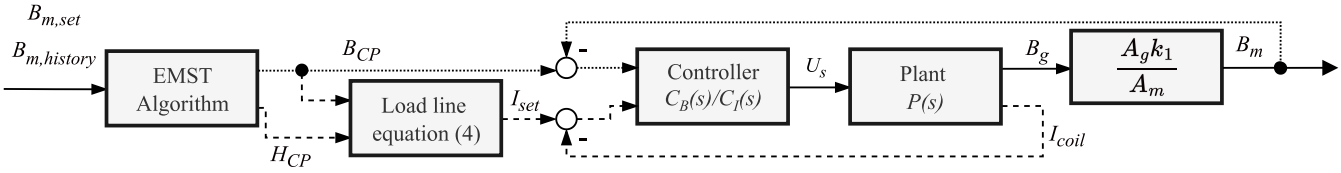

Fig. 9: Controller block diagram used to reach the desired CP, with the current controller in the dashed line and the flux controller in the dotted line. Note, only one of the controllers is active at the same time.

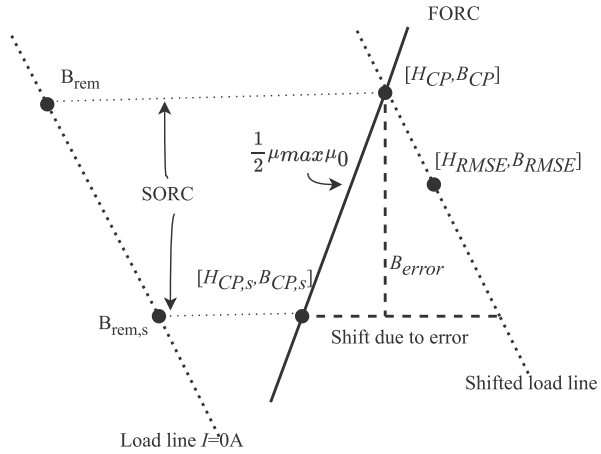

Fig. 10: Transforming the CP calculation error to model inaccuracy. Here $B_{rem,s}$ is the desired remanence and B_{rem} the achieved remanence due to modelling errors. [H_{RMSE}, B_{RMSE}] are the RMSEs of the CP calculation with respect to the correct CP [$H_{CP,s}$, $B_{CP,s}$], and [H_{CP}, B_{CP}] is the realized CP as the intersection of the shifted load line and the linearized reversal curve. Using trigonometry, B_{error} can be calculated.

TABLE V: Performance of different tuning algorithms

	SMST	SMST-E	MMST	EMST-FO	EMST-SO
Current Controlled, Periodic use-case					
RMSE [mT]	7.6	7.4	58.1	13.1	10.8
1σ [mT]	2.5	4.4	2.5	2.5	2.5
Etune [J]	1.16	0.915	0.162	0.161	0.158
Current Controlled, Random use-case					
RMSE [mT]	9.4	9.7	170	45.5	30
Etune [J]	1.55	1.25	0.224	0.204	0.269
Flux Controlled, Periodic use-case					
RMSE [mT]	6.2	7.1	10.1	6.7	5.3
1σ [mT]	3.1	0.83	1.8	0.83	0.92
Flux Controlled, Random use-case					
RMSE [mT]	5.3	4.8	34.5	10	5.8

reduce the tuning energy, but for the current controlled case lose a lot of accuracy. The flux controlled case shows very promising results for both the EMST-FO and EMST-SO where the accuracy is similar to that of the SMST methods while being as efficient as the MMST. In terms of repeatability, there is some variance between the methods using the periodic use-case, but the EMST performs consistently the best.

The great improvements realized with the flux controller can be attributed to two aspects. Firstly, the systematic modelling error of the methods is reduced by only considering flux density of the CP as a set-point, neglecting the error in

TABLE VI: Relative Performance to baseline set by SMST

	SMST	SMST-E	MMST	EMST-FO	EMST-SO
Current Controlled, Periodic use-case					
RMSE	100%	-3%	+664%	+72%	+42%
Etune	100%	-21%	-86%	-86%	-86%
Current Controlled, Random use-case					
RMSE	100%	+3%	+1708%	+384%	+219%
Etune	100%	-19%	-86%	-87%	-83%
Flux Controlled, Periodic use-case					
RMSE	100%	+15%	+62%	+8%	-15%
Flux Controlled, Random use-case					
RMSE	100%	-10%	+551%	+89%	+9%

H_{CP}. Besides this, loop-widening differences between model data and the experiments are canceled as different dI/dt profiles only change the H-response of the magnet but not the B-response. This especially improves the estimation model of the EMST. For example, for the SO estimation model, the intersections between SORCs and FORCs are used to identify the model. The current controller used during the data acquisition uses the point where the SORC closes the loop with its FORC as a set-point resulting in a specific dI/dt profile. During the validation however, the set-point for the controller is different as it is somewhere along the SORC, leading to a different dI/dt profile and therefor a difference in loop-widening effects. When the tuning order is in the measured regime of the model this effect is much smaller as the set-point during validation is a lot closer to the set-point used during data acquisition.

V. Conclusion

A general data driven hysteresis modelling approach has been proposed for implementation of the efficient Envelope Magnetization State Tuning (EMST) method. The hysteresis model can be extended to any order of measured reversal curves. The novel approach allows for accurate Corner Point (CP) calculations based on the history of the remanent Magnetization States (MSs) and the desired MS. The history of remanent MSs are mapped to CP coordinates and a multi-variable polynomial fit is performed to identify the model. In contrast to operator based modelling approaches, the CP calculation can directly be performed without the need of a recursive algorithm.

An estimation method of higher order tuning steps based on lower order data is proposed as an extension to the hysteresis modelling approach. The method allows for continuous MS tuning using the EMST to any higher order reversal curve without the need of higher order data. Using the linear nature and congruency property of reversal curves up until the

remanent MS, CPs are estimated as the intersection between the highest measured order curves and First Order Reversal Curves. Using the same procedure as in the general hysteresis model, the estimation model is identified.

First-Order (FO) and Second-Order (SO) hysteresis models are identified for an AlNiCo-5 permanent magnet in a Tuneable Magnet Actuator. Using an experimental setup, the hysteresis models are validated and have a RMSE of 7.5 mT for FO and 9.4 mT for SO with standard deviation of 2.5 mT in a -1 to 1T range.

The EMST is implemented using a FO and SO Estimation model. Using the experimental setup, the method is validated and compared to the previously introduced methods. Using a flux controller to reach the calculated CP flux density, a MS tuning RMSE of 10 mT and 5.8 mT for the EMST-FO and EMST-SO on a random continuous input are realized. The accuracy of the EMST-SO is as good as the SMST and SMST-E and significantly better than the MMST.

The EMST eliminates the need for saturation steps in the tuning process, reducing theoretical tuning energies by as much as 86% compared to the SMST and 83% compared to the SMST-E.

APPENDIX

A. Design of Experiments

Several use-cases are used to compare different order models and tuning methods. The identified FO and SO model are tested on a FO and SO use-case respectively. These use-cases are multiple MSs from -1 to 1T in the measured domain of the model to validate the expected performance. To compare the EMST to previously introduced tuning methods, two more general use-cases are developed. The first is following a sinusoidal MS trajectory. Using sampling theory, to follow a periodic signal, at least 10 samples per period are needed. Thus 10 samples following a sine function for $-1T \leq B_m \leq 1T$ are used. The second use-case is 10 randomly generated set points uniformly distributed between -1 and $1T$. This use case demonstrates general model accuracy as well as efficiency between different tuning approaches in a random application.

The metrics used to compare the models are the RMSE and the standard deviation (1σ) of the reached remanences and the theoretical average energy loss per tuning cycle (E_{tune}). The theoretical E_{tune} is the sum of the hysteresis losses in the magnet E_{hyst} and copper losses in the coil E_{copper}. By simplifying the hysteresis curve to a parallelogram and neglecting the load line [7], the hysteresis losses between tuning points can be calculated using:

$$E_{hyst,Sat} = V_m H_c(|B_{m,i} - B_{sat}| + |B_{sat} - B_{m,i-1}|) \quad (7)$$

$$E_{hyst} = V_m H_c(|B_{m,i} - B_{m,i-1}|) \quad (8)$$

where (7) is used when a saturation step is performed and (8) when there is no saturation step. $B_{m,i}$ is the reached remanent flux density and $B_{m,i-1}$ the previously reached remanent flux density.

The copper losses are calculated by integrating the I^2R losses over the theoretical fastest tuning times achievable with the used power supply:

$$\begin{aligned} E_{copper} = &\int_0^{T_{sat}} (\frac{U}{R}(1 - e^{-t\frac{R}{L}}))^2 R dt + \\ &\int_0^{T_{demag}} (I_{max} e^{-t\frac{R}{L}} - \frac{U}{R}(1 - e^{-t\frac{R}{L}}))^2 R dt + \\ &\int_0^{T_{decay}} (I_{min} e^{-t\frac{R}{L}})^2 R dt \end{aligned} \quad (9)$$

where the tuning times T are calculated using the current set-points returned by the tuning algorithm using:

$$\begin{aligned} T_{sat} &= \frac{L}{R} \ln(\frac{U}{U - I_{max}R}) \\ T_{demag} &= \frac{L}{R} \ln(\frac{U + I_{max}R}{U + I_{min}R}) \\ T_{decay} &= \frac{L}{R} \ln(\frac{I_{max}}{I_{min}}) \end{aligned} \quad (10)$$

where I_{max} is the saturation current ($I_{max} = 0$ if no saturation step is used for tuning), I_{min} is the demagnetization current and L is the Linearized Inductance [7] according to:

$$L = N^2(\frac{2kl_g}{\mu_0 A_g} + \frac{l_m}{A_m \mu_0 \mu_r})^{-1} \quad (11)$$

here μ_r is the relative permeability which is simplified to $\mu_r = \mu_{max}/2$ for the saturation and demagnetization step and to $\mu_r = 5$ for the decay step.

B. Controller Design

The output of the models, $[H_{CP}, B_{CP}]$, can be converted to a current set-point for the power amplifier using the load line (4). A current controller is implemented to change the voltage source to a current source. The transfer function of an RL-circuit is as follows:

$$P(s) = \frac{I}{U} = \frac{1}{Ls + R} \quad (12)$$

The inductance L varies during the tuning process as it is proportional to $\frac{dB}{dH}$. Assuming a worst case inductance, a proper PI controller can be designed which is tuned to control the current without overshoot, with the transfer function of the following form:

$$C_I(s) = \frac{U}{I} = k_p(\frac{L_C s + R_C}{s}) \quad (13)$$

The value for B_{CP} can also be used as a flux set-point for a flux controller. For this controller, it is assumed that there is a linear relation between coil current and flux density:

$$I_{coil} = \frac{1}{a} B_m \quad (14)$$

Using (13) and (14), a flux controller can be designed as:

$$C_B(s) = \frac{U}{B_m} = \frac{k_p}{a}(\frac{L_C s + R_C}{s}) \quad (15)$$

Both controllers are tuned on the setup such that no overshoot is observed, leading to the parameters shown in Tab. VII.

TABLE VII: Tuned Controller Parameters

Symbol	Value	Comment
R_C	3.75 Ω	Controller resistance
L_C	70E-3 H	Controller inductance
k_p	40	Gain
a	1.7	Flux gain

The controllers are only used to reach the calculated CPs, no feedback controller is active while traversing the reversal curve to the remanence.

REFERENCES

[1] N. H. Vrijsen, J. W. Jansen, and E. A. Lomonova, "Comparison of linear voice coil and reluctance actuators for high-precision applications," *Proceedings of EPE-PEMC 2010 - 14th International Power Electronics and Motion Control Conference*, DOI 10.1109/EPEPEMC.2010.5606572, no. October, 2010.

[2] R. M. Schmidt, G. Schitter, and A. Rankers, *The design of high performance mechatronics-: high-Tech functionality by multidisciplinary system integration*. Ios Press, 2020.

[3] S. Ito, F. Cigarini, and G. Schitter, "Flux-Controlled Hybrid Reluctance Actuator for High-Precision Scanning Motion," *IEEE Transactions on Industrial Electronics*, vol. 67, DOI 10.1109/TIE.2019.2952829, no. 11, pp. 9593–9600, 2020.

[4] S. Hol, *Design and optimization of a magnetic gravity compensator*, no. 2004, 2004. [Online]. Available: http://www.narcis.nl/publication/RecordID/oai:library.tue.nl:574485

[5] "Asml euv lithography systems." [Online]. Available: https://www.asml.com/en/products/euv-lithography-systems

[6] S. Kuiper, N. Doelman, E. Nieuwkoop, T. Overtoom, T. Russchenberg, M. van Riel, J. Wildschut, M. Baeten, J. Human, H. Spruit, S. Brinkers, and M. Maniscalco, "Electromagnetic deformable mirror development at TNO," in *Advances in Optical and Mechanical Technologies for Telescopes and Instrumentation II*, vol. 9912, DOI 10.1117/12.2230891, p. 991204. SPIE, 7 2016.

[7] S. Viëtor, "Tunable Magnets: Modeling and Validation for Dynamic and Precision Applications," *Thesis Topology*, no. February, pp. 5–7, 2018.

[8] Meijer Romano, "Tunable Magnets: Dynamic Flux-feedback Compensation Methods for Improved Magnetization State Tuning Performance and Minor-loop Magnetization State Tuning for the Validation and Reduction of the Break-even Tuning Interval," no. February, 2021.

[15] H. Yang, R. Tu, T. Wang, S. Lyu, and H. Lin, "Investigation of field regulation mechanism of flux-reversal variable flux memory machine by an improved frolich hysteresis model," *2020 8th International Conference on Power Electronics Systems and Applications: Future Mobility and Future Power Transfer, PESA 2020*, DOI 10.1109/PESA50370.2020.9343995, 2020.

[9] V. Ostovic, "Memory motors - A new class of controllable flux PM machines for a true wide speed operation," *Conference Record - IAS Annual Meeting (IEEE Industry Applications Society)*, vol. 4, DOI 10.1109/ias.2001.955983, no. C, pp. 2577–2584, 2001.

[10] H. Yang, H. Lin, S. Fang, Z. Q. Zhu, and Y. Huang, "Flux-regulatable characteristics analysis of a novel switched-flux surface-mounted PM memory machine," *IEEE Transactions on Magnetics*, vol. 50, DOI 10.1109/TMAG.2014.2323331, no. 11, 2014.

[11] T. M. Jahns, "Flux-weakening regime operation of an interior permanent-magnet synchronous motor drive," *IEEE Transactions on Industry Applications*, vol. IA-23, DOI 10.1109/TIA.1987.4504966, no. 4, pp. 681–689, 1987.

[12] M. Al Janaideh, S. Rakheja, and C. Y. Su, "An analytical generalized Prandtl-Ishlinskii model inversion for hysteresis compensation in micropositioning control," *IEEE/ASME Transactions on Mechatronics*, vol. 16, DOI 10.1109/TMECH.2010.2052366, no. 4, pp. 734–744, 2011.

[13] V. Hassani, T. Tjahjowidodo, and T. N. Do, "A survey on hysteresis modeling, identification and control," *Mechanical Systems and Signal Processing*, vol. 49, DOI 10.1016/j.ymssp.2014.04.012, no. 1-2, pp. 209–233, 2014. [Online]. Available: http://dx.doi.org/10.1016/j.ymssp.2014.04.012

[14] M. A. Vasquez-Beltran, B. Jayawardhana, and R. Peletier, "Recursive Algorithm for the Control of Output Remnant of Preisach Hysteresis Operator," *IEEE Control Systems Letters*, vol. 5, DOI 10.1109/LCSYS.2020.3009423, no. 3, pp. 1061–1066, 2021.

[16] C. Yu, S. Niu, S. L. Ho, W. Fu, and L. Li, "Hysteresis modeling in transient analysis of electric motors with AlNiCo magnets," *IEEE Transactions on Magnetics*, vol. 51, DOI 10.1109/TMAG.2014.2362615, no. 3, pp. 14–17, 2015.

[17] H. Liu, H. Lin, Z. Q. Zhu, M. Huang, and P. Jin, "Permanent magnet remagnetizing physics of a variable flux memory motor," *IEEE Transactions on Magnetics*, vol. 46, DOI 10.1109/TMAG.2010.2044638, no. 6, pp. 1679–1682, 2010.

[18] E. Madelung, *Über magnetisierung durch schnellverlaufende ströme und die wirkungsweise des rutherford-marconischen magnetdetektors*. JA Barth, 1905.

[19] S. E. Zirka, Y. I. Moroz, P. Marketos, and A. J. Moses, "Congruency-based hysteresis models for transient simulation," *IEEE Transactions on Magnetics*, vol. 40, DOI 10.1109/TMAG.2004.824137, no. 2 I, pp. 390–399, 2004.

[20] G. Bertotti, *Hysteresis in Magnetism: For Physicists, Materials Scientists, and Engineers*, 1998.

[21] D. Kalman, "The generalized vandermonde matrix," *Mathematics Magazine*, vol. 57, DOI 10.1080/0025570X.1984.11977069, no. 1, pp. 15–21, 1984. [Online]. Available: https://doi.org/10.1080/0025570X.1984.11977069

4

Conclusion

The research goal of this thesis was defined as follows:

Develop a continuous tuning algorithm combined with a non-linear and history dependent hysteresis model to allow for efficient and accurate magnetization state tuning.

In this chapter, this goal will be reflected on by concluding on the objectives defined. Furthermore, recommendations for future work are suggested to further improve the applicability of TMAs.

4.1. Conclusion

To describe a tuning approach which respects the non-linear and history dependent characteristics of magnetic hysteresis.

The existing tuning algorithms in the TMA state of the art, the SMST and MMST, both had their respective downsides. The SMST only uses First Order Reversal Curves and therefor needs the inefficient saturation step during the tuning process. The MMST neglects the history dependency of the hysteresis curve, leading to inaccurate MS tuning. The Envelop Magnetization State Tuning (EMST) method is developed, which adheres to the hysteresis phenomena described by Madelung's rules. The method is realized by implementing the algorithm shown in Fig. 4.1a which tracks the *History* MSs and uses these to find the order of the reversal curve used to reach the desired MS while minimizing the losses during the tuning process. The EMST is based on the wiping-out and loop-closure properties of magnetic hysteresis and is visualized in Fig. 4.1b. The result is a method which allows for continuous MS tuning with minimized Joule heating and hysteresis losses, while correctly tracking the magnetic hysteresis.

To develop a generalized hysteresis modelling approach based on measurement data.

The linear hysteresis model used in previous work is not sufficient to combine with the EMST. A novel and non-linear hysteresis model is proposed such that the EMST can be implemented. It is observed that the hysteresis model only needs to provide a relation between the desired MS, the previously reached MSs and the coordinates of the corresponding CP. A general data driven modelling approach is described which maps the remanent MS of measured reversal curves to the CP coordinates and uses the remanences of the lower order curves to create a continuous space on which multi-variable polynomials are fitted.

The result is a general description of hysteresis useful for MS tuning by directly allowing CP calculations based on the magnetization history and the desired MS.

Furthermore, an estimation method of higher order tuning steps based on lower order data is proposed as an extension to the hysteresis modelling approach. The estimation method allows for continuous MS tuning using the EMST to any higher order reversal curve beyond the highest measured order.

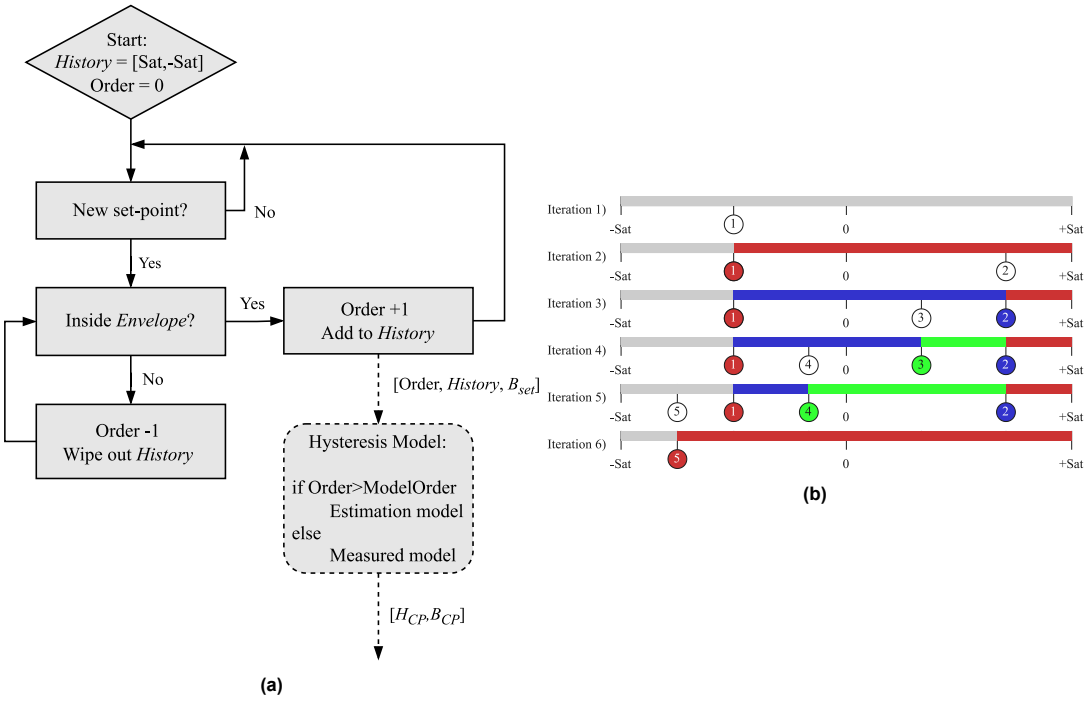

Figure 4.1: (a): The EMST algorithm. (b): Visual representation of how the algorithm progresses. The horizontal bar illustrates the reachable magnetization domain of the PM with new magnetization states in white and the *History* states coloured according to their order, with red, blue and green as first, second and third order respectively.

Using the linear nature and slope similarities of reversal curves of different order up until the remanent MS, CPs are estimated as the intersection between the highest measured order curves and FORCs. Using the same procedure as in the general hysteresis model, the estimation model is identified.

To validate the performance of the tuning algorithm and hysteresis modelling approach.

An experimental setup of a simplified TMA with a fixed mover is build for validation of the proposed algorithm and modelling approach. The fixed mover is used to remove any position dependencies between the measured gap flux density and the magnet flux density.

A First Order (FO) and Second Order (SO) model are identified and tested on a number of set-points between -1 an 1T using a current controller to reach the CP to validate their accuracy with the average performance as follows:

- FO: B_{rem} RMSE=7.5 mT, 1σ=1.8 mT
- SO: B_{rem} RMSE=9.4 mT, 1σ=3.0 mT

The linear model used in previous work realized a static performance of:

- Linear: B_{rem} RMSE=18 mT, 1σ=1.9 mT (converted from B_g to B_m [39])

Comparing these results, Root Mean Square Error (RMSE) improvements of 58% and 48% for FO and SO models respectively is realized.

The EMST is validated by using two use-cases, a periodic magnetization state trajectory following a sine function between -1 and 1T and a sequence of random magnetization states uniformly distributed between -1 and 1T. Both a current controller and a flux controller have been implemented to reach the calculated CP. The SMST, SMST-E and MMST are all implemented with the identified FO model to allow for comparison between the EMST and previously implemented algorithms. The EMST is implemented using the FO and SO model, both with their respective estimation extensions. The algorithms are compared on RMSE and average theoretical energy loss per tuning cycle E_{tune}. Table 4.1 summarizes the results and shows the relative performance to the SMST baseline.

From these results, several things can be concluded. The EMST reduces the energy loss by as much 86% with respect to the SMST and 83% with respect to the SMST-E, which is a significant improvement and as much as the MMST achieved. The EMST generally looses accuracy with respect to the SMST, however, it significantly improves compared to the MMST. Also, the SO model improves the accuracy in all cases compared to the FO model. Lastly, the EMST with a SO model and a flux controller performs as well as the SMST in terms of accuracy, however, the increased efficiency of the EMST makes it the preferred tuning approach.

Table 4.1: Algorithm Comparison

	SMST		SMST-E		MMST		EMST-FO		EMST-SO	
Current Controlled, Periodic Use-Case										
RMSE (mT)	7.6	100%	7.4	-3%	58.1	+664%	13.1	+72%	10.8	+42%
1σ (mT)	2.5	-	4.4	-	2.5	-	2.5	-	2.4	-
E_{tune} (J)	1.16	100%	0.915	-21%	0.162	-86%	0.161	-86%	0.158	-86%
Current Controlled, Random Use-Case										
RMSE (mT)	9.4	100%	9.7	+3%	170	+1708%	45.5	+384%	30	+219%
E_{tune} (J)	1.55	100%	1.25	-19%	0.224	-86%	0.204	-87%	0.269	-83%
Flux Controlled, Periodic Use-Case										
RMSE (mT)	6.2	100%	7.1	+15%	10.1	+62%	6.7	+8%	5.3	-15%
1σ (mT)	3.1	-	0.83	-	1.8	-	0.83	-	0.92	-
Flux Controlled, Random Use-Case										
RMSE (mT)	5.3	100%	4.8	-10%	34.5	+551%	10	+89%	5.8	+9%

By summarizing the conclusions, the contribution of this thesis is visualized in Figure 4.2, and can be described as follows:

By implementing the Envelope Magnetization State Tuning method combined with a non-linear and history dependent model, continuous magnetization state tuning is achieved. Validation shows that the hysteresis model improves the static accuracy with approximately 50% compared to previous work, and that the flux controlled EMST is as efficient as the MMST without sacrificing accuracy compared to the SMST.

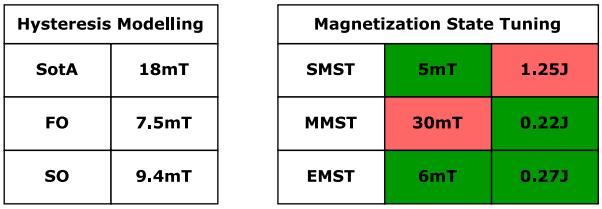

Figure 4.2: Contribution Summary

4.2. Discussion

Looking at the results summarized in table 4.1, two important points of discussion should be addressed. Namely, the inaccuracy of the EMST in the current controlled case, and the great relative performance gain of the EMST in the flux controlled case.

Current Controlled Estimation Inaccuracy Looking at the accuracies of the EMST to the SMST in the current controlled case, it can be seen that the SMST performs as expected from the model validation results discussed earlier. The same can be said about the EMST-SO on the periodic use-case, but besides this, the EMST preforms poorly. This shows that when the estimation models start to play a part in the tuning process, the accuracy of the magnetization state tuning degrades. In the random use-case this is exceptionally clear as relatively high order reversal curves are reached. The

SMST will always stay in the measured domain of the hysteresis curve and therefor does not lose significant accuracy between the two use-cases.

The relatively poor performance of the estimation model in the current controlled case can largely be attributed to the rate-dependent effects of loop-widening. As discussed in chapter 2, the $B(H)$ response of the magnet is dependent on the rate of change of the applied field which is directly proportional to dI/dt. To identify the estimation model, the non-linear part of reversal curves are measured up to the loop-closure point. This point has been used as a set-point for the current controller resulting in a specific dI/dt profile for that specific reversal curve. The intersections of FORCs with this non-linear section are used to identify the estimation model. During tuning, when one of these intersections is used as CP, this point is used as set-point for the current controller, resulting in a different dI/dt profile which causes loop-widening errors between the model and the reality. When the desired MS is within the measured domain, the difference in measurement set-point and tune set-point is much smaller, resulting in less loop-widening. Fig. 4.3a and 4.3b show the difference in CP calculation of the FO estimation model between the implemented case and the case where there is no difference in dI/dt respectively. It shows that there is a clear improvement in CP calculation when the loop-widening effects are reduced. Fig. 4.3b is obtained by using the same set-point for the current controller as is used for the identification data, but the current is set to zero before it reaches this set-point. This data is then used to perform off-line CP calculations for the measured remanent states. Since there is no model for when to set the current to zero for a certain remanent MS, this is not a solution for real-time implementation.

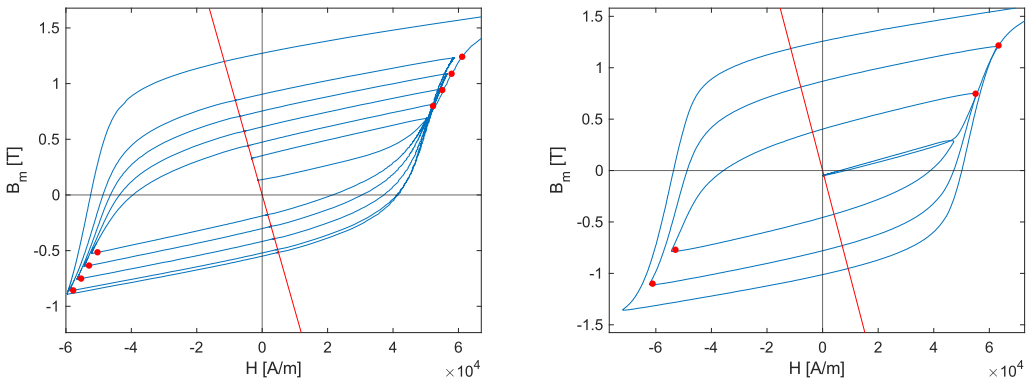

Figure 4.3: (a): The estimation model as implemented during experiments, where the red dots are the estimated CPs. (b): The estimation model where both the model data as the test data have the same dI/dt profile.

Flux Controlled Performance By implementing a flux controller instead of a current controller for reaching the CP, all algorithms experience an improvement in accuracy. This can be attributed to the fact that by using B_{CP} as a set-point for the flux controller, modelling errors in H_{CP} are removed. However, this does not explain why the EMST improves relatively more than the SMST. The flux controller also reduces loop-widening effects significantly, as these errors mostly influence H_{CP} as loop-widening stretches the $B(H)$ curve along the H-axis. A flux controller is therefor a very effective way to reduce modelling errors for both the hysteresis model as the estimation model.

4.3. Recommendations

The contribution of the thesis improves the applicability of TMAs for industrial applications. However, there are still improvements to be made on dynamic implementation and tuning speed. Also, since the hysteresis modelling approach described here is very general, it would be interesting to look at how it can be used for other applications dealing with hysteresis. To further elaborate on these points, several recommendations are given below.

1. **Dynamic Implementation of the EMST.** In this thesis, the focus was on development of a general solution to the MS tuning problem. By using a static version of the TMA, it was possible to easily

convert gap flux measurements to magnet flux. The methodology described in this thesis should be extended to a dynamic TMA setup to further proof the applicability of this actuator design. The following steps are recommended to achieve this:

- **Develop load line and actuator model:** For now, let's assume that the control variable of the dynamic set-up is position. A model is needed which corrects the load line due to the position change. An actuator model is also needed to calculate the force needed for the desired displacement and from there, the desired flux density in the gap is calculated. The gap flux density can be converted to magnet flux density using a position corrected fringe flux loss factor.
- **Develop load line compensation method:** Since the model is identified for the mover in the mid position, a change in position will change the load line and therefor the remanence. Directly using the hysteresis model without any compensation can result in large errors. By linearizing the reversal curves between the extremes of the load line (see Fig. 4.4a) and by mapping the remanent states of the mid position load line to the slope of the reversal curve (Fig. 4.4b), a linear relation can be found which can be used to convert the remanence of the corrected load line to the remanence of the mid position load line along this linearized reversal curve. The mid position remanence can than be used in the hysteresis model and the CP is calculated for the correct reversal curve.

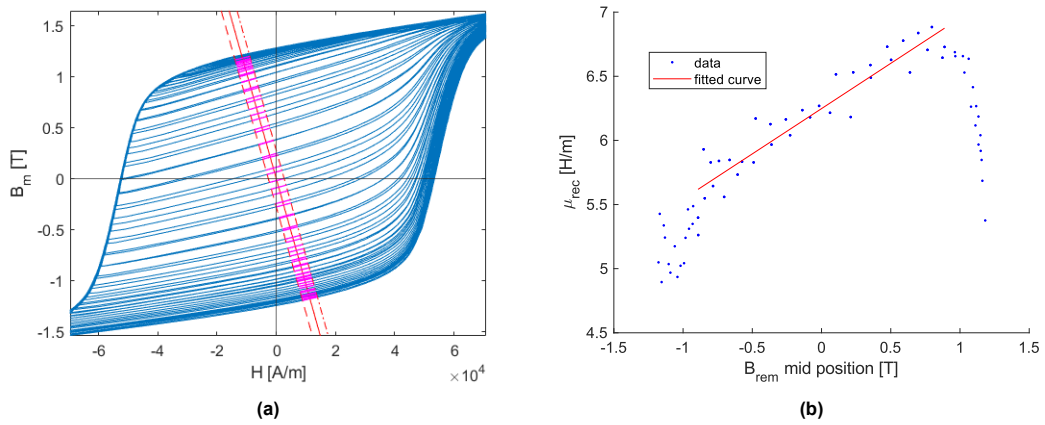

Figure 4.4: (a): The load lines at the extreme positions of the mover are used to linearize the reversal curves around the mid position load line (magenta lines). (b): A linear relation between -1 and 1T can be found between the mid position remanences and the slopes of the linearized reversal curves

- **Implement for dynamic tuning:** The dynamic compensation methods discussed should be implemented in real-time and validated. Fig. 4.5 illustrates how the compensation methods could be implemented in the tuning algorithm.

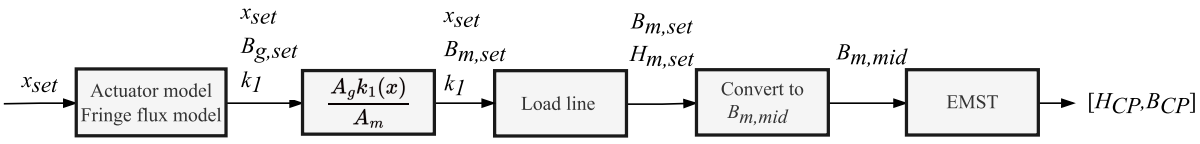

Figure 4.5: Dynamic compensations block diagram.

2. **Improved Flux Controller Design.** The controller design used in this work is far from optimal and resulted in very slow tuning times. The focus here was to have a controller which would not overshoot the CP and which had a high repeatability to improve the quality of the acquired data. To push the tuning times of the TMA towards the theoretical limits, a better designed controller should be implemented. Specifically, a better flux controller should be designed as this has significant benefits over current control by reducing modelling errors and reducing errors due to loop-widening. Important to note is, that for flux control, B_m is controlled while B_g is measured. So similar to recommendation 1, a position dependent conversion should be implemented.

- **Implement FPGA based processor, or faster micro controllers:** In this thesis, the NIDAQmx USB module is used which has a relatively slow interaction between module and PC. This limits the bandwidth of controllers since the program does not compile externally but on your laptop. By either moving to an FPGA based processor, or a faster micro controller board (from TI for example), higher control bandwidths can be achieved and tuning times can be significantly reduced.
- **Design a Flux Controller to reach the Corner Point:** The non-linear characteristics of the $B(H)$-curve make controller design challenging due to the variable inductance. Also, the non reversibility of hysteresis poses challenges as overshooting the CP will result in significant errors as your maximum dictates what reversal curve you enter. The optimal controller would be a bang-bang type controller which switches the supply voltage from -30V to 30V exactly at the CP. However, this might not be possible due to delays or other dynamic effects. This could be investigated and a controller which approaches this optimal controller could be designed.
- **Design a Feed Forward Controller to reach the remanence:** Between the CP and the desired MS, the reversal curves are close to linear resulting in a constant inductance. The slopes of reversal curves can be modelled as is done in previous work. This could be used to design a feed forward controller to provide a voltage pulse to push the current to zero as fast as possible, increasing the efficiency and the tuning times.

3. **Develop and implement a reversal curve slope based controller:** Table 4.1 reveals a great improvement for the MMST when a flux controller is implemented. It also shows that there is a significant difference between periodic and random use-case. These results show that the MMST is still inaccurate, however, it does show potential due to its simplicity. Also, by implementing the estimation models, we've shown that the slopes of different order reversal curves are similar in the linear regime, and that this can be used for reversal curve estimation. This idea can be used to further improve the accuracy of the MMST.

   Currently, the MMST calculates the CP on a FORC with a slope similar to the slope of the higher order reversal curve. By calculating the slope between the operating point and the calculated CP, and comparing it the the slope of the FORC, a controller can be designed which reverses the field when the operating point of the magnet crosses the FORC. Figure 4.6 explains this visually. This controller could improve the accuracy of the MMST to approach the accuracy of the EMST. If this would be achieved, and tuning times are not significantly influenced, then the MMST could be a better solution for the MS tuning problem than the EMST due to its simplicity.

4. **Extension to the Remnant Control problem in Hysteretic Deformable Mirrors (HDMs):** By using the remanent state of piezoelectric actuators, HDMs are developed for space applications [33]. Using a Preisach operator based hysteresis model, a feedforward control input is determined to reach the desired remnant state [38]. Due to the nature of operator based models, a recursive algorithm is introduced to determine this control input, and currently multiple iterations of the computationally expensive model are needed before the control input has converged.

   In this work, the remnant control problem is solved in a different way. By using the data driven hysteresis modelling approach together with the history dependent tuning algorithm, no recursive algorithm is needed to calculate the control input while accurate remnant states are achieved. It could be interesting to investigate whether HDMs and piezoelectric actuators could benefit from the methodology presented in this thesis to improve computational efficiency while maintaining accurate actuation.

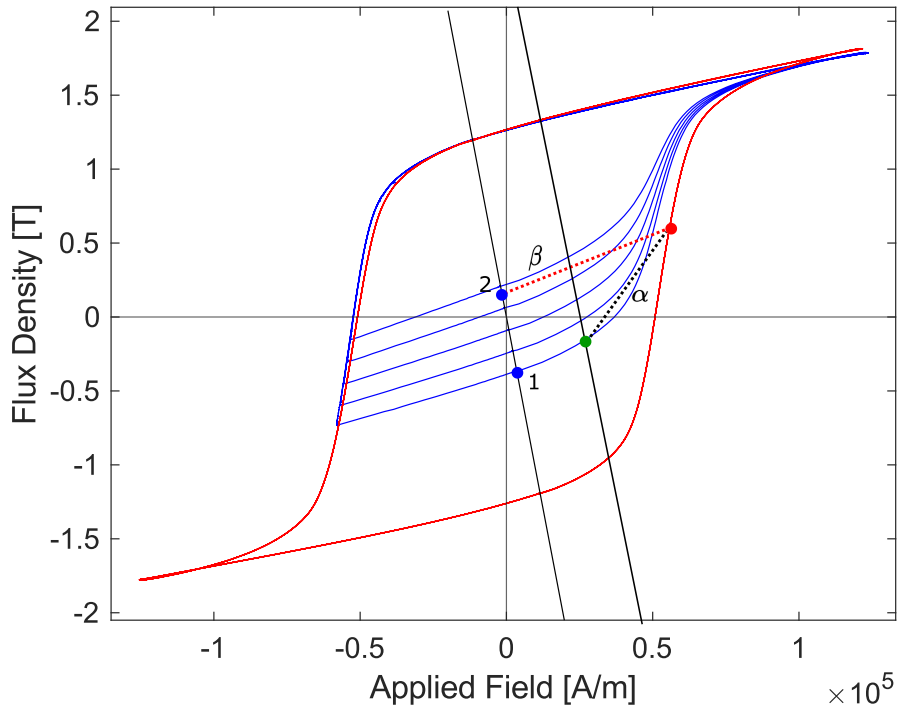

Figure 4.6: Reversal curve slope based controller. Here, the tuning step is from point 1 to point 2, the green dot represents the operating point and the red dot the calculated CP. By reducing the error between slopes α and β, the higher order reversal curve can be estimated using the MMST.

References

[1] Ahmet Cecen (2022). *Multivariate Polynomial Regression*. Retrieved July 1, 2022. URL: https://github.com/ahmetcecen/MultiPolyRegress-MatlabCentral.

[2] NS (2022). *Curve intersections*. Retrieved July 5, 2022. URL: https://www.mathworks.com/matlabcentral/fileexchange/22441-curve-intersections.

[3] Mohammad Al Janaideh, Subhash Rakheja, and Chun Yi Su. "An analytical generalized Prandtl-Ishlinskii model inversion for hysteresis compensation in micropositioning control". In: *IEEE/ASME Transactions on Mechatronics* 16.4 (2011), pp. 734–744. ISSN: 10834435. DOI: 10.1109/TMECH.2010.2052366.

[4] *ASML EUV lithography systems*. URL: https://www.asml.com/en/products/euv-lithography-systems.

[5] Giorgio Bertotti. *Hysteresis in Magnetism: For Physicists, Materials Scientists, and Engineers*. 1998, p. 558. ISBN: 0120932709.

[6] John R. Brauer and Isaak D. Mayergoyz. "Finite-element computation of nonlinear magnetic diffusion and its effects when coupled to electrical, mechanical, and hydraulic systems". In: *IEEE Transactions on Magnetics* 40.2 II (2004), pp. 537–540. ISSN: 00189464. DOI: 10.1109/TMAG.2004.824591.

[7] Peter Campbell. "Permanent magnet materials and their application". In: (1996).

[8] Barbara Cannas, Silvano Cincotti, and Ivano Daneri. "A generalization of a piece-wise linear circuit model of hysteresis". In: *IEEE Transactions on Magnetics* 38.2 I (2002), pp. 901–904. ISSN: 00189464. DOI: 10.1109/20.996232.

[9] Kenneth H Carpenter and Senior Member. "A Differential Equation Approach to Minor Loops in the Jiles-Atherton Hvsteresis Model". In: 27.6 (1991), pp. 4404–4406.

[10] Vahid Hassani, Tegoeh Tjahjowidodo, and Thanh Nho Do. "A survey on hysteresis modeling, identification and control". In: *Mechanical Systems and Signal Processing* 49.1-2 (2014), pp. 209–233. ISSN: 10961216. DOI: 10.1016/j.ymssp.2014.04.012. URL: http://dx.doi.org/10.1016/j.ymssp.2014.04.012.

[11] Hoekwater William. "Hybrid Tunable Magnet Actuator: Design of a linearized forc-flux tunable magnet actuator". In: (2022).

[12] SAJ Hol. *Design and optimization of a magnetic gravity compensator*. 2004. 2004, p. 199. ISBN: 9038615639. DOI: 10.6100/IR574485. URL: http://www.narcis.nl/publication/RecordID/oai:library.tue.nl:574485.

[13] Shingo Ito, Francesco Cigarini, and Georg Schitter. "Flux-Controlled Hybrid Reluctance Actuator for High-Precision Scanning Motion". In: *IEEE Transactions on Industrial Electronics* 67.11 (2020), pp. 9593–9600. ISSN: 15579948. DOI: 10.1109/TIE.2019.2952829.

[14] Amália Iványi. "Hysteresis Models in Electromagnetic Computation". In: November (1997), p. 229. URL: http://books.google.com/books?id=pNXxPAAACAAJ&pgis=1.

[15] R.V. Iyer and X Tan. "Control of Hysteretic Systems Through Inverse Compensation". In: *IEEE Control Systems Magazine* February (2009), pp. 83–99.

[16] Thomas M. Jahns. "Flux-weakening regime operation of an interior permanent-magnet synchronous motor drive". In: *IEEE Transactions on Industry Applications* IA-23.4 (1987), pp. 681–689. ISSN: 19399367. DOI: 10.1109/TIA.1987.4504966.

[17] D C Jiles and D L Atherton. "Theory of Ferromagnetic Hysteresis". In: *Journal of Magnetism and Magnetic Materials* 61 (1986), pp. 48–60.

[18] D C Jiles and J B Thoelke. “Theory of ferromagnetic hysteresis: determination of model parameters from experimental hysteresis loops”. In: *IEEE Transactions on Magnetics* 25.5 (1989), pp. 3928–3930.

[19] A Knaian. “Electropermanent magnetic connectors and actuators : devices and their application in programmable matter”. In: (2010), p. 208. URL: http://dspace.mit.edu/handle/1721.1/60151.

[20] Stefan Kuiper et al. “Electromagnetic deformable mirror development at TNO”. In: *Advances in Optical and Mechanical Technologies for Telescopes and Instrumentation II*. Vol. 9912. SPIE, July 2016, p. 991204. ISBN: 9781510602038. DOI: 10.1117/12.2230891.

[21] Dieter Lederer et al. “On the Parameter Identification and Application of the Jiles-Atherton Hysteresis Model for Numerical Modelling of Measured Characteristics”. In: 35.3 (1999), pp. 1211–1214.

[22] J V Leite et al. “Real Coded Genetic Algorithm for Jiles – Atherton Model Parameters Identification”. In: July 2014 (2004). DOI: 10.1109/TMAG.2004.825319.

[23] Hengchuan Liu et al. “Permanent magnet remagnetizing physics of a variable flux memory motor”. In: *IEEE Transactions on Magnetics* 46.6 (2010), pp. 1679–1682. ISSN: 00189464. DOI: 10.1109/TMAG.2010.2044638.

[24] Erwin Madelung. *Über magnetisierung durch schnellverlaufende ströme und die wirkungsweise des rutherford-marconischen magnetdetektors*. JA Barth, 1905.

[25] Meijer Romano. “Tunable Magnets: Dynamic Flux-feedback Compensation Methods for Improved Magnetization State Tuning Performance and Minor-loop Magnetization State Tuning for the Validation and Reduction of the Break-even Tuning Interval”. In: February (2021).

[26] Miroslav Novak, Jakub Eichler, and Miloslav Kosek. “Difficulty in identification of Preisach hysteresis model weighting function using first order reversal curves method in soft magnetic materials”. In: *Applied Mathematics and Computation* 319 (2018), pp. 469–485. ISSN: 00963003. DOI: 10.1016/j.amc.2017.05.017.

[27] V. Ostovic. “Memory motors - A new class of controllable flux PM machines for a true wide speed operation”. In: *Conference Record - IAS Annual Meeting (IEEE Industry Applications Society)* 4.C (2001), pp. 2577–2584. ISSN: 01972618. DOI: 10.1109/ias.2001.955983.

[28] Andrea Paesano Jr et al. “Application of the modified Rayleigh model in the mathematical analysis of Alnico II minor loops”. In: 612.October 2020 (2021). DOI: 10.1016/j.physb.2020.412629.

[29] Franz Preisach. “Untersuchungen über den Barkhauseneffekt”. In: *Annalen der Physik* 395.6 (1929), pp. 737–799.

[30] Guangyuan Qiao et al. “Analysis of Magnetic Properties of AlNiCo and Magnetization State Estimation in Variable-Flux PMSMs”. In: *IEEE Transactions on Magnetics* 55.7 (2019), pp. 12–17. ISSN: 19410069. DOI: 10.1109/TMAG.2019.2898888.

[31] Sören Rosenbaum et al. “Use of Jiles – Atherton and Preisach Hysteresis Models for Inverse Feed-Forward Control”. In: *IEEE Transactions on Magnetics* 46.12 (2010), pp. 3984–3989.

[32] Michael Ruderman. “Computationally Efficient Formulation of Relay Operator for Preisach Hysteresis Modeling”. In: *IEEE Transactions on Magnetics* 51.12 (2015), pp. 51–54. ISSN: 00189464. DOI: 10.1109/TMAG.2015.2455517.

[33] A. E. M. Schmerbauch et al. “Influence functions for a hysteretic deformable mirror with a high-density 2D array of actuators”. In: *Applied Optics* 59.27 (2020), p. 8077. ISSN: 1559-128X. DOI: 10.1364/ao.397472. arXiv: 2005.07418.

[34] R Munnig Schmidt, Georg Schitter, and Adrian Rankers. *The design of high performance mechatronics-: high-Tech functionality by multidisciplinary system integration*. Ios Press, 2020.

[35] C Sima. “Minor loops modelling with a modified Jiles – Atherton model and comparison with the Preisach model”. In: 320 (2008), pp. 1034–1038. DOI: 10.1016/j.jmmm.2008.04.092.

[36] R.K. (TU Delft) Sinha. “Hysteresis Compensation in Piezo-Actuator”. In: *Thesis Topology* February (2016), pp. 5–7.

[37] Zsolt Szabó and János Füzi. “Implementation and identification of Preisach type hysteresis models with Everett Function in closed form”. In: *Journal of Magnetism and Magnetic Materials* 406 (2016), pp. 251–258. ISSN: 03048853. DOI: 10.1016/j.jmmm.2016.01.027. URL: http://dx.doi.org/10.1016/j.jmmm.2016.01.027.

[38] M. A. Vasquez-Beltran, B. Jayawardhana, and R. Peletier. “Recursive Algorithm for the Control of Output Remnant of Preisach Hysteresis Operator”. In: *IEEE Control Systems Letters* 5.3 (2021), pp. 1061–1066. ISSN: 24751456. DOI: 10.1109/LCSYS.2020.3009423.

[39] S.G. Viëtor. “Tunable Magnets: Modeling and Validation for Dynamic and Precision Applications”. In: *Thesis Topology* February (2018), pp. 5–7.

[40] N. H. Vrijsen, J. W. Jansen, and E. A. Lomonova. “Comparison of linear voice coil and reluctance actuators for high-precision applications”. In: *Proceedings of EPE-PEMC 2010 - 14th International Power Electronics and Motion Control Conference* October (2010). DOI: 10.1109/EPEPEMC.2010.5606572.

[41] Hui Yang et al. “Flux-regulatable characteristics analysis of a novel switched-flux surface-mounted PM memory machine”. In: *IEEE Transactions on Magnetics* 50.11 (2014). ISSN: 00189464. DOI: 10.1109/TMAG.2014.2323331.

[42] Hui Yang et al. “Investigation of field regulation mechanism of flux-reversal variable flux memory machine by an improved frolich hysteresis model”. In: *2020 8th International Conference on Power Electronics Systems and Applications: Future Mobility and Future Power Transfer, PESA 2020* (2020). DOI: 10.1109/PESA50370.2020.9343995.

[43] Chuang Yu et al. “A flux-mnemonic permanent magnet brushless motor for electric vehicles”. In: *Journal of Applied Physics* 103.7 (2008), pp. 1–4. ISSN: 00218979. DOI: 10.1063/1.2830553.

[44] Chuang Yu et al. “Hysteresis modeling in transient analysis of electric motors with AlNiCo magnets”. In: *IEEE Transactions on Magnetics* 51.3 (2015), pp. 14–17. ISSN: 00189464. DOI: 10.1109/TMAG.2014.2362615.

[45] R. Zeinali, D. C.J. Krop, and E. A. Lomonova. “Comparison of preisach and congruency-based static hysteresis models applied to non-oriented steels”. In: *IEEE Transactions on Magnetics* 56.1 (2020), pp. 1–4. ISSN: 19410069. DOI: 10.1109/TMAG.2019.2950812.

[46] Miaolei Zhou et al. “Modified KP Model for Hysteresis of Magnetic Shape Memory Alloy Actuator”. In: *IETE Technical Review* 32.1 (2015), pp. 29–36. ISSN: 0256-4602. DOI: 10.1080/02564602.2014.968642. URL: http://dx.doi.org/10.1080/02564602.2014.968642.

[47] Sergey E. Zirka et al. “Congruency-based hysteresis models for transient simulation”. In: *IEEE Transactions on Magnetics* 40.2 I (2004), pp. 390–399. ISSN: 00189464. DOI: 10.1109/TMAG.2004.824137.

A

Extended Literature Review on Hysteresis Modelling

As suggested in chapter 1, an new modelling approach is needed to further increase the efficiency of the TMA. In this section, different modelling approaches in literature are discussed. First a distinction between modelling approaches is made and some restrictions are made. Then models found in literature are discussed and compared on a set of criteria which are:

- Modelled Order
- Direct or indirect CP calculation
- Estimated accuracy
- Complexity

Finally a conclusion on the comparison is given showing a gap in the state of the art of hysteresis modelling.

A.1. Introduction

In the field of hysteresis modelling, there are a lot of different hysteresis models with different properties, in this section, these properties will be discussed and assumptions on the importance of these properties are made.

Physical and phenomenological models Models can be subdivided into physical and phenomenological models [5], where physical models try to model the physics behind the hysteresis and phenomenological models are focused on the phenomena observed in magnetic hysteresis such as loop closure, wiping out property and history dependence. Applying this to the model needed for the TMA, it is not necessary to limit ourselves to one of these approaches since both approaches can fulfill the criteria set.

History independent and history dependent In chapter 2, the history dependence of magnetic hysteresis is discussed. However, there are modelling approaches that do not take this phenomena into account and are known as history independent hysteresis models (HIHM). History dependent hysteresis models (HDHM) do take this property into account. Zirka et al., discusses the differences between the two approaches and the applicability to modelling transients in the hysteresis curve (e.g. minor loops and reversal curves) [47]. In a HIHM, any trajectory in the B-H plane is completely determined by the current reversal point [47]. According to Zirka, this property makes it that it is inaccurate in modelling minor loops and can therefor not be used to model transient behaviour inside the major loop. The main reason given for this is that minor loop closure is not guaranteed, which is an inherently history dependent phenomena [5]. The claim that such a model is not suited for our application can be supported by the criteria set. Since an operating point can be reached by a FORC or a SORC (or any

higher order reversal curve), it is important to distinguish between this since the corner point prediction of the next step greatly depends on this. Therefor HIHMs are not suited for our applications and won't be considered.

Rate independent and rate dependent Another distinction that can be made in hysteresis models is that of rate independent models and rate dependent models. As discussed in chapter 2, hysteresis is not a static process and the rate at which the applied field is changed can have impact on the hysteresis behaviour. Rate dependent models try to model this behaviour where rate independent models neglect this effect. For our purpose, mostly the rate dependence due to the production of eddy currents between domain walls is of interest, since the thermal relaxation happens at very large time scales [5]. Magnetic diffusion time τ_m is a useful parameter for predicting eddy current delay effects on transient magnetic fields [6]. The magnetic diffusion time measures how long it takes for the magnetization state to reach 63% of the final state uniformly throughout the magnet. Viëtor also identified this in his work, and proposed an equation to estimate this parameter for the magnet used [39]. A more generalized estimation of τ_m can be found in the work of Brauer and Mayergoyz [6]. Here the $B(H)$-curve is assumed as a step leading to a simplified equation for the magnetic diffusion time:

$$\tau_m = \frac{\sigma R^2 B_m}{4H_o} \tag{A.1}$$

Where σ is the magnet's conductivity, R the radius, B_m the saturation flux density and H_o the applied field. This relation is validated using FEA and shown to overestimate the diffusion time between 10% and 20%. It is therefor safe to use this equation to get an estimation on the magnetic diffusion time in the AlNiCo 5 magnet present in the TMA.

Figure A.1 shows the magnetic diffusion time for different coil currents. The operating range for the TMA is between 1 and 10 A. It shows that the magnetic diffusion time for this range ranges between 100 and 700 microseconds. This is significantly less than the minimum tuning times that can be achieved by the current setup [25], therefor, it is assumed we can limit our research to only rate-independent models.

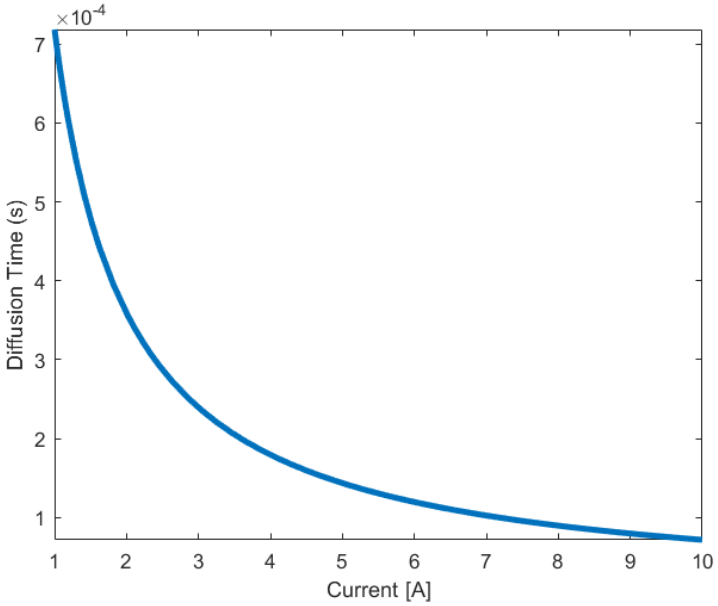

Figure A.1: Magnetic diffusion time of the AlNiCo magnet in the TMA setup for different coil currents

A.2. Literature review hysteresis modelling

In this section we will discuss the hysteresis models found in literature. Several well known general models are discussed and multiple models for certain applications.

General hysteresis models In general, the most used modelling approaches for magnetic hysteresis can be subdevided into the physical Jiles-Atherton (J-A) [17] model and the phenomenological operator based models such as the Preisach, Krasnosel'skii-Pokrovskii (KP) and Prandtl-Ishlinskii (PI) models [10]. First we will discuss the J-A approach, followed by the operator based approaches and their differences.

Jiles-Atherton models

First introduced by Jiles and Atherton in 1986, the J-A model tries to model magnetic hysteresis based on a physical approach [17]. The resulting model is a simple, differential equation based model with only 5 parameters to identify. A well-known drawback of the original model is that it is history-independent [35]. Carpenter proposed the first solution to this problem that does not require a priori knowledge of the next field reversal point [9]. Sima proposed a solution to allow for the modelling of closed minor loops by introducing history dependent parameters and compared it's accuracy to that of the Preisach model [35]. Since a history dependent hysteresis model is needed, Sima's approach to the J-A model will be considered from here onward.

Operator based models

Operator based models use a phenomenological approach to model hysteresis. In short, these models are based on a summation of an infinite amount of simple mathematical operators. The first operator based hysteresis model was proposed by Preisach and is based on the bi-stable relay operator [29]. The model is characterized by three important properties, the wiping out property, the congruency of minor loops and it being rate-independent [3]. It can be regarded as the basis of the development of other operator based hysteresis models. One of the most prevalent real-time applications of hysteresis models in literature, is inverse hysteresis compensation. Here, a hysteresis operator is identified and the inverse is used in the control scheme to cancel the hysteresis non-linearity of the plant [15]. In implementing the Preisach model for this purpose, two important disadvantages were observed. The Preisach model has a limited accuracy and due to the double integral, constructing the inverse of the model is not easy [10]. To improve the usability of the Preisach model, a modification was introduced called the Krasnosel'skii-Pokrovskii (KP) model. This model is similar to the Preisach model, only it uses a different operator, called the KP Kernel. This model has been implemented by Zhou to model magnetic shape memory allow actuators [46], and shows very good accuracy for the data it was identified on. However, due to the fact that still a double integral is used, difficulties still arise in constructing the inverse as well as in real-time applications [10]. To overcome this, the Prandtl-Ishlinskii (PI) model is introduced. The PI model is used a lot in inverse hysteresis control, since unlike the Preisach and KP models, it is analytically inversible [3]. Sinha summarized the advantages of the PI model over Preisach as that it is invertible, rate dependent and assymetric [36]. Since for our application, we are looking at a rate-independent and symmetric problem, where we don't need the inverse of the model, we can limit ourselves by not considering the PI model since its main advantages are not beneficial for our case.

Models in VFMMs As introduced earlier, the problem of hysteresis modelling for in-situ magnetization state tuning is something that is also found in Variable-Flux Memory Machines (VFMMs) [27]. Therefor, a review on the modelling approaches used in this field is given in this section. According to Yang, the existing numerical hysteresis models of AlNiCo magnets utilized in VFMMs are normally formulated by Preisach, piecewise linear and Frolich hysteresis models [41]. Besides that, a 3D hysteresis model and a nonlinear model are looked at [30] [23].

Piecewise Linear

Similar to what has been implemented by Viëtor and Meijer for the TMA [39],[25], linear models have been implemented in VFMMs as well. Yu implemented a Piecewise-linear hysteresis model based on the assumption that the major loop and all the minor loops have the same value of coercivity, but different values of remanence [44]. Cannas introduced a Piecewise-linear rate-dependent model based on a piecewise-linear circuit [8]. Due to the desire of a rate-independent model and no added benefits from the model proposed by Yu compared to the TMA linear model, we will only review the TMA linear model from here on forward.

Frölich

Yang introduced a hysteresis model based on the Frölich equations [41], and an improved version in later work [42]. The Frölich equations are based on the first empirical equation proposed for the representation of magnetization characteristics [14]. The entire major loop can be described by using a set of these equations. In Yang's work, the model can also represent minor loops and ascending and declining reversal curves.

3D Hysteresis

Qiao et at., introduces a model based on a 3D representation of the ascending and descending first order reversal curves of AlNiCo [30]. In this approach, FORCs are measured and distributed in 3D parameter space of (H, B, β) where β is a parameter introduced that is calculated from the reversal point of the FORC it represents. Every FORC therefor has constant β. This 3D surface is then identified using a Neural Network approach. However, other approaches are possible such as a simple 3D polynomial.

Nonlinear Liu Approach Liu introduced a model based on a higher order polynomial approach [23]. Here the major loops can be described using 5th order polynomials and any reversal curve can be described as a curve that follows the major loop and converges at saturation.

Others Other novel and interesting modelling approaches that were found during this literature review are discussed here. These are congruency based methods [47],[45] and a model based on Rayleigh equations [28].

Congruency based hysteresis models

The congruency property, is the property that the output of the model for a cyclic input is the same, independent on the initial remanent magnetization state [5]. This means that the initial magnetization state will merely results in a vertical shift of the minor loops created by the cyclic input. Prominent models such as the Preisach model show this property, however, magnetic hysteresis is inherently non H-congruent [45]. To solve this, congruency based hysteresis models have been introduced.

Zirka first introduced the First-order Congruency-based Model (FCM) in his work [47], Zeinali followed up this work by introducing the Second-order Congruency-based Model (SCM) [45]. The FCM is based on using measured FORCs to identify transplants for higher order reversal curves. These transplants are found by a series of numerical interpolations and a weighted sum over all possible transplants. The model can describe reversal curve of an infinite order and shows loop closure properties without H-congruency. The SCM includes the measurements of SORCs, such that transplants for TORCs and higher order reversal curves are taken directly from SORCs with the same reversal curve.

Rayleigh equations

Rayleigh equations are based on a power series approximation and can be used to model hysteresis loops [14]. Paesano used these equations to identify minor loops for different applied field magnitudes of an AlNiCo magnet [28], and showed good identification accuracy. However, since this approach only allows for the identification of symmetric minor loops and not of reversal curves, it is unsuited for TMA applications.

A.3. Model comparison

In this section, the models introduced are compared to see which fits best to the TMA application. Every model is reviewed on the previously defined criteria and at the end a summary is given visualizing the differences between the models. The criteria are: model order, reversal point calculation, identification, measurement and computational complexity and predicted accuracy.

Jiles-Atherton Since the model is a continuus description of the magnetization state, the model has an infinite order. Due to the nature of the modelling approach, which is the use of differential equations, the solution is gained by stepwise numerical integration, the stepsize of this integration is limited due to sensitivities to the input increment [31]. Thus, reversal point calculation is an iterative process. The identification process involves identifying 7 parameters based on the model proposed by Sima [35]. Multiple algorithms have been used to do so, such as: iterative [14],[18], based on simulated annealing [21] and genetic algorithms [22]. The data used for identification is of first order, meaning major loop and FORC data [35]. The computational complexity is low, due to the limited space and runtime complexity, it is therefor well suited for implementation on microcontrollers [31]. The accuracy of the model has been validated by Sima and shows decent understanding of minor loops with an average error of 2.4% [35].

Preisach and Krasnosel'skii-Pokrovskii Operator based models are continuous and thus have infinite order. It is not possible to directly calculate the reversal point from the desired operating point. The operator at the current operating point is known, but the operator at the desired operating point is not. The value for H_{CP} needs to be found, which can only be achieved via an iterative process. Such a recursive algorithm has been implemented by Vasquez-Beltran for remnant control of piezoelectric actuators [38], here around 18 iterations were needed for the control input to converge to the desired remanence. To identify the model, the weight function needs to be identified [37], Novak discusses the difficulties in this process involving non symmetry and negative weights in the weight function, both are non physical behaviour [26]. Zeinali argues that these problems can be solved by identifying on concentric loops, rather than reversal curves, however, this leads to an inaccurate model for reversal curves [45]. These difficulties increase the identification complexity of the model. Depending on the identification process used, the measurements needed are FORCs or symmetric minor loops. However, more data can be accquired as this increases model accuracy [10]. Computational complexity is high as a large amount of operators needs to be evaluated, this can be greatly reduced by implementing parallel computation such as FPGA [32]. The accuracy of these models ranges from moderate for Preisach [45],[35] to high for KP based modelling [46].

Frölich For the analyzis of Frölich based modelling, the paper of Yang is used [42]. The way this model is implemented by Yang, only FORCs are modelled, making this a first order model. Every FORC is determined by 2 parameters, which need to be found from the coordinates of the desired operating point, through a numerical iterative process. From here, the corner point can directly be calculated. The parameters need to be identified for every FORC, which can be done by a simple curve fitting algorithm. Measurements needed are major loop and symmetric minor loops. Since the resulting model is a discrete model, an interpolation algorithm is needed to continuously model all FORCs, increasing computational complexity. Besides that, computational effort is very low since the model is based on analytical equations. Accuracy is hard to estimate, but since the model is based on analytical equations, it is likely worse than that of empirical based models.

Linear The discussion on linear modelling is limited to the work performed by Viëtor and Meijer [39],[25]. The linear model implemented in the TMA only models a linearized approximation of ascending FORCs. From the desired operating point, it is directly possible to find the reversal point by solving a set of linear equations. To identify this model, only the empirical slope equation needs to be identified as done by Meijer. Measurement complexity is also low as only the first part of the FORCs is needed. Computational complexity is also low due to the linear equations. The accuracy of the model is shown to be good for the parts it has been identified for.

Nonlinear Liu Approach For nonlinear modelling approaches, we refer to the work of Liu [23]. The model can describe FORC and SORC behaviour, but it can be extended to model higher orders too. The reversal point can directly be calculated by solving a set of nonlinear equations. The identification process discussed by Liu only relies on the identification of the major loop as a 5th order polynomial. An extra identification step can be implemented where the non linear function $D(B)$ is identified. This would also increase measurement complexity as for this identification also minor loop data is required. Computational complexity is low since the model is a set of analytical equations that can directly be solved. The validation of the method shows an error of around 10% for different re-magnetization MMFs, which can be considered as poor accuracy.

3D Hysteresis Based on the work of Qiao, the 3D hysteresis model is reviewed [30]. The modelling approach only characterizes FORCs and is therefor first order. Due to the 3D Hysteresis surface, direct calculation of the reversal point is possible. When the coordinates on a FORC are known, the value of β can be found and the reversal curve can be found by solving for the intersection of the FORC and the major curve. The proposed identification procedure involving neural networks can be complex, however, simpler methods could be used as well. For the measurements, FORC data and major loop data is sufficient. The computational complexity can be considered low as well since computing the model is only evaluating a few equations. The work of Qiao shows very good understanding between measurements and modelled values.

First-order Congruency-based Model The FCM model discussed here is that of Zirka [47]. In this approach, FORCs are modelled directly from measurements and any higher order reversal curve is approximated from these measurements making the model order infinite. Calculating the reversal point becomes a complex process. When reversing onto a FORC, the reversal point can be found iteratively by finding a measured FORC and interpolating. Reversing onto a SORC or higher order reversal curve, requires a double iteration. The reversal point is found iteratively, and for every reversal point tested, a transplant that describes the SORC needs to be found iteratively. Since FORCs are directly taken from measurements, no identification is necessary. Measurement complexity is limited to FORC and major loop data. Computational complexity is high due to the double iterative solution. Finally, the accuracy of the model is high, but reduces with every higher order reversal curve.

Second-order Congruency-based Model For the SCM, the model proposed by Zeilani is considered [45]. Similarly to the FCM, the SCM is of infinite order. The reversal point when reversing onto FORCs or SORCs can be found using interpolation between measured reversal curves and higher order reversal curves need to be found using a double iteration similar to that of the FCM. Identification and computational complexity are comparable to that of the FCM, however, the measurement complexity is higher due to the required SORC measurements. The accuracy seems to be slightly better for higher order reversal curves.

A.3.1. Summary

To summarize the above review, the models are compared on the metrics which is shown in figure A.2. Here, green is the best, orange is worse and red is the worst. Also the ideal model is shown. Note that half a model order refers to the linearization of the reversal curves.

	Order	Reversal Point	Identification	Measurement	Computational	Accuracy
Ideal	1.5 order	Directly	Low	Moderate	Low	High
Non-Linear Liu Approach	Infinite	Directly	Low to moderate	Low to moderate	Low	Low
3D Identification	First order	Directly	Low	Moderate	Low	High up to first order
Linear	Half order	Directly	Low complexity	Moderate	Low	High for 0th order tuning, low for higher order tuning
Modified Jiles Atherton	Infinite	Iterative	Low	Moderate	Low	Moderate
Preisach	Infinite	Iterative	High	Moderate	High	Moderate to High
Frölich	First order	Iterative	Moderate	Moderate	Low	Low
First-order Congruency-based	Infinite	Double iterative	Low	Moderate	High	High for low order, moderate for high order
Second-order Congruency-based	Infinite	Double iterative	Low	High	High	High for low order, moderate for high order

Figure A.2: Comparison between models used in literature

A.3.2. Conclusion

As can be seen from the summary above, there is no modelling approach that perfectly fits the requirements set. The most promising modelling methods in terms of reversal point calculation and accuracy are the 3D identification and linear approach. However, both models separately don't model high enough order reversal curves to implement the improved tuning method. Combining both models with a congruency based regularity to linearize the SORCs as FORCs or by identifying SORCs directly could prove as the ideal solution to the application. This solution would model FORCs nonlinear and SORCs linear until the load line, it would directly calculate reversal points, with low identification effort, measurements including FORCs and possibly SORCs however this is rather avoided, with low computational complexity and high accuracy up until the linear part of SORCs. However, to really understand how such a modelling approach would work, a quantitative analysis on the hysteresis curve of AlNiCo needs to be performed through measured data.

B

Eddy Current Damping in Electro Magnetic Actuators.

Initial research into magnetic hysteresis and its properties in a magnetic actuator were investigated at the start of this thesis. Observations were made on dynamic effects due to eddy currents and will be discussed in this appendix.

B.1. Dynamic effects in non-laminated iron cores.

First, the setup developed in previous work [39],[25] was used to do initial investigation into magnetic hysteresis and to explore modelling options. The flexure mechanism was removed to fix the gap length to $l_g = 1000\mu m$. Furthermore, it is important to note that the steel cores used in this setup were not laminated, meaning that they are solid blocks of ST. 37 steel.

The first tests performed were to measure ascending FORCs over the entire magnetization range in the $B(H)$-curve. For this purpose negative voltage set-points were used to reach the CPs. The voltage was switched at 10Hz to give the current enough time to converge due to the inductance. One test was done where the voltage was switched from the negative set-point directly to +30V to saturate the magnet (Fig. B.1a), and one test where the voltage was first set to zero to let the magnetization state settle at the remanence before saturating (Fig. B.1b).

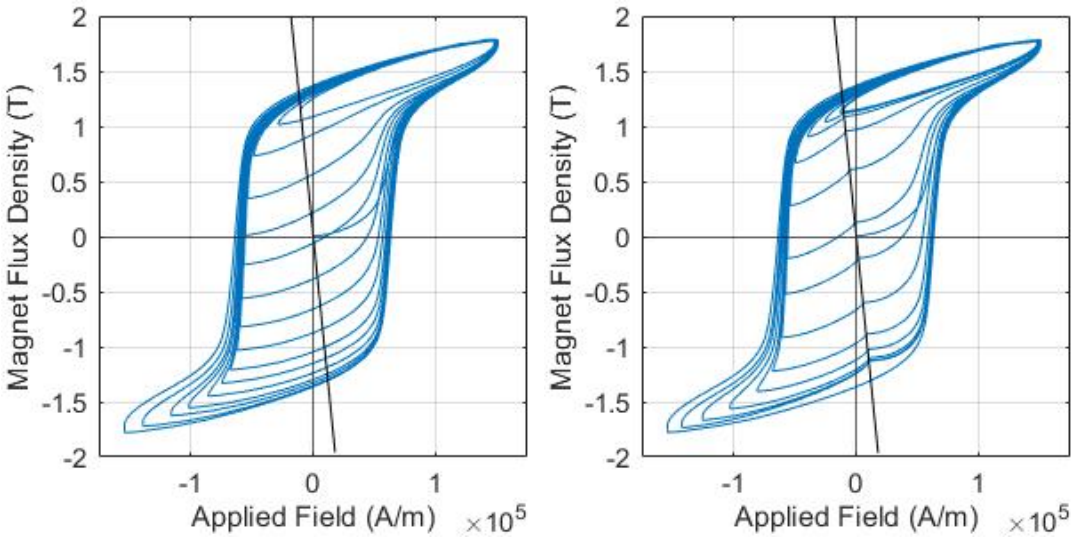

Figure B.1: (a): FORC measurement in non-laminated circuit directly switching from negative to saturation voltage. (b): FORC measurement with voltage set to zero before saturation.

From the results we can observe that there is very significant loop widening in the major loop due to the difference in voltage set-points to reach different CPs. This is observed by looking at the branches of the major loop from where the FORCs originate. The closer the CP is to negative saturation, the more loop widening is observed due to the faster rate of change in the applied field.

Another observation is made by looking at the difference around the load line in both figures. There is a significant difference between directly going to saturation or having a zero step in between. It shows that there is a settling of the magnetization state to a steady state. This can be explained by the eddy currents in the steel cores. The eddy currents are generated due to the flux flowing through the core, but in turn, the eddy currents also generate a magnetic flux, in opposite direction of the applied field. By setting the voltage to zero, these eddy currents will die out, resulting in a net higher flux density in the gaps, which is shown by the spike at the load line. When the voltage is set to +30V to saturate the magnet, the eddy currents return and the opposed field reduces the measured flux density again.

To reduce the effects of loop-widening, a new test is designed. Here, the voltage is switched from +30V to -30V and the pulse length is varied to reverse the applied field at different CPs. The current profile should be the same for every step as the same -30V set-point is used. When there is no difference in dI/dt there is no difference in dH/dt between the steps and no relative loop-widening should be observed. Similar to before, this test is preformed twice, once by directly going to saturation (Fig. B.2a) and once with a zero step in between (Fig. B.2b).

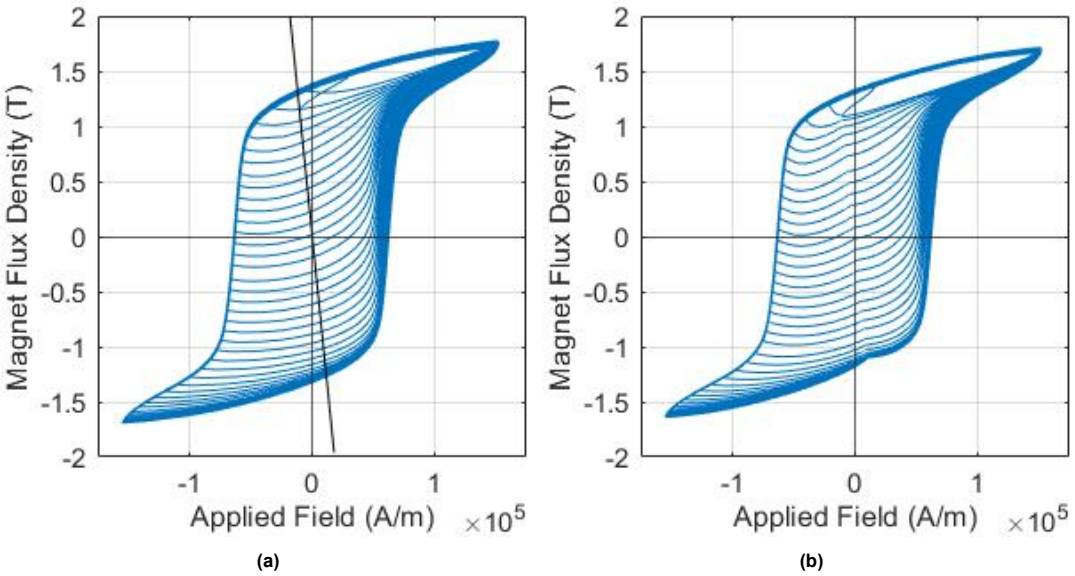

Figure B.2: (a): FORC measurement in non-laminated circuit, constant dI/dt, directly switching from negative to saturation voltage. (b): FORC measurement with voltage set to zero before saturation.

As expected, the loop-widening in the major loop has significantly decreased. However, the settling to the steady state is still observed. To investigate this further, one final test is performed on the non-laminated set-up. Here, the same CP is reached twice and the voltage is switched to +30V, once it is kept until saturation and once the voltage is set to zero when the current reaches zero. This is done to force the current to zero rather than letting it naturally decay. Eventually this is what is desired in the TMA as it is more efficient to force the current to zero, as your copper losses are less. It is expected that both responses are the same until the load line but that the magnetization state will still settle after the voltage is set to zero. This test is shown in Fig. B.3a with a zoomed in plot at the reached remanence in Fig. B.3b. As expected, the magnetization state settles to the remnant state after the voltage is set to zero.

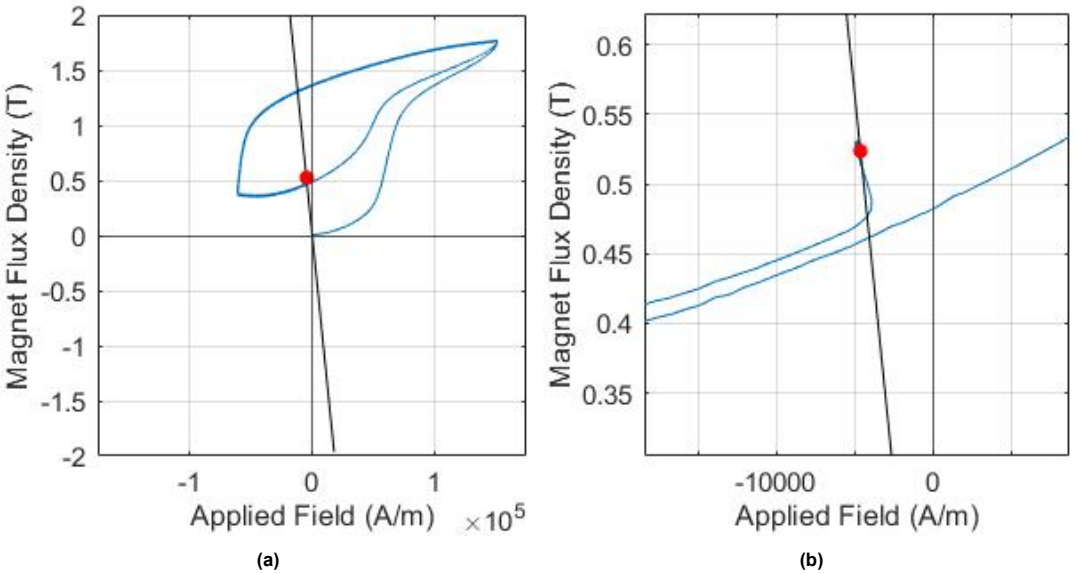

Figure B.3: (a): Settling of the magnetization state after forced decay to $I = 0$A (b): Zoomed in on the remanent sate.

From all the tests preformed on the non-laminated set-up, a few conclusions are made. Loop widening can be reduced by keeping the dI/dt profile the same for all tuning steps. However, in reality this is

hard to implement as you need a fast controller which can control the switching point of the voltage very accurately to not under- or overshoot the desired CP. Furthermore, the eddy currents introduce transients in the magnetization state that need to be taken into account during the modelling. If, for example, a model is identified on data without a zero step before saturation, significant errors in the remanent state will be observed between model and reality. Finally, all these dynamic effects will reduce the repeatability and quality of the measurement set-up. It is therefor desired to investigate how much this can be reduced by laminating the steel cores to reduce eddy currents and the effects.

B.2. Dynamic Effects in Laminated Cores

It is widely known that by laminating your electromagnetic circuit, eddy currents are greatly reduced. By electrically insulating the sheets from each other, no currents are flowing between the sheets. Since the sheets are much thinner than a solid block, the resistance is significantly increased and the potential difference is decreased, resulting in a net reduction of currents in the circuit. In this section, the dynamic effects observed in the previous section are investigated in a laminated circuit to see to what extend this is reduced. The circuit used it the one discussed in Appendix C. Here the cores are laminated out of 0.27mm thick electrical steel sheets. The insulation between sheets is achieved by a layer of epoxy glue which also binds the sheets together to form a solid core.

Figures B.4a and B.4b show the measurements for the same FORC test as performed in the previous section. Fig. B.4a shows the result where there is no zero step before saturation, where Fig. B.4b shows both the data with (red) and without a zero step (blue) to illustrate the differences.

First of all, almost no loop widening is observed anymore in the major loop. Also, the hysteresis curve resembles the shapes generally found in literature much better as the eddy current effects are reduced. Finally, there is almost no observable difference anymore between using a zero step or not before saturating the magnet again. It is clear to see that laminating the cores leads to a significant decrease in dynamic effects and a general increase in data quality.

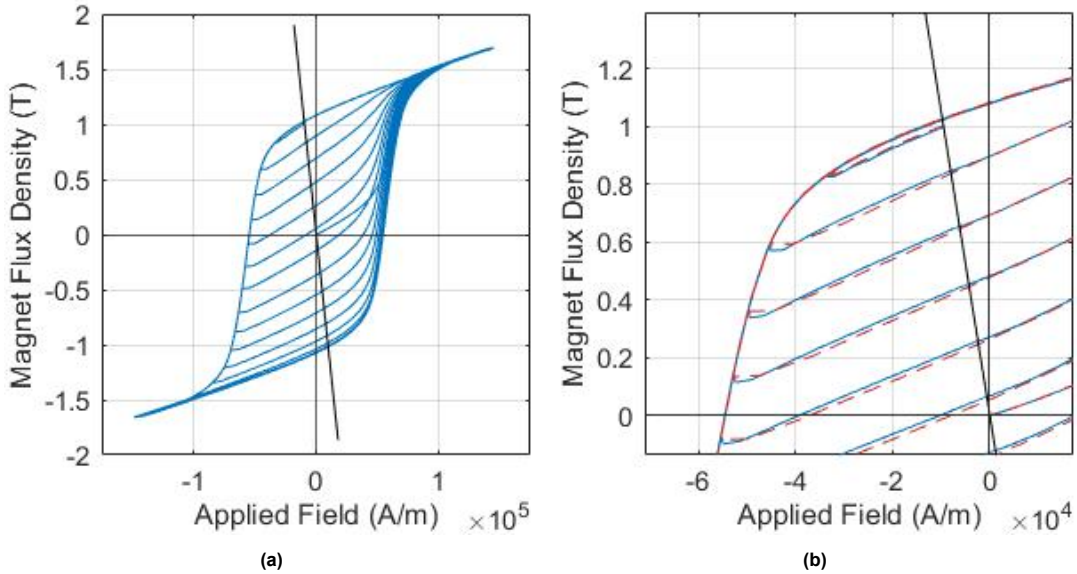

Figure B.4: (a): FORC measurement in laminated circuit, directly switching from negative to saturation voltage. (b): FORC measurement with zero step (red) and without zero step (blue).

As can be seen from Fig. B.4a, the reversal curves show linear behaviour in a large part of the $B(H)$-curve. To see how the linearity relates between different order curves, Figure B.5 is shown. Here, descending FORCs and descending SORCs are plotted together. It can be seen that the slopes of the different order reversal curves are similar. This observation is used in the development of the estimation algorithm proposed in chapter 3.

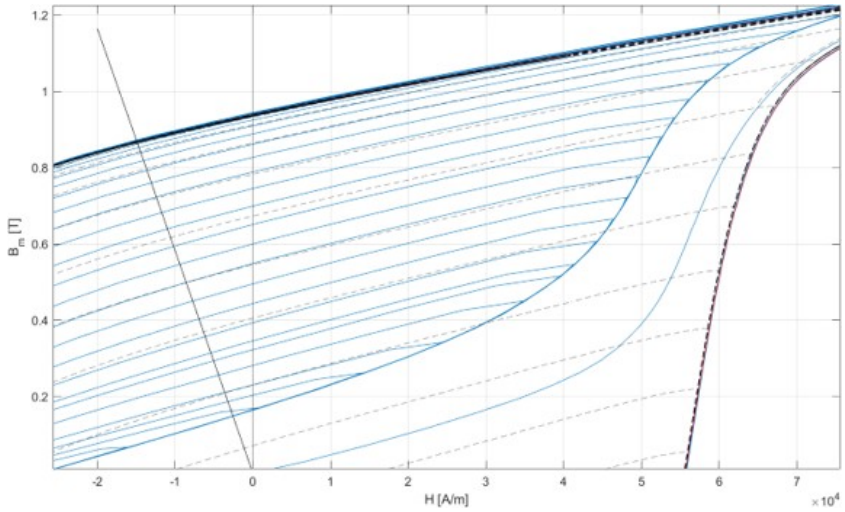

Figure B.5: Comparison between the slopes of the linear parts of descending FORCs (grey dashed) and descending SORCs (blue solid).

C

Experimental Setup

C.1. Experimental Hardware

In this section, the experimental hardware used during this thesis is discussed. First the actuator and its physical parameters are given, followed by the power electronics and their schematics. Finally sensors, their placements and their sensitivities are discussed.

C.1.1. Actuator Set-up

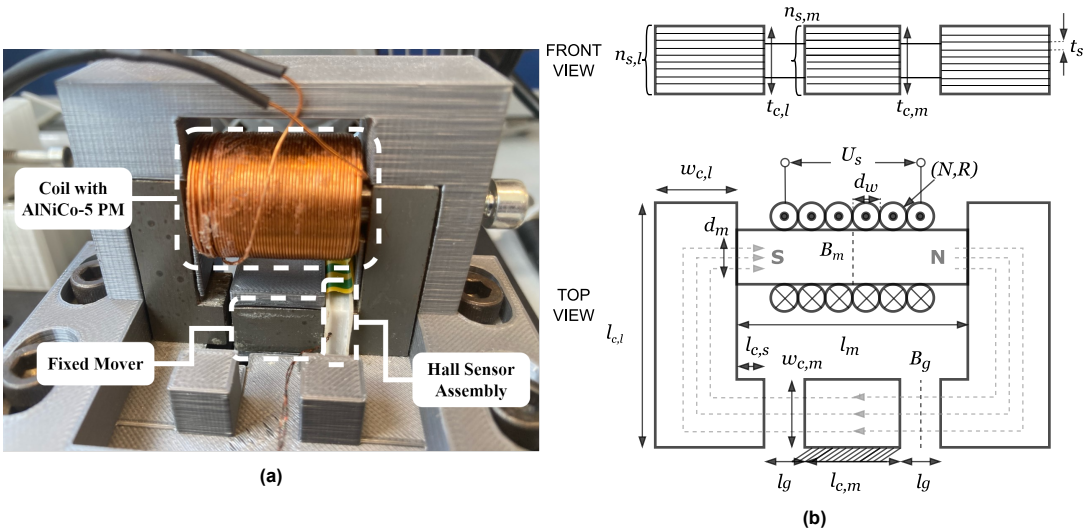

Figure C.1: (a): The realized experimental TMA. (b): Schematic of the TMA with dimensions.

Figures C.1a and C.1b show the realized TMA and its schematic respectively. Table C.1 contains all relevant system parameters. The housing which contains the actuator is 3D-printed PLA. In hindsight, this is not the ideal material as it is very flexible and can expand or contract due to changes in temperature and humidity. This makes the actuator less constant and there can be small differences in the measurements between certain days. The electrical steel components are laminated by hand using epoxy glue and some 3D-printed molds. Using an industrial lamination method could prove useful as thinner electrical steel can be used and more accurate manufacturing can be achieved, further reducing the eddy currents. The L-pieces are clamped in place by two bolts and the magnet. The mover is glued in a printed bracket and bolted to a mechanical breadboard. The L-pieces, magnet and 3D-printed housing are connected to a Thorlabs manual precision linear stage which allows for positioning of the mover with respect to the L-pieces.

Table C.1: Experimental Set-up Parameters

Symbol	Value	Unit	Description
Magnet Parameters (AlNiCo-5 (LNG44 Alcomax)			
l_m	30.15	[mm]	Magnet length
d_m	9.9	[mm]	Magnet diameter
$B_{r,sat}$	1.25	[T]	Saturated reanent flux density
H_c	55	[kA/m]	Coercive field strength
μ_{max}	270	[Tm/A]	Maximum relative permeability
Circuit Parameters			
$l_{c,l}$	34.85	[mm]	Length L-pieces
$w_{c,l}$	10.95	[mm]	Top width of L-pieces
$t_{c,l}$	9.90	[mm]	Tickness L-pieces
$n_{s,l}$	35	[-]	Number of electrical steel sheets in the L-pieces
$l_{c,s}$	14.85	[mm]	Length of hall sensor pole
$l_{c,m}$	17.4	[mm]	Length mover
$w_{c,m}$	12	[mm]	Width mover
$t_{c,m}$	10.9	[mm]	Tickness mover
$n_{s,m}$	39	[-]	Number of electric steel sheets in the mover
l_g	1.16	[mm]	Length air gap
A_g	100	[mm^2]	Area air gap
t_s	0.27	[mm]	Electrical steel sheet tickness
Coil Parameters			
N	655	[-]	Number of coil windings
R	3.75	[Ω]	Resistance coil
d_w	0.45	[mm]	Diameter coil wire
Other			
k	0.216	[-]	Experimentally tuned loss factor
U_{max}	\pm 30	[V]	Maximum voltage
I_{max}	10	[A]	Maximum current

C.1.2. Power Electronics

Two Delta Elektronica ES 030-10 30V/10A DC power supplies (Figure C.2a) are connected in parallel to supply the coil with $\pm$30V and 10A maximum. Due to the resistance of the coil, the supply is voltage limited and a maximum of 8A can be supplied, however, this is still enough to saturate the magnet (6.4A). A linear power amplifier (Figure C.2b, schematic can be found in Appendix E) is used to control the supply with the DAQ. The analog output pins of the DAQ have a $\pm$10V range and the amplifier has gain of 3. An additional 15V power supply (Figure C.2a, Delta Elektronica D1D) is used to power the signal conditioning board (Figure C.3b), current sensor (Figure C.3a) and hall sensor current source (Figure C.3c). The complete schematic of all the electronics is shown in Figure C.4.

(a) (b)

Figure C.2: (a): The two 30V supplies in parallel (right) and the $\pm$15V supply (left). (b): The linear power amplifier.

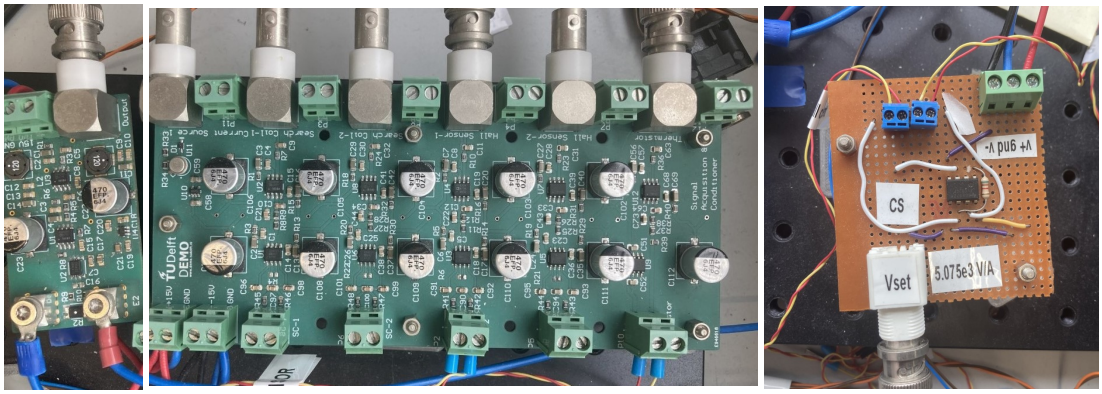

(a) (b) (c)

Figure C.3: (a): Current Sensor Board. (b): Signal Processing Board. (c): Hall Sensor Current Source.

C.1.3. Sensing

Two sensors are used to measure the state of the system, the custom designed current sensor (Figure C.3a, schematic in Appendix E) and an HE144 Hall Sensor (data sheet in Appendix E).

The current sensor board is supplied by the $\pm$15V power supply and the measured signal is send to the signal conditioning board (Figure C.3b, schematic in Appendix E). Here the signal is low-pass filtered at 3kHz. Sensor parameters are given in Table C.2.

The Hall sensor is supplied with a constant current from the Hall Sensor Current Source (Figure C.3c, schematic in Appendix E). The current source is fed by the $\pm$15V power supply and a 5.085V supply is needed to reach the correct current supply to the Hall sensor. The measured signal is amplified by the signal conditioning board and low-pass filtered at 3kHz. Other sensor parameters are given in Table C.2.

Table C.2: Sensor Parameters

Parameter	Value	Unit
Current Sensor		
Range	$\pm$10	[A]
Sensitivity	2	[AV^-1]
Resolution	$\sim$1	[mA]
Offset	5.018	[V]
LPF	3	[kHz]
Hall Sensor		
Range	$\pm$1.5	[T]
Sensitivity	5.1306	[TV^-1]
Resolution	$\sim$0.2	[mT]
Gain	23.85	[-]
LPF	3	[kHz]

The NI DAQmx USB module (NI 6351 USBX DAQmx) is used to supply the Linear Power Amplifier and the Hall Sensor Current Source. The processed sensor signals are connected to the analog input pins, as well as the supply voltage send to the Linear Power Amplifier (see Figure C.4).

C.2. Software

All experimental work has been done using the LabView software. To be able to use the scripts, NI LabView 2020 32 bit is recommended with the packages shown in Figure C.5.

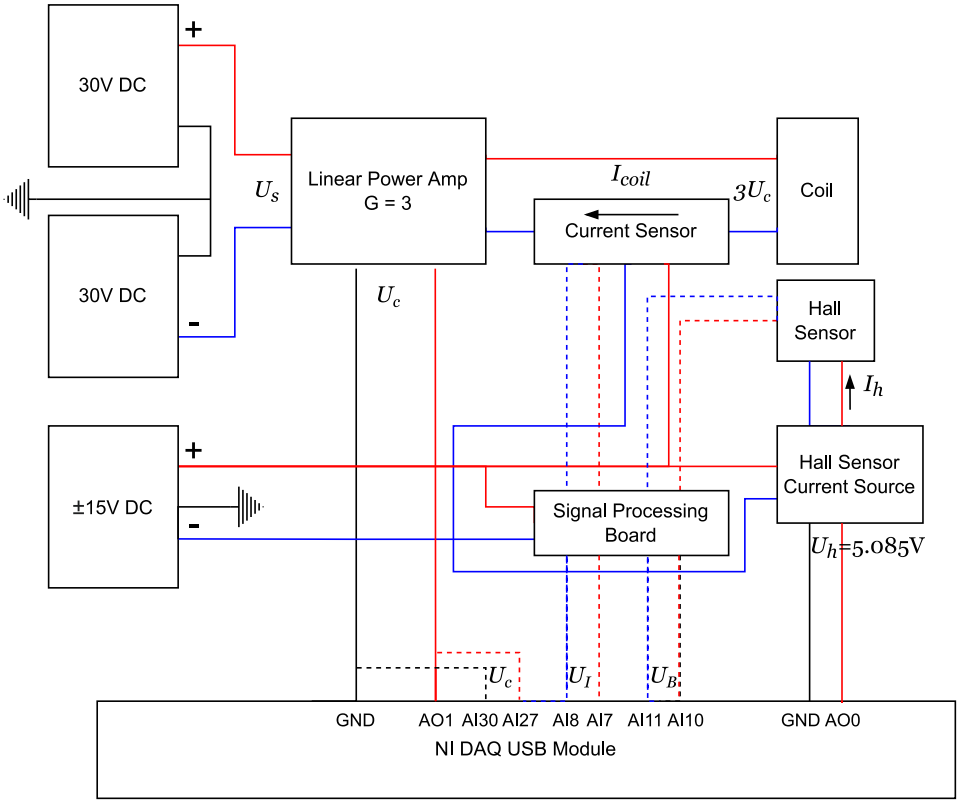

Figure C.4: Electronics Schematic: Here the solid lines are power supplies, dashed lines are sensor signals.

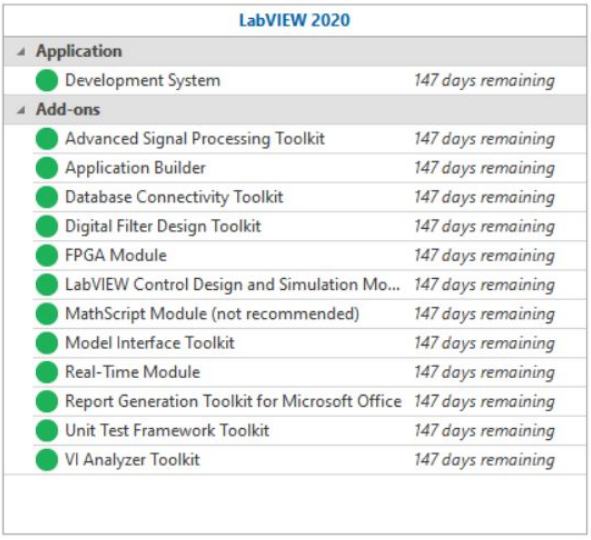

Figure C.5: Recommended LabView packages.

D

Hysteresis Model Identification and Algorithm Implementations

In this appendix, detailed information is given on how the contributions proposed in this thesis are implemented. First, the data acquisition for the models is discussed. Then the post processing needed is explained and the model identification is shown. Finally, the implementation of the different algorithms and the code needed is discussed. The processes will be shown for the FO and SO model as these are the models validated in this work. This appendix is mostly interesting for readers who plan to reproduce the work done in this thesis.

The entire process discussed here is done on the experimental setup discussed in Appendix C. It is important to note here that the measurements are quite sensitive to the state of the actuator. What is meant by this is that a slight change in shape can introduce changes in the B_m measurements in the order of 10 to 100 mT. For example if the mover is changed with respect to the cores or if the bolts clamping the magnet are loosened or tightened. This is due to the fact that fringe fluxes will change when the actuator is changed, but a constant loss factor is used in the post processing. The actuator is therefor kept as constant as possible during this entire process since this research focuses on modelling the magnet rather than the actuator. The loss factor is identified on the set-up by measuring the major loop and scaling it to a remanence of 1.25T.

D.1. Data Acquisition

When starting the data acquisition process, first a decision should be made on what order model is going to be identified and what the operating range of the actuator will be. In this work, FORCs and SORCs are measured to identify a FO and SO model. The reversal curves are measured over the entire domain of the $B(H)$-curve.

A current controller is used to accurately and repeatably reach the desired CPs. Current control removes any temperature dependencies in the measurements, as heating of the coil will change the resistance and therefor change the current for a specific voltage set-point. Besides this, current control makes sure that the current has converged to the set-point whereas voltage control does not due to the varying inductance.

To design the controller, the transfer function of an RL-circuit is used:

$$P(s) = \frac{I}{U} = \frac{1}{Ls + R} \tag{D.1}$$

A PI controller is designed by taking the inverse of (D.1) and making it proper. The controller is tuned to control the current without overshoot, with the transfer function of the following form:

$$C_I(s) = \frac{U}{I} = k_p(\frac{L_C s + R_C}{s}) \tag{D.2}$$

Here the parameters are tuned to the following values:

- $k_p = 40$
- $L_C = 70 * 10^{-3}$ H
- $R_C = 3.75\Omega$

To implement the controller in Labview, (D.2) is discretized to the z-domain using the 'tustin' method and a sampling time of 10 ms, leading to the following discrete transfer function:

$$C_I(z) = \frac{3.55z - 2.05}{z - 1} \tag{D.3}$$

Implementation of the controller together with the data acquisition in LabView is shown in Figure D.1. Here the red dot shows where current set-points enter the loop, areas A to D highlight different sections and the code will be explained by going through these:

Area A: Controller Logic The current controller should only be used to accurately reach the CP, during other steps no control is needed. The logic in this area makes sure this is the case. First it checks if the current set-point is larger or equal than 6.4A or smaller or equal than -6.4A which are the currents needed to saturate the magnet. If this is the case, the voltage is set to 30V or -30V respectively and no feedback control is active. If the current set-point is equal to 0A, the voltage is set to 0V and again no control is necessary. In any other case, the voltage is set to the output of the discretized controller in area B. The final voltage set-point is divided by 3 as there is a linear amplifier with a gain of 3 amplifying the DAQ signal. Finally, it is combined with the voltage supply of the hall sensor and fed into the analog output block.

Area B: Discretized Controller To implement the discretized controller, (D.3) needs to be rewritten explicitly for U_s as follows:

$$C_I(z) = \frac{U_s}{e_I} = \frac{3.55z - 2.05}{z - 1}$$

$$U_s z - U_s = 3.55 e_I z - 2.05 e_I$$

$$U_s - U_s z^{-1} = 3.55 e_I - 2.05 e_I z^{-1}$$

$$U_{s,i} = 3.55 e_{I,i} - 2.05 e_{I,i-1} + U_{s,i-1} \tag{D.4}$$

Here the subscripts i and $i-1$ denote current iteration value and previous iteration value respectively. U_s is the voltage set-point and e_I is the error between set-point and measurement. The Discretized Controller block in area B calculates U_s using (D.4) and sends it to the logic in Area A. The initial values of the inputs are set to zero as can be seen as inputs to the shift registers.

Area C: Data Acquisition Here the NI DAQmx assistant block is used to read the analog input pins of the DAQmx module. The DAQ receives inputs from the hall sensor, current sensor, temperature sensor and its own analog output. The sampling speed is set to 10kHz and the amount of samples to 100 samples. This means that the while loop will only iterate when 100 samples are read, resulting in a controller sampling frequency of 100Hz. It is important that this value corresponds to the sampling time used to discretize the controller. Every loop, the 100 measured samples are appended to the previously measured data which is logged in a .lvm file. The raw current data is processed to I_{coil} using the sensor sensitivity (Appendix C) and the last value is taken and fed back for the controller. The absolute value of I_{coil} is send to area D to check if the stopping criteria is met.

Area D: Stopping Criteria The logic in this area checks if any of the stopping criteria are met, which are:

1. Current has converged
2. Maximum loop iterations
3. Error occurs

For criteria 1, the absolute value of the measured current is compared to the absolute value of the current set-point. If this is lower or equal to 2 mA, the while loop finishes and the next current set-point is given. Note that this criteria is only active when the controller is active. For criteria 2, depending on the current set-point a maximum number of iterations is specified, which are:

- $I_{set} = 0$A: $i_{max} = 40$ $(0.4s)$
- $|I_{set}| \geq 6.4$A: $i_{max} = 3$ $(0.03s)$
- Else: $i_{max} = 50$ $(0.5s)$

Finally, for criteria 3, the loop is stopped if an error in the DAQmx module occurs.

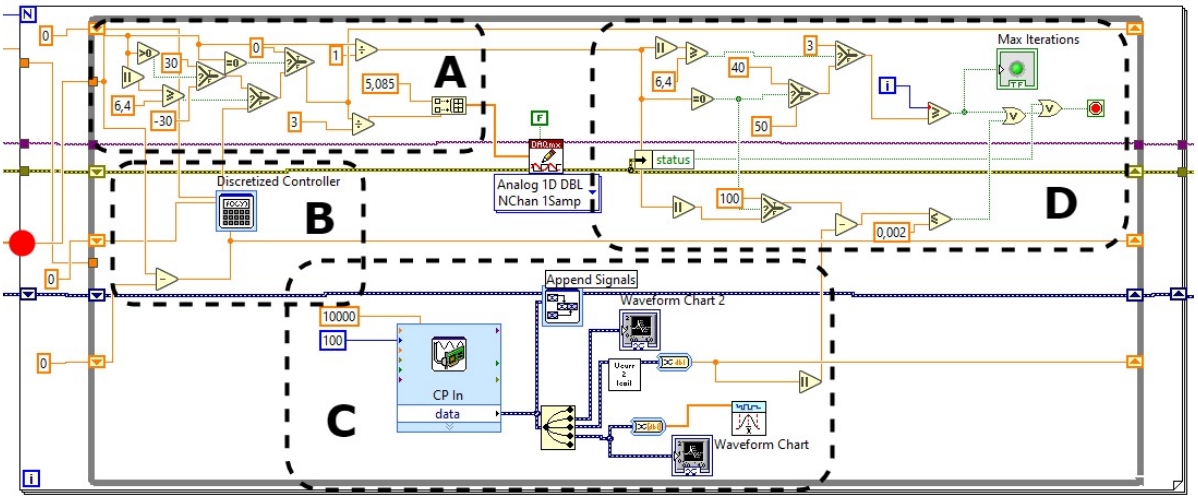

Figure D.1: Labview implementation, with the following sections highlighted: A) Controller Logic, B) Discrete Current Controller, C) Data Acquisition and D) Stopping Criteria Logic. Current set-points enter the loop at the red dot.

Using the LabView implementation the data for the FORCs and SORCs is gathered. Both ascending (Fig. D.2a) and descending FORCs (Fig. D.2b) are measured, where the CPs are determined by the following 1D array of current set-points:

$$\begin{aligned} I_{set} = \pm[&0.720, 1.200, 1.333, 1.467, 1.600, 1.733, 1.867, 2.000, 2.133, 2.200, 2.267, \\ &2.333, 2.400, 2.467, 2.533, 2.600, 2.667, 2.733, 2.800, 2.867, 2.933, 3.000, 3.067, 3.133, \\ &3.200, 3.267, 3.333, 3.467, 3.600, 3.733, 3.867, 4.000, 4.200, 4.800]\text{A} \end{aligned} \tag{D.5}$$

After reaching a CP, the next set-point is always 0A followed by ± 6.4A to saturate the magnet.

For every FORC measured, a set of SORCs is measured. Here, for every SORC the following current set-points are used:

$$I_{set} = [I_{FORC}, 0, I_{SORC}, 0, I_{FORC}, I_{\text{Sat}}]$$

where I_{FORC} is the current set-point of the FORC from which the SORCs originate and I_{SORC} is the current set-point of the SORC. Figure D.3 shows 3 sets of these measured SORCs as illustration.

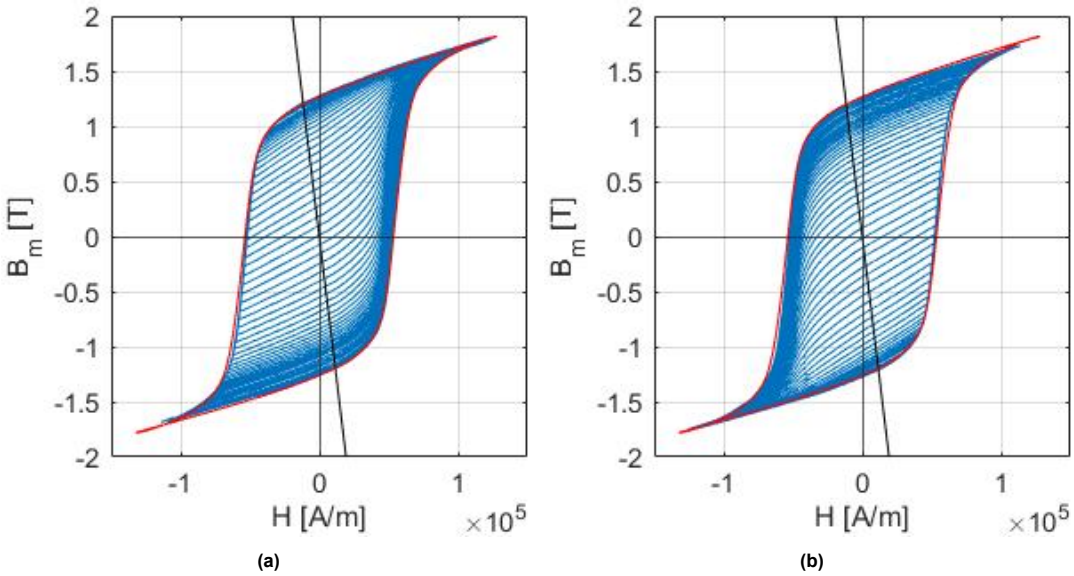

Figure D.2: (a): Measured Ascending FORCs (b): Measured Descending FORCs.

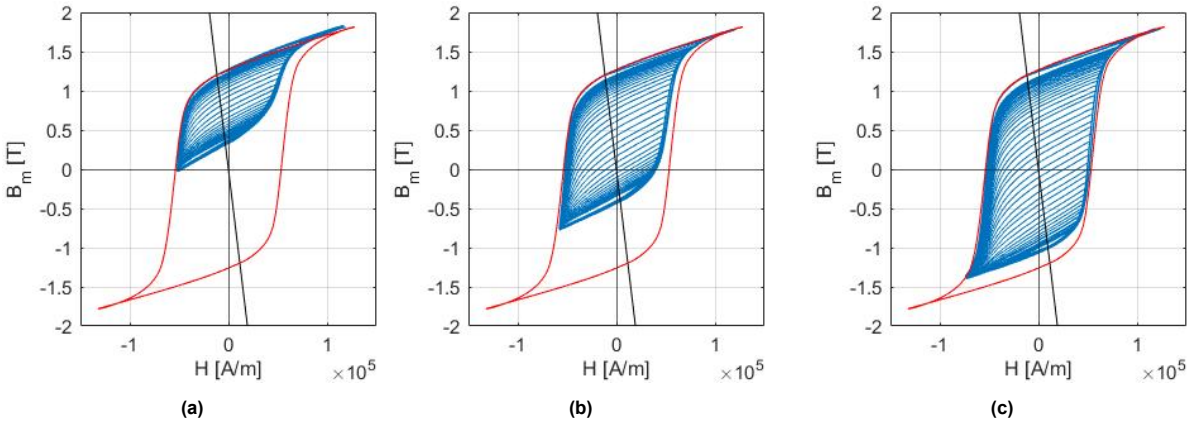

Figure D.3: (a): Measured Descending SORCs for $I_{FORC} = 2.4$A. (b): Measured Descending SORCs for $I_{FORC} = 3.0$A. (c): Measured Descending SORCs for $I_{FORC} = 4.0$A.

D.2. Post Processing

The data logged by the LabView script contains the raw voltage read-outs of the analog pins. These values need to be converted to the right values using the sensor sensitivities. Some search algorithms are then implemented to find the CPs and the corresponding remanences for each reversal curve. Finally, the intersections between the non-linear part of the reversal curves and the FORCs are found to use as CPs for the estimation model.

D.2.1. Data Conversion

The details of the experimental set-up are discussed in Appendix C, here the sensitivities of the sensors are given, which lead to the following conversion equations:

$$B_g = \frac{U_{hall}}{23.85} * 5.1306 - (-0.0532) \tag{D.6}$$

$$I_{coil} = \frac{U_{current} - 5.018}{0.5} \tag{D.7}$$

Since we are interested in modelling the magnetic flux density B_m, B_g needs to be converted using:

$$B_m = \frac{A_g B_g}{k A_m} \tag{D.8}$$

where A_g and A_m are the gap and magnet area as measured on the experimental setup (Appendix C) and k is the loss factor of the system. The value of k is experimentally tuned such that the converted major-loop has a remanence of 1.25T as is specified on the AlNiCo-5 data sheet (Appendix E). This has let to a value of $k = 0.216$.

Finally, we would like to know the applied magnetic field in the magnet H_m. By using the load line equation discussed in chapter 3, we can convert the current and flux measurement into applied field:

$$H_m = B_m \frac{2k A_m l_g}{-\mu_0 A_g l_m} + N_{coil} \frac{I_{coil}}{l_m} \tag{D.9}$$

Where the values of the actuator parameters are given in Appendix C. Since equations (D.8) and (D.9) are both used to convert from measurement to model data and from model data to control values, any systematic modelling errors are canceled, so they have no influence on the results presented in this thesis.

D.2.2. Find Corner Points and Remanences of Measured Data

Since the data acquisition program discussed in the previous section continuously records data, an algorithm is implemented to find the data for just the reversal curves, as this is what we are interested in. Figure D.4 illustrates how this algorithm is implemented by visualizing some converted data. Here the plots are the $B(H)$-curve, the voltage output of the DAQ, I_{coil} and B_m. The MATLAB code which performs the algorithm is given below.

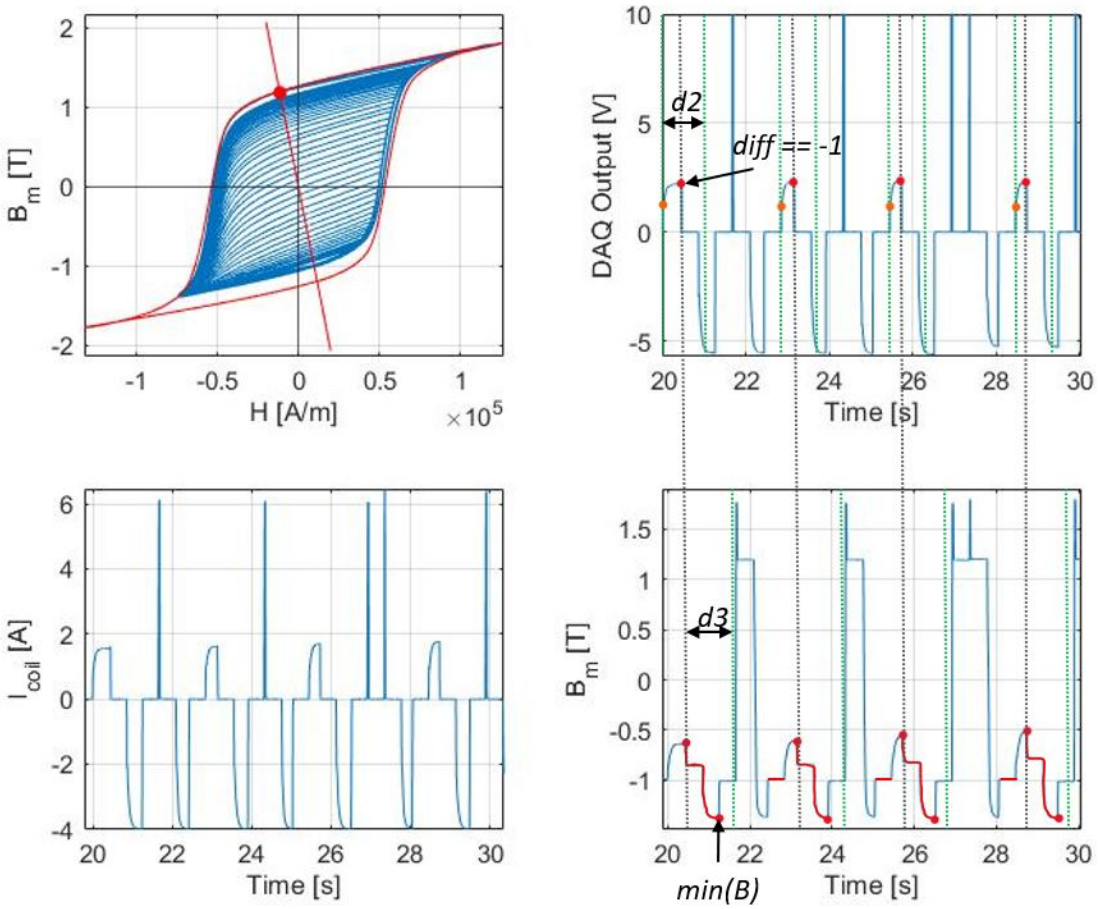

Figure D.4: Search algorithm on measurement data.

The working principles are described through the example of descending SORCs, but this can be used for ascending and descending reversal curves of any order. The goal of the algorithm is to find the time indexes which mark the start and end of the reversal curve data. The algorithm starts to search along the current data in steps of 1000 samples for regions where there are more than 140 samples between 0.5A and 5.5A (or -0.5 and -5.5 in case of ascending reversal curves). With this method, we find the increasing current pulses which are not saturation pulses, as these are shorter than 140 samples. We know that for descending reversal curves, the increasing current pulse is used to reach the CP, so we would like to find the first point where the input is switched from increasing to decreasing, as this will be the CP. So for this we define $\mathrm{dummy2}$, which is defined as the voltage output data from the point found on the positive current pulse to 10000 samples (1 second) further (*d2* if Fig. D.4). This data is converted to logical data with zeros for the samples which are zero (with a margin for noise) and 1 for samples larger than 0. By now taking the difference of this logical data, we expect to find zeros as long as the data is positive and find a single -1 value when the voltage is set to zero, followed by zeros again. By finding the index of the first -1 value in the difference, we find the index where the current is switched from increasing to decreasing and thus the index of the CP. Now we can look at the B_m data and define *dummy3* which starts at the CP and is 12000 samples long. By finding the index in this data where B_m is the minimum value, we find the end of the reversal curve.

Now that we've found the reversal curve data, we need to find the remanences of the SORC and FORC and log these. Since we used relatively long periods where the current is set to zero during the measurements, this is easily done by just taking the average of a small part of this steady-state data. For the settings used in this case it's identified that for the SORC remanence we can take the average of samples 500:600 after the CP and for the FORC remanence we can take 6000:5500 samples before

the CP. If the data is acquired with faster controllers and shorter wait times at zero, these values need to be changed. We can now continue the search algorithm from this point to find the next reversal curve and continue this for the entire data set. Then by performing this search on every SORC data set, we can log all the SORC CPs with their corresponding remanence and FORC remanence.

```
searchLength = 1000 ;
searchSteps = length(input_u)/searchLength ;

B_sat = 1.7 ;
B_minsat = -1.7 ;
i = 0 ;
j=0 ;



    while i <= searchSteps-10001/searchLength

        dummy1 = I_coil(searchLength*i+1:searchLength*i+searchLength) ;
        if direction == 1
             dummy1 = dummy1(dummy1 > -5.5) ;
             dummy1 = dummy1(dummy1 < -0.5) ;
        elseif direction == -1
             dummy1 = dummy1(dummy1 < 5.5) ;
             dummy1 = dummy1(dummy1 > 0.5) ;
        end


        if length(dummy1) > 140

            dummy2 = input_u(searchLength*i+1:searchLength*i+10001) ;
            if direction == 1
                dummy2 = dummy2 < 0 -0.03   ;
                dummy2 = diff(dummy2) ;
                startIndex = find(dummy2 == direction,1,'first') ;
            else
                dummy2 = dummy2 > 0 +0.03   ;
                dummy2 = diff(dummy2) ;
                startIndex = find(dummy2 == direction,1,'first') ;
            end

            if isempty(startIndex) == 0
                j = j+1 ;

                startIndex = startIndex + searchLength*i-5 ;

                dummy3 = B_m(startIndex:startIndex+12000) ;
                endIndex = find(dummy3 == min(dummy3) , 1, 'first')+startIndex +1 ;

                SORCB = B_m(startIndex:endIndex) ;
                SORCH = H_m(startIndex:endIndex) ;
                B_rem(j) = mean(SORCB(500:600)) ;
                H_rem(j) = mean(SORCH(500:600)) ;
                H_CP(j) = SORCH(1) ;
                B_CP(j) = SORCB(1) ;
                FORCRem(j,:) = [mean(H_m(startIndex-6000:startIndex-5500)), ...
                mean(B_m(startIndex-6000:startIndex-5500))] ;

                i = round(endIndex/searchLength,0) +1   ;

                NonLinSORC_H(j,:,m) = SORCH(length(SORCH)-5000:length(SORCH)) ;
                NonLinSORC_B(j,:,m) = SORCB(length(SORCB)-5000:length(SORCB)) ;

            else
                i = i+1 ;
            end

        else
            i = i+1 ;
        end
```

```
65      end
```

D.2.3. Find Intersections of FORC and Measured Data

For the estimation model proposed in chapter 3, we need to find the intersections between the highest measured order and the FORCs. In the case of the SO model, this is the intersection between the measured SORCs and the measured FORCs. The non-linear part of the SORC data is logged by taking the last 5000 values of the SORC data as can be seen in the code in the previous subsection. With the non-linear part, we mean from the remanent state to the FORC CP. Due to the stopping criteria in the data acquisition program we know that this will never be more than 5000 samples. Similarly, the linear part of the FORCs (from CP to remanent) are logged during the FORC post processing.

Due to loop widening, it can be the case that the non-linear part of the SORC, crosses the FORC past its CP, in this case, no intersection is found. A linear extrapolation is performed on the FORC data to solve this.

Using the MATLAB function InterX [2], we can find the intersections of the SORCs and FORCs and log them as the CPs with the code shown below. Here size(NonLinDescendingSORC_H,1) are the amount of SORCs per set, size(LinAscendingFORC_H_Ext,2) are the number of linear FORCs and size(NonLinDescendingSORC_H,3) are the amount of SORC sets. A moving average filter is used to smooth the SORC data, as the noise was increasing the number of intersections which greatly reduced the computational speed of this code. InterX returns all the intersections between L1 and L2 in an array. In theory, there should only be one or no intersections, however, it can happen that due to noise, multiple intersections are found. To handle this, some logic is used which logs NaN in the case of no intersections and takes the most negative intersection in the case of more than 1 (most positive if SORCs are ascending). This can be used due to the monotonically decreasing nature of the reversal curves. The CP coordinates are then logged in the 3-dimensional arrays as shown in the code. The corresponding remanences are those of the linear FORCs which are already logged during the FORC post processing. Figure D.5 shows two examples where the intersections are found between a set of descending SORCs and ascending FORCs.

```
1  for i = 1:size(NonLinDescendingSORC_H,1)
2      for j = 1:size(LinAscendingFORC_H_Ext,2)
3          for m = 1: size(NonLinDescendingSORC_H,3)
4              L1X(:) = NonLinDescendingSORC_H(i,:,m) ;
5              L1Y(:) = NonLinDescendingSORC_B(i,:,m) ;
6              L1X = smooth(L1X,20,'moving')' ;
7              L1Y = smooth(L1Y,20,'moving')' ;
8              L2X(:) = LinAscendingFORC_H_Ext(:,j)' ;
9              L2Y(:) = LinAscendingFORC_B_Ext(:,j)' ;
10             L1 = [L1X;L1Y] ;
11             L2 = [L2X;L2Y] ;
12
13             P = InterX(L1,L2) ;
14
15             if isempty(P) == 1
16                 IntL = [NaN ; NaN] ;
17             elseif size(P,2) == 1
18                 IntL = [P(1) ; P(2)] ;
19             else
20                 IntL = [min(P(1,:)) ; min(P(2,:))] ;
21             end
22
23             DescSORCEstCP_H(i,j,m) = IntL(1) ;
24             DescSORCEstCP_B(i,j,m) = IntL(2) ;
25         end
26
27     end
28 end
```

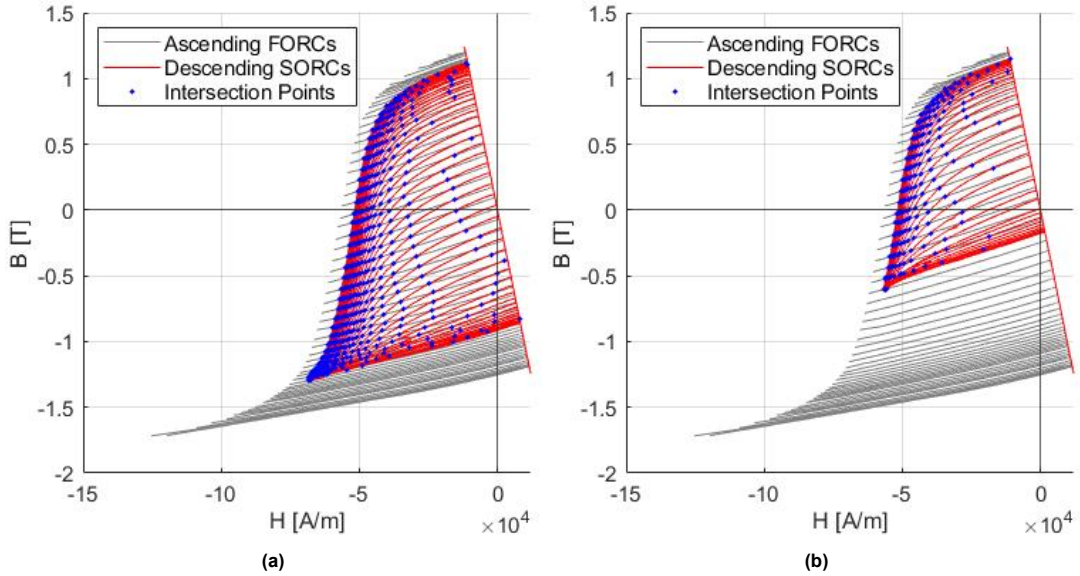

Figure D.5: Intersections between descending SORCs and ascending FORCs.

D.3. Model Identification

Using the logged CP coordinates and remanent values, model identification can be performed. To find the optimal polynomial order, the fit is performed on orders 1 to 50 and the average RMSE on test data is optimized. The MATLAB implementation for the SO model is shown in the code below. Here B2H3D and B2B3D are the CP coordinates logged with the remanences of the corresponding SORCs and FORCs. B2H3D(1,:,:) are the FORC remanences, B2H3D(2,:,:) are the SORC remanences and B2H3D(3,:,:) are the H-values of the CP, and the same for B2B3D. The function prepareSurfaceData converts the arrays from 3-dimensional to 2-dimensional such that is can be used by the function MultiPolyRegress [1]. MultiPolyRegress fits a multi-variable polynomial to B2H_y as a function of B2H_x with the specified order polyorder. B2H_PF and B2B_PF are the resulting polynomial functions for calculating H_{CP} and B_{CP} respectively.

To test the obtained polynomials, some test data is processed where TestFORCRem is a 1D array of size *n* with FORC remanences, TestSORCRem is a 2D array of size *nxm* with SORC remanences for every FORC, and TestCP_H and TestCP_B are the corresponding CP coordinates in *H* and *B* respectively. We calculate the CP coordinates for every SORC with the model and log them in CP_HModel and CP_BModel. Then by calculating the RMSE of the calculated coordinates with respect to the real coordinates we find RMSE_H and RMSE_B. Finally, to find the overall performance of the tested polynomial, we take the mean of the RMSEs and log this for every order. Figures D.6a and D.6b show the values of meanRMSE_H and meanRMSE_B for every order. From here we can observe over-fitting past the order of 25 for B2B_PF, so the optimal order is in this case set to 25.

```
for order = 1:50
    polyorder = order ;

    [B2H_x(:,1),B2H_x(:,2),B2H_y] = ...
        prepareSurfaceData(B2H3D(1,:,:),B2H3D(2,:,:),B2H3D(3,:,:)) ;

    B2H_fit = MultiPolyRegress(B2H_x,B2H_y,polyorder) ;
    B2H_PF = B2H_fit.PolynomialExpression ;


    [B2B_x(:,1),B2B_x(:,2),B2B_y] = ...
        prepareSurfaceData(B2B3D(1,:,:),B2B3D(2,:,:),B2B3D(3,:,:)) ;

    B2B_fit = MultiPolyRegress(B2B_x,B2B_y,polyorder) ;
    B2B_PF = B2B_fit.PolynomialExpression ;

```

```
15
16      clear CP_HModel
17      clear CP_BModel
18      clear RMSE_H
19      clear RMSE_B
20
21      for j = 1:length(TestFORCRem)
22          for i = 1:length(TestSORCRem(:,1))
23
24              CP_HModel(i,j) = B2H_PF(TestFORCRem(j),TestSORCRem(i,j)) ;
25              CP_BModel(i,j) = B2B_PF(TestFORCRem(j),TestSORCRem(i,j)) ;
26          end
27      end
28
29      for j = 1:length(TestFORCRem)
30          dummyy = CP_HModel(:,j) ;
31          y = dummyy(~isnan(dummyy)) ;
32          dummyyhat = TestCP_H(:,j);
33          yhat = dummyyhat(~isnan(dummyyhat)) ;
34          RMSE_H(j) = sqrt(mean((y-yhat).^2)) ;
35
36          dummyy = CP_BModel(:,j) ;
37          y = dummyy(~isnan(dummyy)) ;
38          dummyyhat = TestCP_B(:,j);
39          yhat = dummyyhat(~isnan(dummyyhat)) ;
40          RMSE_B(j) = sqrt(mean((y-yhat).^2)) ;
41      end
42
43      meanRMSE_H(order) = mean(RMSE_H) ;
44      meanRMSE_B(order) = mean(RMSE_B) ;
45
46  end
```

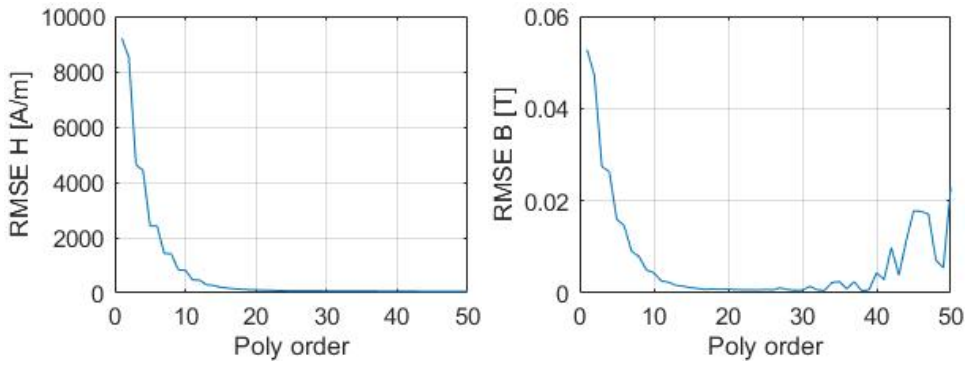

(a) (b)

Figure D.6: (a): RMSE in calculating H_{CP} for different polynomial orders. (b): RMSE in B_{CP}, over-fitting is observed past order 29.

D.4. Algorithm Implementation

The tuning algorithms discussed in chapter 3 are now implemented into LabView to validate the performance of both the algorithm as the hysteresis models identified.

D.4.1. LabView Implementation

The front panel of the validation script (Figure D.7) allows the user to select the tuning algorithm and the use-case. The use-case variables are the number of samples, the number of periods and the bounds. The algorithms implemented are: SMST, SMST-E, MMST, EMST-FO and EMST-SO. The use-cases are: FOTest, SOTest, Periodic, Decreasing Periodic and Random. The Test Number and Test Type control dictate the file names of the logged data.

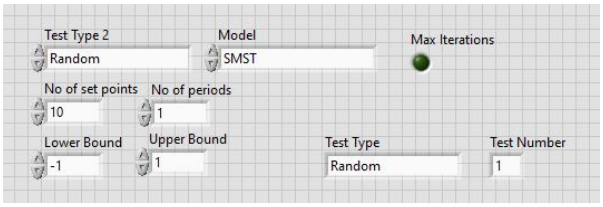

Figure D.7: LabView front panel controls.

The script uses the same control algorithm as has been used during the data acquisition in section D.1. However, since both a flux controller and current controller have been tested, modifications were needed to allow for this. The flux controller, as discussed in chapter 3 is discretized in the same manner as the current controller in section D.1:

$$U_{s,i} = 2.118e_{B,i} - 1.176e_{B,i-1} + U_{s,i-1} \tag{D.10}$$

The current or flux set-points, depending on the controller, are generated by the chosen tuning algorithm. The algorithms consist of two parts, a order tracking algorithm which is the same for every algorithm expect for the SMST-E, and the tuning algorithm itself (Figure D.8). It uses the Matlab implementation structures in LabView. The blue script is the order tracking algorithm which is directly implemented in LabView, where the grey script is the tuning algorithm script which uses the MathScript structure which calls on your Matlab files and runs externally.

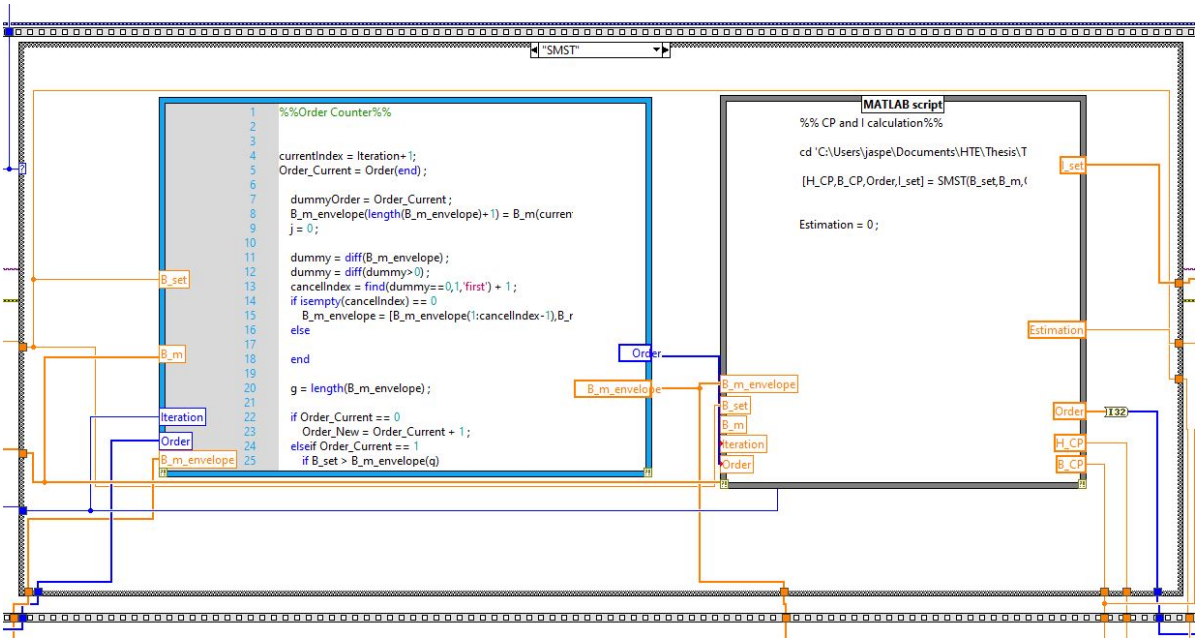

Figure D.8: Algorithm implementation in LabView.

D.4.2. Order Tracking Algorithm

For every algorithm except the SMST-E, the order tracking algorithm code shown below is used. The code takes the following inputs:

- B_{set}: The next desired MS.
- B_m: The previously reached magnetization states, taken from measurements.
- $Iteration$: The current iteration of the tuning process, one iteration is one MS
- $Order$: The orders of the previously reached magnetization states.

- $B_{m,envelope}$: The *History* states of the previously reached magnetization states.

The code produces the following outputs:

- $Order$: Extended with the order of the desired MS.
- $B_{m,envelope}$: Updated for the desired MS.

First B_m_envelope is extended with the latest reached magnetization state. Then a check is performed on how this state changes the *History* states. We know that only when the magnetization state is increased or decreased twice in row, the previous magnetization state should be removed from B_m_envelope. To check this, we take the diff of B_m_envelope resulting in positive and negative values representing increases or decreases in MS. By taking the diff of the logical array for where dummy is positive (so 0 if negative, 1 if positive) we expect 1's where the MS is alternating between increasing or decreasing and a 0 if it increases or decreases twice in row. By checking if there exists a 0 in the resulting array, we can find the index of the MS that should be removed which is then done.

Now the code continues to check where in the *History* B_{set} lies to find the order of the reversal curve. If the current order is either 0 or 1, this check is straight forward. As we always start tuning from the positive saturated remnant MS, the order is increased from 1 to 2 if B_{set} is larger than the last entry in B_m_envelope. If the current order is higher than 1, an iterative process is started which works as explained in chapter 3, where it is introduced as the EMST method. We define dummyOrder as a variable which starts as the current order and is reduced by 1 for every iteration where B_{set} does not lie in the previous two *History* states, defined as the *Envelope*. Finally, $Order$ is extended with the order of the reversal curve of B_{set}.

```
%%Order Counter%%

currentIndex = Iteration+1;
Order_Current = Order(end) ;

    dummyOrder = Order_Current ;
    B_m_envelope(length(B_m_envelope)+1) = B_m(currentIndex) ;
    j = 0 ;

    dummy = diff(B_m_envelope) ;
    dummy = diff(dummy>0) ;
    cancelIndex = find(dummy==0,1,'first') + 1 ;
    if isempty(cancelIndex) == 0
        B_m_envelope = [B_m_envelope(1:cancelIndex-1), ...
        B_m_envelope(cancelIndex+1:length(B_m_envelope))] ;
    else

    end

    g = length(B_m_envelope) ;

    if Order_Current == 0
        Order_New = Order_Current + 1 ;
    elseif Order_Current == 1
        if B_set > B_m_envelope(g)
            Order_New = Order_Current + 1 ;
        else
            Order_New = Order_Current ;
        end
    else
        while dummyOrder ≥ 1
            if dummyOrder == 1
                if B_set > B_m_envelope(g-j)
                    Order_New = dummyOrder + 1 ;
                    dummyOrder = 0 ;
                else
                    Order_New = dummyOrder ;
                    dummyOrder = 0 ;
                end
            elseif mod(dummyOrder,2) == 0
                if B_set < B_m_envelope(g-j) && B_set > B_m_envelope(g-j-1)
```

```
42                          Order_New = dummyOrder+1 ;
43                          dummyOrder = 0 ;
44                      else
45                          dummyOrder = dummyOrder - 1 ;
46                      end
47                  else
48                      if B_set > B_m_envelope(g-j) && B_set < B_m_envelope(g-j-1)
49                          Order_New = dummyOrder + 1 ;
50                          dummyOrder = 0 ;
51                      else
52                          dummyOrder = dummyOrder -1 ;
53                      end
54                  end
55                  j = j + 1 ;
56              end
57          end
58
59  Order(length(Order)+1)= Order_New;
```

The SMST-E has a different and simpler algorithm, as here it should be considered if the saturation step should go through positive or negative saturation. Here we define two values for $Order$ which are 1 and 2. If the order is 1, the CP lies on the descending major loop, if the order is 2, the CP should lie on the ascending major loop. If the current order is 1, there are three options:

1. B_{set} is lower than previous MS: order remains 1.
2. B_{set} is higher than previous MS and has greater absolute value: order remains 1 as positive saturation is more efficient.
3. B_{set} is higher than previous MS and has smaller absolute value: order goes to 2 as negative saturation is more efficient.

The same principles hold when the order is 2, only inverted.

```
1  %%Order Counter%%
2
3  currentIndex = Iteration+1;
4
5  Order(1) = 1 ;
6  Order_Current = Order(end) ;
7
8  if Order_Current == 1 && B_set<=B_m(currentIndex)
9          Order(length(Order)+1) = 1 ;
10 elseif Order_Current == 1 && B_set>=B_m(currentIndex)
11         if abs(B_set)<abs(B_m(currentIndex))
12             Order(length(Order)+1) = 2 ;
13         else
14             Order(length(Order)+1) = 1 ;
15         end
16 end
17
18 if Order_Current == 2 && B_set>=B_m(currentIndex)
19         Order(length(Order)+1) = 2 ;
20 elseif Order_Current == 2 && B_set<=B_m(currentIndex)
21         if abs(B_set)<abs(B_m(currentIndex))
22             Order(length(Order)+1) = 1 ;
23         else
24             Order(length(Order)+1) = 2 ;
25         end
26 end
```

D.4.3. Tuning Algorithms

The code that is implemented in the MathScript structure in LabView, sets the path of the function files and calls on the desired algorithm function in Matlab using the following code:

```
%% CP and I calculation%%

cd 'C:\PathToFunctions'

 [H_CP,B_CP,Order,I_set] = AlgorithmName(B_set,B_m,Order,Iteration)
```

The function for every tuning algorithm is shown in the next paragraphs. There is a lot of overlap between the functions, so only relevant differences are explained each time.

SMST The SMST algorithm starts by loading in the polynomial functions which are identified on the ascending FORC data. The SMST only operates on these reversal curves so these are the only ones needed. The script params.m contains all the system parameters as discussed in Appendix C which are needed to calculate the current set-points. The CP coordinates are then calculated for B_{set} which are used to calculate I_{set} using the load line equation. If a saturation step is needed, an extra current set-point of 6.4A is added to first saturate the magnet. In this case, the order is reset to 1.

```
function [H_CP,B_CP,Order,I_set] = SMST(B_set,B_m,Order,Iteration)

%% Load Polynomials %%

B2HAscFORC_PF = load('C:\PathToFunctions\B2HAscendingFORC.mat');
B2BAscFORC_PF = load('C:\PathToFunctions\B2BAscendingFORC.mat');
%% Model Calculations %%
currentIndex = Iteration+1;
tuneOrder = Order(end);
run params.m

if tuneOrder ==1
    B_CP = B2BAscFORC_PF(B_set);
    H_CP = B2HAscFORC_PF(B_set);
    I_set = l_m/N_coil*(H_CP-B_CP*(-2*k1*l_g*A_m/(mu_0*A_g*l_m)));
else
    B_CP = B2BAscFORC_PF(B_set);
    H_CP = B2HAscFORC_PF(B_set);

    I_set = l_m/N_coil*(H_CP-B_CP*(-2*k1*l_g*A_m/(mu_0*A_g*l_m)));

    I_set = [6.4, I_set];
    Order(length(Order)) = 1;
end
end
```

SMST-E The SMST-E uses both the polynomial functions identified on the ascending FORC data as on the descending FORC data. As explained in the previous sub-section, the order has a different meaning here than in other algorithms. By comparing the desired order with the previous order, the right polynomial is used to calculate the CP and a positive or negative saturation step is added to the current set-points.

```
function [H_CP,B_CP,Order,I_set] = SMSTE(B_set,B_m,Order,Iteration)

%% Load Polynomials %%

B2HAscFORC_PF = load('C:\PathToFunctions\B2HAscendingFORC.mat');
B2BAscFORC_PF = load('C:\PathToFunctions\B2BAscendingFORC.mat');
B2HDescFORC_PF = load('C:\PathToFunctions\B2HDescendingFORC.mat');
B2BDescFORC_PF = load('C:\PathToFunctions\B2BDescendingFORC.mat');
%% Model Calculations %%

currentIndex = Iteration+1;
tuneOrder = Order(end);
prevOrder = Order(length(Order)-1);
run params.m

```

```
if tuneOrder ==1 && tuneOrder == prevOrder && B_set ≤ B_m(currentIndex)
    B_CP = B2BAscFORC_PF(B_set) ;
    H_CP = B2HAscFORC_PF(B_set) ;
    I_set = l_m/N_coil*(H_CP-B_CP*(-2*k1*l_g*A_m/(mu_0*A_g*l_m))) ;
if tuneOrder ==1 && tuneOrder == prevOrder && B_set > B_m(currentIndex)
    B_CP = B2BAscFORC_PF(B_set) ;
    H_CP = B2HAscFORC_PF(B_set) ;
    I_set = l_m/N_coil*(H_CP-B_CP*(-2*k1*l_g*A_m/(mu_0*A_g*l_m))) ;
    I_set = [6.4, I_set] ;
elseif tuneOrder == 1 && tuneOrder≠prevOrder
    B_CP = B2BAscFORC_PF(B_set) ;
    H_CP = B2HAscFORC_PF(B_set) ;
    I_set = l_m/N_coil*(H_CP-B_CP*(-2*k1*l_g*A_m/(mu_0*A_g*l_m))) ;
    I_set = [6.4, I_set] ;
elseif tuneOrder == 2 && tuneOrder == prevOrder && B_set ≥ B_m(currentIndex)
    B_CP = B2BDescFORC_PF(B_set) ;
    H_CP = B2HDescFORC_PF(B_set) ;
    I_set = l_m/N_coil*(H_CP-B_CP*(-2*k1*l_g*A_m/(mu_0*A_g*l_m))) ;
elseif tuneOrder == 2 && tuneOrder == prevOrder && B_set < B_m(currentIndex)
    B_CP = B2BDescFORC_PF(B_set) ;
    H_CP = B2HDescFORC_PF(B_set) ;
    I_set = l_m/N_coil*(H_CP-B_CP*(-2*k1*l_g*A_m/(mu_0*A_g*l_m))) ;
    I_set = [-6.4, I_set] ;
else
    B_CP = B2BDescFORC_PF(B_set) ;
    H_CP = B2HDescFORC_PF(B_set) ;
    I_set = l_m/N_coil*(H_CP-B_CP*(-2*k1*l_g*A_m/(mu_0*A_g*l_m))) ;
    I_set = [-6.4, I_set] ;
end
end
```

MMST The MMST algorithm neglects any history dependency in the hysteresis curve and only checks if the desired order is even or uneven. For an even order, the descending FORCs are used and for a uneven order the ascending.

```
function [H_CP,B_CP,Order,I_set] = MMST(B_set,B_m,Order,Iteration)

%% Load Polynomials %%

B2HAscFORC_PF = load('C:\PathToFunctions\B2HAscendingFORC.mat') ;
B2BAscFORC_PF = load('C:\PathToFunctions\B2BAscendingFORC.mat') ;
B2HDescFORC_PF = load('C:\PathToFunctions\B2HDescendingFORC.mat') ;
B2BDescFORC_PF = load('C:\PathToFunctions\B2BDescendingFORC.mat') ;
%% Model Calculations %%

currentIndex = Iteration+1 ;
tuneOrder = Order(end) ;
run params.m

if mod(tuneOrder,2) == 0
    B_CP = B2BDescFORC_PF(B_set) ;
    H_CP = B2HDescFORC_PF(B_set) ;
else
    B_CP = B2BAscFORC_PF(B_set) ;
    H_CP = B2HAscFORC_PF(B_set) ;
end

I_set = l_m/N_coil*(H_CP-B_CP*(-2*k1*l_g*A_m/(mu_0*A_g*l_m))) ;
end
```

EMST-FO The EMST-FO is the first algorithm that incorporates the estimation models identified. Both the estimation models identified on the ascending FORC data as on the descending FORC data are used. If the tune order is 1, the same polynomial function as in the SMST is used. If the order is higher, it depends on if the order is even or uneven. For even order the estimation model identified on the ascending FORCs is used and for an uneven order to descending FORCs. Note that the estimation

models require two inputs, the desired magnetization state and the previous *History* magnetization states.

```
function [H_CP,B_CP,Order,I_set] = EMSTFO(B_set,B_m,B_m_envelope,Order,Iteration)

%% Load Polynomials %%

B2HAscFORC_PF = load('C:\PathToFunctions\B2HAscendingFORC.mat') ;
B2BAscFORC_PF = load('C:\PathToFunctions\B2BAscendingFORC.mat') ;
B2HAscFORCEst_PF = load('C:\PathToFunctions\B2HAscendingFORCEstimation.mat') ;
B2BAscFORCEst_PF = load('C:\PathToFunctions\B2BAscendingFORCEstimation.mat') ;
B2HDescFORCEst_PF = load('C:\PathToFunctions\B2HDescendingFORCEstimation.mat') ;
B2BDescFORCEst_PF = load('C:\PathToFunctions\B2BDescendingFORCEstimation.mat') ;
%% Model Calculations %%
currentIndex = Iteration+1 ;
tuneOrder = Order(end) ;
run params.m

if tuneOrder ==1
      B_CP = B2BAscFORC_PF(B_set) ;
      H_CP = B2HAscFORC_PF(B_set) ;
elseif mod(tuneOrder,2) == 0
      if B_m(currentIndex)-B_m(currentIndex-1)> 0
            B_set_prev = B_m_envelope(length(B_m_envelope)-1) ;
      else
            B_set_prev = B_m(currentIndex) ;
      end
    B_CP = B2BAscFORCEst_PF(B_set_prev,B_set) ;
    H_CP = B2HAscFORCEst_PF(B_set_prev,B_set) ;
else
      if B_m(currentIndex)-B_m(currentIndex-1)< 0
            B_set_prev = B_m_envelope(length(B_m_envelope)-1) ;
      else
            B_set_prev = B_m(currentIndex) ;
      end
    B_CP = B2BDescFORCEst_PF(B_set_prev,B_set) ;
    H_CP = B2HDescFORCEst_PF(B_set_prev,B_set) ;
end

I_set = l_m/N_coil*(H_CP-B_CP*(-2*k1*l_g*A_m/(mu_0*A_g*l_m))) ;

end
```

EMST-SO The EMST-SO works basically the same as the EMST-FO, with the major difference being that the estimation models are only used for orders higher than 2 and that they require 3 inputs which are the desired magnetization state and the previous two *History* magnetization states.

```
function [H_CP,B_CP,Order,I_set] = EMSTSO(B_set,B_m,B_m_envelope,Order,Iteration)

%% Load Polynomials %%
B2HAscFORC_PF = load('C:\PathToFunctions\B2HAscendingFORC.mat') ;
B2BAscFORC_PF = load('C:\PathToFunctions\B2BAscendingFORC.mat') ;
B2HDescSORC_PF = load('C:\PathToFunctions\B2HDescendingSORC.mat') ;
B2BDescSORC_PF = load('C:\PathToFunctions\B2BDescendingSORC.mat') ;
B2HDescSORCEst_PF = load('C:\PathToFunctions\B2HDescendingSORCEstimation.mat') ;
B2BDescSORCEst_PF = load('C:\PathToFunctions\B2BDescendingSORCEstimation.mat') ;
%% Model Calculations %%
currentIndex = Iteration+1 ;
tuneOrder = Order(end) ;
B_set_tune = B_set ;
B_set_prev = B_m(currentIndex) ;
run params.m

if tuneOrder ==1
      B_CP = B2BAscFORC_PF(B_set) ;
      H_CP = B2HAscFORC_PF(B_set) ;
```

```
20  elseif tuneOrder == 2
21      if B_m(currentIndex)-B_m(currentIndex-1)> 0
22              B_set_prev = B_m_envelope(length(B_m_envelope)-1) ;
23      else
24              B_set_prev = B_m(currentIndex) ;
25      end
26     B_CP = B2BDescSORC_PF(B_set_prev,B_set) ;
27     H_CP = B2HDescSORC_PF(B_set_prev,B_set) ;
28  elseif mod(tuneOrder,2) == 0
29      if  B_m(currentIndex)-B_m(currentIndex-1)> 0
30              B_set_prev = B_m_envelope(length(B_m_envelope)-1) ;
31      else
32              B_set_prev = B_m(currentIndex);
33      end
34     B_CP = B2BDescSORC_PF(B_set_prev,B_set) ;
35     H_CP = B2HDescSORC_PF(B_set_prev,B_set) ;
36  else
37      if B_m(currentIndex)-B_m(currentIndex-1)< 0
38              B_set_prev = B_m_envelope(length(B_m_envelope)-1) ;
39              B_set_prev2 = B_m_envelope(length(B_m_envelope)-2) ;
40      else
41              B_set_prev = B_m(currentIndex);
42              B_set_prev2 = B_m_envelope(length(B_m_envelope)-1) ;
43      end
44     B_CP = B2BDescSORCEst_PF(B_set_prev2,B_set_prev,B_set) ;
45     H_CP = B2HDescSORCEst_PF(B_set_prev2,B_set_prev,B_set) ;
46  end
47
48  I_set = l_m/N_coil*(H_CP-B_CP*(-2*k1*l_g*A_m/(mu_0*A_g*l_m))) ;
49
50  end
```

E

Data Sheets and Schematics

Technical Data Sheet - Alnico Magnets

Alnico Magnets

Alnico magnets have the best temperature coefficients of any magnet material.
Alnico magnets should be regarded as the best choice in extremely high temperature applications.
Alnico magnets can be produced by Casting or Sintering. Alnico is also rarely made by Bonding within a binder.
Cast Alnico is the most common form of Alnico magnet. Casting is often used to get "near net shape" Alnico magnets.
Casting Alnico is cost effective for both low and high volume, for small and very large magnets.
Sintered Alnico is cost effective for medium to high volume runs due to tooling cost. The parts are generally small to medium.
Sintered Alnico magnets are not so commonly used due to lower magnetic performance and limitation to simpler shapes.
Anisotropic magnets have the direction of magnetisation (DoM) permanently within the structure and give the maximum performance.
Isotropic magnets can be magnetised in many ways as they have no preferred direction of magnetisation but give reduced performance.
Cast Alnico 5 is the most common grade of Alnico, with the LNG44 variant of Alnico 5 (Alcomax 3) being the most popular.
Alnico5, Alnico 8 and Alnico 9 all exist with several sub-grades with differing performance characteristics.
Where the shape is new, tooling charges may apply. It is common for the magnet pole faces to be machined to finish.
Alnico produced to specific Br, Hc, Hci and BHmax may be possible but at extra cost. Keeping within normal grades is advised.
Custom or bespoke magnet shapes may carry an additional tooling cost and even a minimum order charge.
Alnico Assemblies are also possible.

Anisotropic Cast Alnico

Typical Range of Values

Material	Br		Hc (Hcb)		Hci (Hcj)		BHmax	
	T	kG	kA/m	kOe	kA/m	kOe	kJ/m^3	MGOe
Alnico 5 (Alnico5_LNG34)	1.10	11.0	50	0.63	52	0.65	34	4.25
Alnico 5 (Alnico5_LNG37)	1.18	11.8	50	0.61	51	0.64	37	4.63
Alnico 5 (Alnico5_LNG40)	1.20	12.0	50	0.63	52	0.65	40	5.00
Alnico 5 (Alnico5_LNG44)	1.25	12.5	50	0.65	54	0.68	44	5.50
Alnico 6 (Alnico6_LNG28)	1.15	11.5	58	0.73	60	0.75	28	3.50
Alnico 5DG (Alnico5DG_LNG52)	1.30	13.0	56	0.70	58	0.73	52	6.50
Alnico 5-7 (Alnico5-7_LNG60)	1.35	13.5	58	0.73	60	0.75	60	7.50
Alnico 8 (Alnico8_LNGT38)	0.80	8.0	110	1.38	112	1.4	38	4.75
Alnico 8 (Alnico8_LNGT40)	0.85	8.5	115	1.44	117	1.46	40	5.00
Alnico 8 (Alnico8_LNGT44)	0.90	9.0	115	1.44	117	1.46	44	5.50
Alnico 8HC (Alnico8HC_LNGT36J)	0.72	7.2	150	1.88	152	1.90	36	4.50
Alnico 9 (Alnico9_LNGT60)	1.00	10.0	110	1.38	112	1.4	60	7.50
Alnico 9 (Alnico9_LNGT72)	1.05	10.5	115	1.44	117	1.46	72	9.00
Alnico 9 (Alnico9_LNGT80)	1.08	10.8	120	1.50	122	1.53	80	10.00

Alnico 5 (LNG44) = Alcomax 3 = Alnico 500 = LNG44
Alnico 6 (LNG28) = Alcomax 4 = Alnico 400 = LNG28
Alnico 5DG (LNG52) = Alcomax 3SC = Alnico 600 = LNG52
Alnico 5-7 (LNG60) = Columax = Alnico 700 = LNG60
Alnico 8 (LNGT44) = Hycomax 3 = Alnico 8HE = LNGT44
Alnico 8 (LNGT40) = Hycomax 2 = Alnico 8H = LNGT40
Alnico 8 (LNGT38) = Alnico 8B = LNGT38
Alnico 8HC (LNGT36J) = Alnico 8HC = LNGT36J

Anisotropic Sintered Alnico

Typical Range of Values

Material	Br		Hc (Hcb)		Hci (Hcj)		BHmax	
	T	kG	kA/m	kOe	kA/m	kOe	kJ/m^3	MGOe
Alnico 5 (Alnico5_FLNG34)	1.15	11.5	48	0.60	50	0.63	34	4.25
Alnico 6 (Alnico6_FLNG28)	1.10	11.0	58	0.73	60	0.75	28	3.50
Alnico 8HC (Alnico8HC_FLNG36J)	0.72	7.2	150	1.88	152	1.90	36	4.50
Alnico 8 (Alnico8_FLNGT38)	0.80	8.0	110	1.38	112	1.40	38	4.75
Alnico 8 (Alnico8_FLNGT44)	0.85	8.5	120	1.50	122	1.53	44	5.50
Alnico 8 (Alnico8_FLNGT48)	0.92	9.2	125	1.56	127	1.59	48	5.50

Isotropic Cast Alnico

Typical Range of Values

Material	Br		Hc (Hcb)		Hci (Hcj)		BHmax	
	T	kG	kA/m	kOe	kA/m	kOe	kJ/m^3	MGOe
Alnico 3 (Alnico3_LN10)	0.65	6.5	38	0.48	40	0.50	10	1.25
Alnico 2 (Alnico2_LNG12)	0.75	7.5	45	0.56	46	0.58	12	1.50
Alnico 8 (Alnico8_LNG18)	0.55	5.5	90	1.13	97	1.21	18	2.25

Isotropic Sintered Alnico

Typical Range of Values

Material	Br		Hc (Hcb)		Hci (Hcj)		BHmax	
	T	kG	kA/m	kOe	kA/m	kOe	kJ/m^3	MGOe
Alnico 3 (Alnico3_FLN10)	0.65	6.5	40	0.50	42	0.53	10	1.25
Alnico 2 (Alnico2_FLNG12)	0.75	7.5	45	0.56	46	0.58	12	1.50
Alnico 8 (Alnico8_FLNGT18)	0.60	6.0	95	1.19	98	1.23	18	2.25
Alnico 8 (Alnico8_FLNGT20)	0.62	6.2	100	1.25	105	1.31	20	2.50

Bonded Alnico

Typical Range of Values

Material	Br		Hc (Hcb)		Hci (Hcj)		BHmax	
	T	kG	kA/m	kOe	kA/m	kOe	kJ/m^3	MGOe
Alnico_BLN7	0.31	3.1	79	1.00	103	0.85	6.77	0.86
Alnico_BLN8	0.34	3.4	83	1.05	107	1.00	7.96	1.00

Physical Characteristics (Typical)

Characteristic	Symbol	Unit	Value
Density	D	g/cc	6.9-7.3
Vickers Hardness	Hv	D.P.N	520-700
Curie Temperature	Tc	°C	800
Compression Strength	C.S	N/mm^2	300-400
Coefficient of Thermal Expansion	C//	10^{-6}/°C	11.5-13
	C⊥	10^{-6}/°C	11.5-13
Electrical Resistivity	ρ	μ Ω.cm	45-70
Tensile Strength	σ_{UTS} or S_U	x10^6 Pa	20-450 (37 LNG44)
Hardness		Rockwell	45-55
Curie Temperature	Tc	°C	810-860

Max Working Temperature
(Please note - your application will affect the performance available)

Material	Maximum recommended temperature
Alnico 2	450 degrees C
Alnico 3	450 degrees C
Alnico 5	525 degrees C
Alnico 6	525 degrees C
Alnico 5DG	525 degrees C
Alnico 5-7	525 degrees C
Alnico 8	550 degrees C
Alnico 8HC	550 degrees C
Alnico 9	550 degrees C
Bonded Alnico	150-200 degrees C (binder limiting)

Corrosion Resistance

Alnico is regarded as having very good to excellent corrosion resistance for most applications.
Because iron exists within the Alnico alloy, corrosion may be seen during prolonged exposure to water.
Alnico can be coated or painted (e.g. Red Paint) but this is often only for aesthetic purposes.

Temperature coefficients

Rev.Temp.Coef. of Induction (Br), α, %/°C	Rev.Temp.Coef. of Intrinsic Coercivity (Hci), β, %/°C
-0.03 (Alnico 2, Cast)	-0.02 (Alnico 2, Cast)
-0.035 (Alnico 2, Sintered)	-0.025 (Alnico 2, Sintered)
-0.035 (Alnico 3, Cast)	-0.025 (Alnico 3, Cast)
-0.03 (Alnico 3, Sintered)	-0.02 (Alnico 3, Sintered)
-0.02 (Alnico 5, Cast and Sintered)	+0.01 (Alnico 5, Cast and Sintered)
-0.02 (Alnico 6, Cast and Sintered)	+0.03 (Alnico 6, Cast and Sintered)
-0.02 (Alnico 5DG, Cast)	+0.03 (Alnico 5DG, Cast)
-0.02 (Alnico 5-7, Cast)	+0.03 (Alnico 5-7, Cast)
-0.025 (Alnico 8, Cast and Sintered)	+0.01 (Alnico 8, Cast and Sintered)
-0.025 (Alnico 8HC, Cast and Sintered)	+0.01 (Alnico 8HC, Cast and Sintered)
-0.025 (Alnico 9, Cast and Sintered)	+0.01 (Alnico 9, Cast and Sintered)

Example Alnico second quadrant demagnetisation BH curve

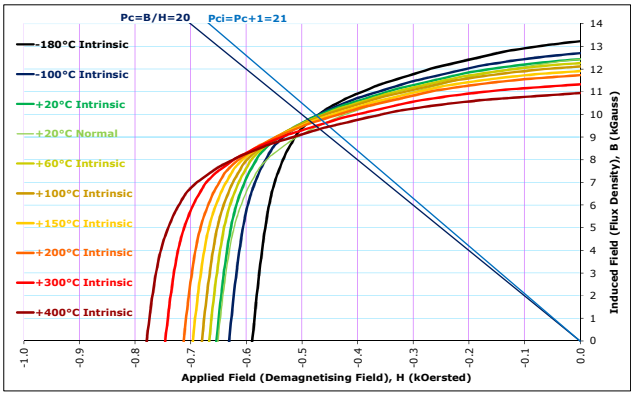

Additional Information

The magnet shape, its environment, and the actual application affect how the Alnico magnet will perform.
The Intrinsic curve (not the Normal curve, although similar in shape for Alnico) is needed to assist in determining magnet suitability.
For Alnico, it is important to keep the working point above the "knee" of the Intrinsic curve to avoid severe demagnetisation.
Rotating machines and generators using Alnico need careful design due to the varying air gap during rotor rotation.
We can assist in designing in resistance to demagnetisation. We can guide you with your design options.
A length to diameter (L/D) ratio of at least 4 or 5 is a rule of thumb guide when using Alnico. A high L/D ratio is important for resisting demagnetising.
External demagnetising factors such as other magnets and electromagnets must be taken into account. They will put a field onto the magnet risking demagnetising it.
Even pushing two Alnico magnets in repulsion into each other can weaken their output. However careful handling will quickly resolve this. Alnico can be remagnetised.
The risk of demagnetisation of Alnico is reduced by improving the working point (e.g. use a longer magnet, increase the L/D ratio, use a higher Hc, introduce magnetic steel to the circuit, etc).
Alnico magnets have the best temperature coefficients of any magnet type. Alnico has the least change in field output over a change in temperature. They can also operate at the highest temperatures of any magnet.
Cast Alnico can have a blackened surface - this is the "As Cast" finish with the surface texture coming from the sand cast mold. Machining of the Alnico (e.g. precision ground pole faces) leaves a bright silvery metallic finish.
Very small air holes may be seen from time to time within the structure of cast Alnico magnets. This is natural for cast magnets (due to the casting process) and cannot be avoided.
If you have any more questions, require technical assistance and would like a quotation, simply contact us.
Although we have made every attempt to provide accurate information, we do reserve the right to change any of the information in this document without notice.
We cannot accept any responsibility or liability for any errors or problems caused by using any of the information provided.

www.eclipsemagnetics.com
sales@eclipsemagnetics.com
Tel: +44 (0)114 225 0600
Fax: +44 (0)114 225 0610

bsi. ISO 9001 Quality Management
FM31278

HE144

Advanced Sensor Technology

Linear High Precision

Analog Hall Sensor HE144

Features

- Large magnetic field range - below milli-Tesla to over 10 Tesla
- Very small linearity error - typically 0,1 % up to 1,5 T
- Optimized for low Hall sensor current - typical 1000 Ohm and 0,2 Volt/Tesla at 1 mA
- Very high sensitivity
- Low noise
- Low drift
- Low inductive zero component, low EMC pickup
- Low temperature coefficients
- Very wide operating temperature range
- Very low PHE, Planar Hall Effect Error
- Very flat miniature package
- Pin compatible with Siemens®/Infineon® KSY14 and KSY44

Deviation from linearity at 1mA, 20 °C
Comparison with Infineon KSY44

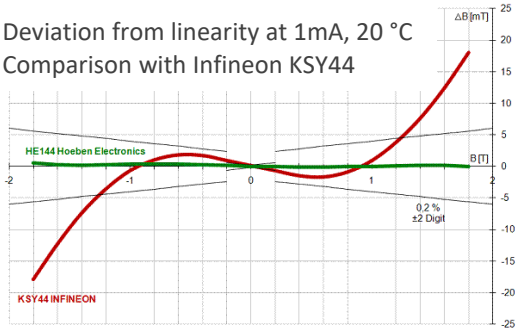

Our products are lead free devices, compliant with RoHS, REACH and 'Japan green' demands.

Typical applications

- Magnetic field measurements
- Oil drill measurement
- Position and rotation sensing
- Distance and thickness measurements
- Aerospace
- Current and power measurement
- Multi-sensor and differential usage
- Control of motor flux strength
- Windmills
- Movement sensing

Asensor Technology AB
Maskinvägen 6
746 30 Bålsta
Sweden

When Performance Matters

E-mail: hallsensor@asensor.eu
Phone: +46 8 590 755 10
Phone (NL): +31 6 515 900 81
www.asensor.eu

Specifications HE144

Electrical specifications		Values
Advised supply current		0,1 to 2,0 mA recommended 1 mA*
Open-circuit Hall voltage B=1 T		typical 200 mV at I=1 mA min 180 to max 360
Temperature coefficient of open-circuit Hall voltage B=1 T, at 25°C		typical -0,015 %/K at I=1 mA min -0,02 to max 0,02
Ohmic offset voltage B=0 T		≤± 12 mV at I=1 mA typical 10 mV **
Temperature coefficient of ohmic offset voltage B=0 T		typical 40 ppm/K (6,7 µT/K) at I=1 mA
Linearity of Hall voltage at I=1 mA	B = ± 0 to 1 T	≤± 0,2 % typical ≤± 0,1 %
	B = ± 1 to 2,4 T	Limit not specified typical ≤± 0,2 %
Supply side internal resistance B=0 T		900 to 1250 Ω typical 1000 Ω
Hall side internal resistance B=0 T		900 to 1700 Ω typical 1000 Ω
Thermal conductivity in air		≥ 1,5 mW/K
Thermal conductivity soldered		≥ 2,2 mW/K
Bandwidth		Not specified (contact us)

* Optimal signal to noise ratio and low power consumption

** Variations within the same production batch are very small.

Absolute maximum ratings		Values
Supply current		10 mA
Operating temperature	**P-version**	-40 to +170 °C
	SH-version	-40 to +125 °C
	T-version	-40 to +125 °C
	HT-version	-40 to +200 °C

For very low (cryogenic down to a few Kelvin) or very high (over 200 °C) temperature applications, contact us for more information.

Current Sensor Schematic

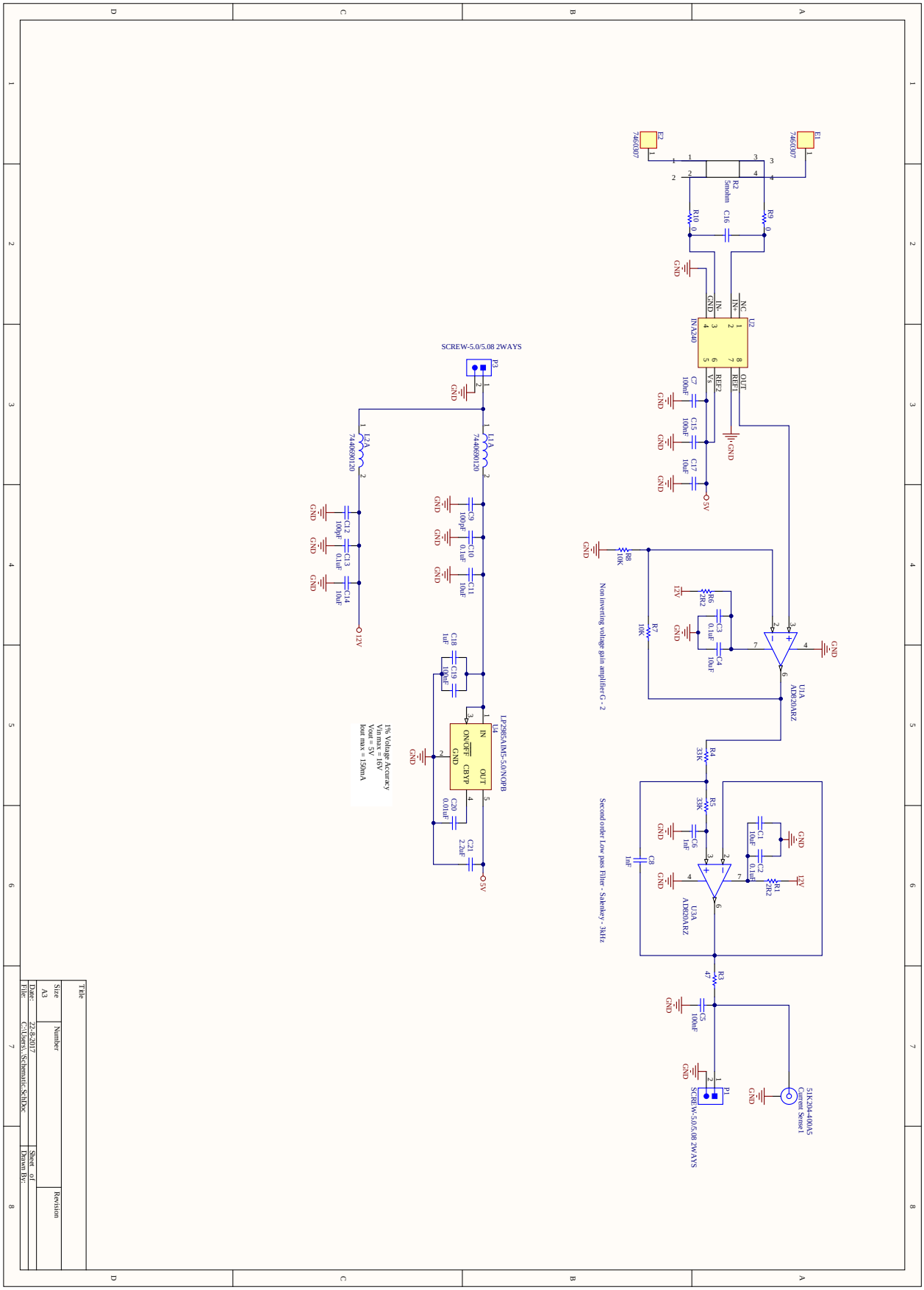

Signal Conditioning Schematic

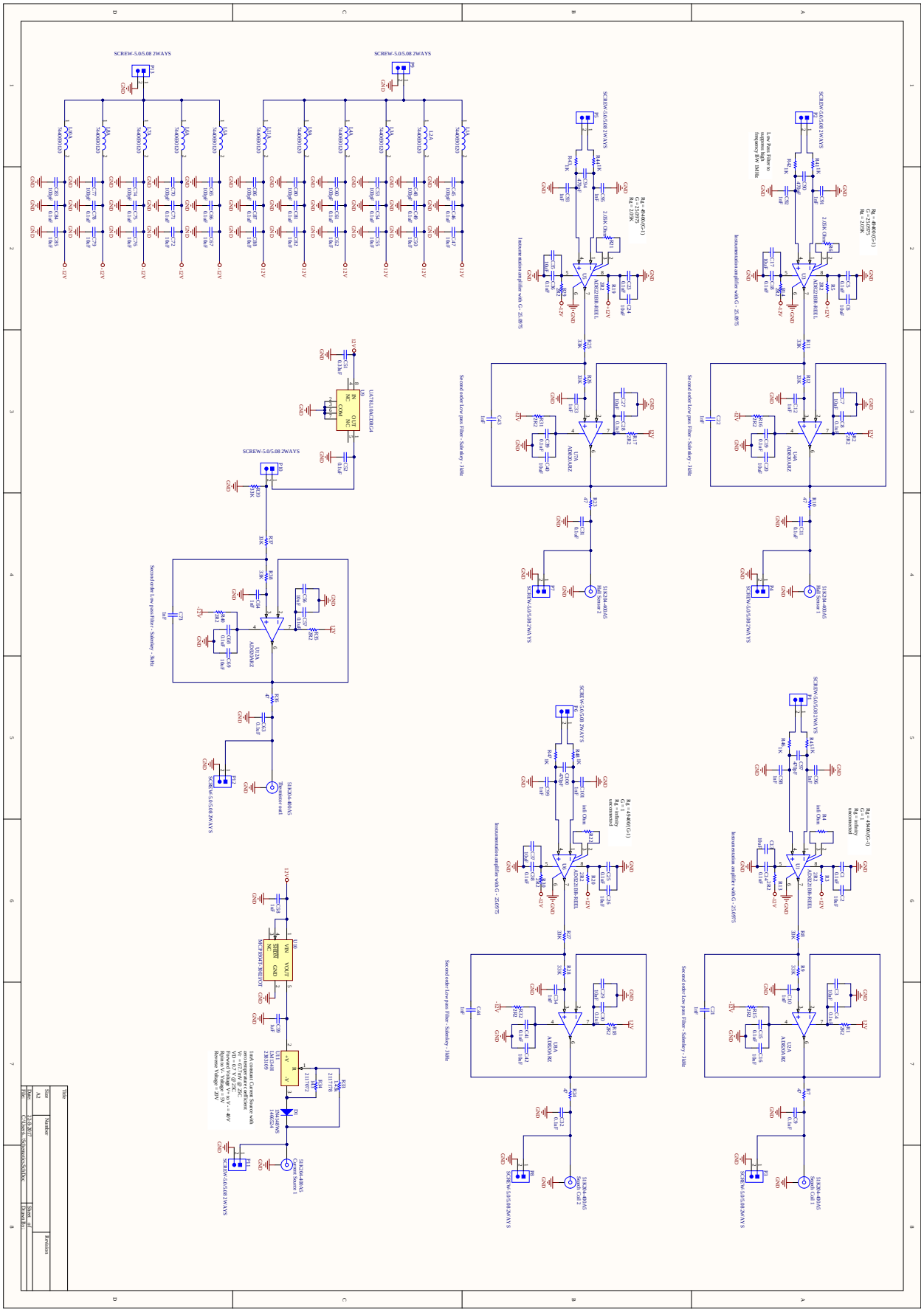

Linear Power Amplifier Schematic